Eur. Phys. J. H (2021)46:3
https://doi.org/10.1140/epjh/s13129-021-00002-z

THE EUROPEAN
PHYSICAL JOURNAL H

Regular Article

The history of LHCb

I. Belyaev[1], G. Carboni[2], N. Harnew[3], C. Matteuzzi[4,a], and F. Teubert[5]

[1] NRC Kurchatov Institute/ITEP, Moscow, Russia
[2] INFN and Università di Roma Tor Vergata, Rome, Italy
[3] University of Oxford, Oxford, UK
[4] INFN and Università Milano-Bicocca, Milan, Italy
[5] CERN, Geneva, Switzerland

Received 5 October 2020 / Accepted 3 December 2020

Abstract In this paper, we describe the history of the LHCb experiment over the last three decades, and its remarkable successes and achievements. LHCb was conceived primarily as a b-physics experiment, dedicated to CP violation studies and measurements of very rare b decays; however, the tremendous potential for c-physics was also clear. At first data taking, the versatility of the experiment as a general-purpose detector in the forward region also became evident, with measurements achievable such as electroweak physics, jets and new particle searches in open states. These were facilitated by the excellent capability of the detector to identify muons and to reconstruct decay vertices close to the primary pp interaction region. By the end of the LHC Run 2 in 2018, before the accelerator paused for its second long shut down, LHCb had measured the CKM quark mixing matrix elements and CP violation parameters to world-leading precision in the heavy-quark systems. The experiment had also measured many rare decays of b and c quark mesons and baryons to below their Standard Model expectations, some down to branching ratios of order 10^{-9}. In addition, world knowledge of b and c spectroscopy had improved significantly through discoveries of many new resonances already anticipated in the quark model, and also adding new exotic four and five quark states. The paper describes the evolution of the LHCb detector, from conception to its operation at the present time. The authors' subjective summary of the experiment's important contributions is then presented, demonstrating the wide domain of successful physics measurements that have been achieved over the years.

Contents

---

[a] e-mail: cxm@mail.cern.ch (corresponding author)

1 Introduction

LHCb is an experiment at the CERN LHC, dedicated to the study of heavy flavours with large statistics. The resulting high precision makes possible the observation of tiny deviations from the predictions of the Standard Model (SM) in *CP* violation and rare phenomena, variations which could hint at New Physics (NP) processes. LHCb started taking data in 2010. The so-called Run 1 commenced at an initial centre of mass energy of $\sqrt{s} = 7$ TeV which was then increased to $\sqrt{s} = 8$ TeV, collecting an integrated luminosity of 3.23 fb^{-1} until the end of 2012. After a two-year shutdown, LHC operation continued from 2015 to 2018 (Run 2), when the experiment took data at $\sqrt{s} = 13$ TeV, recording an integrated luminosity of ~ 6 fb^{-1}. Throughout the running periods, LHCb collected and analysed an unprecedented number of b decays, and also enlarged its scope to include charm physics, W and Z measurements, jets and nuclear collisions.

In this paper, the motivation for the LHCb experiment is described, recalling how its design was developed and evolved. The experiment's major achievements in terms of physics results are then summarised. Finally, we discuss the plans for the future upgrade, in the period when the Super-KEKB collider will also operate.

The layout of this paper is as follows. Introduction (Sect. 1) describes the status of the b physics programme at the time when the LHCb detector was conceived and provides an evolution of its design. In Sect. 2, the basic elements of the detector are described, optimised for the requirements of heavy-flavour physics measurements, together with a description of the triggers. The measurements which were originally the major aims of the experiment, i.e. the CKM matrix measurements and *CP* violation and very rare decays of the b-quark, are reviewed in Sects. 3 and 4, respectively. In Sect. 5, a summary of the wide-ranging results in b- and c-spectroscopy is presented. A review is given of the many *non-planned* physics areas in Sect. 6, such as results on jets, electro-weak (EW) physics and searches for new particles not associated with heavy flavours. In all these domains, LHCb proves to be an extremely versatile detector, providing complementary measurements to those of the LHC general purpose detectors (GPDs). The paper concludes in Sect. 8 with a short description of the upgrade plans, which will ensure LHCb operation beyond 2030.

The paper presents the authors' subjective summary of LHCb's many major physics results; however, the review inevitably omits a substantial number of important measurements. To this end, additional information can be found in the paper's exhaustive bibliography.

1.1 b physics at the end of the XXth century

In 1970 Glashow, Iliopoulos and Maiani postulated the existence of a fourth quark, *charm*, necessary to explain the smallness of K^0 oscillations in the framework of the Standard Model of Weak Interactions [1]. The so-called Glashow–Iliopoulos–Maiani (GIM) mechanism generalised Cabibbo's idea of rotated weak currents to the quark model with two doublets, introducing a 2×2 mixing matrix written in terms of the Cabibbo angle. An experimental confirmation of the fourth quark hypothesis came in 1974 with the discovery of J/ψ [2,3], soon identified as a $c\bar{c}$ bound state, and followed by the discovery of open charm. In 1973, Kobayashi and Maskawa [4] proposed a third heavy-quark doublet in order to describe *CP* violation in the framework of the SM, thus generalising the Cabibbo matrix to the 3×3 CKM (Cabibbo, Kobayashi, Maskawa) matrix. The discovery of the Υ in 1977, followed by the charged and neutral B-mesons in 1983 [5], proved the validity of their idea and held the prospect of understanding quantitatively *CP* violation.

The level of *CP* violation in b quark decays was expected to be orders of magnitude larger than in the neutral K system, but unfortunately the relevant decay channels had only tiny branching fractions, so the lack of intense "b-quark sources" slowed the progress of beauty physics: in particular, in 1986 the PDG only listed five decay modes of B^0 and $B^{\pm}$. However, in 1987 a new impetus came from the discovery at ARGUS of $B^0 - \overline{B}^0$ oscillations [6]. It was clear that the forthcoming LEP machine, designed for an entirely different purpose, and the symmetrical CESR collider, could not yield an exhaustive answer to all the questions related to the CKM hypothesis, despite their valuable contributions to many facets of b-physics [7,8]. When in 1989 P. Oddone proposed an asymmetric e^+e^- collider [9] operating at the $\Upsilon(4S)$ energy with a luminosity above 10^{33} $\text{cm}^{-2}\,\text{s}^{-1}$, an intense period of accelerator studies ensued. This gave birth to the PEP-II and KEKB B Factories, which were approved in 1994, and started operating in 1998, soon reaching and passing their design luminosity.

Around this time, proponents pursued the idea of exploiting hadron beams to attack the problem of detecting *CP* violation in the b sector. The idea behind this was that the large hadronic b production cross section plus the high-intensity hadron beams at the already existing and planned proton accelerators would produce a large number of $b\bar{b}$ pairs, sufficient to gather evidence for *CP* violation at least in the so-called golden channel $B^0 \to J/\psi K^0_S$. To achieve an adequate background rejection, the experimental difficulties were formidable because of the small ratio of the b cross sec-

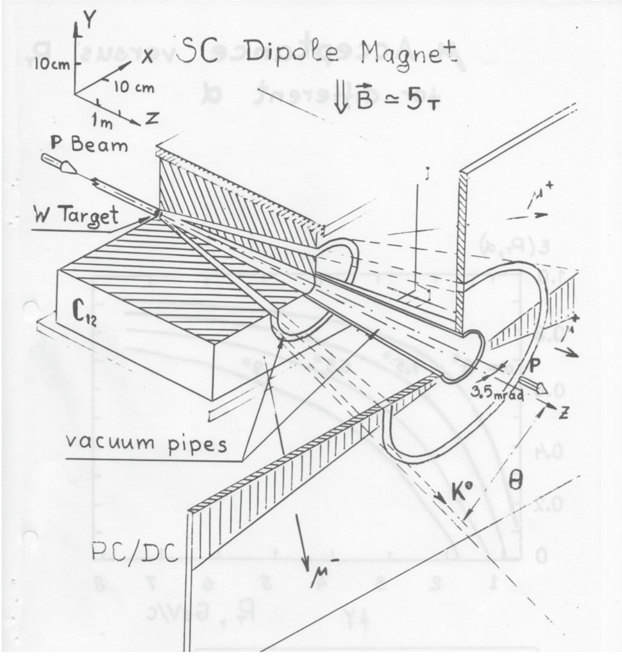

Fig. 1 A sketch of a proposed beam-dump style experiment designed to detect $B^0 \to J/\psi K^0_S$ decays. The K^0_S would traverse the conical slit before decaying [11]

tion to the total hadronic cross section at the $\sqrt{s}$ values available in fixed-target and collider experiments.

In 1985, the fixed-target WA75 hybrid experiment at the CERN SPS [10] observed in emulsions the first partially reconstructed $b\bar{b}$ pair produced by an extracted pion beam of 350 GeV/c, confirming that the production cross section at such low energies was very small. To circumvent this problem, simple experiments were proposed [11] for the CERN SPS and for the planned UNK machine [12] at Serpukhov, with a brute-force approach based on a high-intensity extracted beam and a minimalist detector designed to reconstruct the $B^0 \to J/\psi K^0_S$ decay and to provide flavour tagging (Fig. 1). There was no time-dependent analysis of the decay since the beam-dump character of the experiments made the use of a microvertex detector impossible. There were exploratory fixed-target experiments, at CERN (WA92) [13] and at Fermilab (E653, E672, E771, E789) [14], which tried to observe and measure beauty events, albeit without (or very limited) success.

In 1989, P. Schlein proposed a dedicated Beauty experiment exploiting the large b cross section expected at the CERN SPS proton-antiproton collider ($\sqrt{s} =$ 630 GeV) [15]. The authors of the proposal (P238) remarked that the bulk of $b\bar{b}$ production occurred at very small angles with respect to the beams, therefore making a compact experiment practical. The heart of the detector was a silicon microvertex detector operating very close to the beam (1.5 mm) coupled to a fast readout and track-reconstruction electronics. The microvertex detector provided the trigger by requiring that accepted events had to be inconsistent with a single vertex. P238 was not approved but the CERN R&D Committee, established to support new detector developments in view of the LHC, approved in 1991 a test of the microvertex detector [16] in the SPS collider. This proved very successful [17] and paved the way towards the future COBEX experimental proposal.

At the time when the e^+e^- colliders were approved, the HERA-B experiment had been conceived at DESY [18]. Approved in 1994, HERA-B exploited the 920 GeV HERA proton beam on a fixed target made of metallic wires, placed inside Roman Pots in the vacuum pipe, and immersed in the beam halo. HERA-B was approved to take data in 1998, one year before PEP-II and KEKB. The sophisticated apparatus consisted of a single-arm spectrometer, including a RICH, a large microvertex silicon detector, a high-resolution tracker, plus an electromagnetic calorimeter. HERA-B was designed primarily for the detection of the $B^0 \to J/\psi K^0_S$ decay and its trigger was based on J/ψ reconstruction at the first level.

At $\sqrt{s} = 40$ GeV, the $b\bar{b}$ cross section is about 10^{-6} of the total hadronic cross section, hence HERA-B had to achieve a background rejection around 10^{-11} for the $B^0 \to J/\psi K^0_S$ decay. Data taking conditions were similar to those of the current LHCb experiment (a 40 MHz interaction rate), as were the requirements of radiation resistance. HERA-B started data taking in 2000, but it soon emerged that the detector did not have sufficient rejection power against background and the track reconstruction was not as efficient as expected.

The large number of detector stations and their total thickness in terms of radiation lengths made secondary interactions an important issue for event reconstruction. Eventually, HERA-B could not observe b events efficiently, but taught several valuable lessons for any future experiment working in a crowded hadron-collision environment. These were a need of a robust and efficient tracking and a flexible trigger systems able to adapt to harsher environments than may have been expected, as well as the need to design the thinnest and lightest detector (in terms of radiation and interaction lengths).

1.2 Towards the LHC

Over the same period, the planned LHC and SSC machines, with their large energies, promised spectacular increases of the $b\bar{b}$ cross section, thus making the task of background rejection much simpler. This was particularly true for operation in collider mode, but even in fixed-target mode ($\sqrt{s} \approx \mathcal{O}(130)$ GeV) the b cross section was expected to be a respectable 1 μb at the LHC and 2 μb at the SSC [19]. The large cross section and corresponding good background rejection would facilitate a hadron B Factory, competitive and complementary with e^+e^- colliders, which could focus primarily on the measurement of CP violation and also allow the study of the spectrum of all b particles. Given the intrinsically "democratic" nature of hadronic production, the new hadron machines would also give access to large samples of B_s^0 and of b baryons, something not possible at e^+e^- colliders operating at the Υ resonances.

Two schools of thought soon emerged: one pursuing a fixed-target (FT) strategy and the other based on a collider mode. The more favourable ratio of the $b\bar{b}$ to the total hadronic cross section, about two orders of magnitude larger in collider mode, gave this a competitive advantage.

There was, however, a strong reason in favour of the FT concept: a collider B experiment could not operate at the design luminosity of the machine ($10^{33-34}\,\mathrm{cm}^2\mathrm{s}^{-1}$) because of the significant number of overlapping interactions (pile-up) with multiple vertices. This would have required dedicated low-luminosity running, creating a potential conflict with the major experiments and considerably reducing the data-taking time. Later it was ascertained that the individual experiment luminosities could be tuned over a broad range with an appropriate design of beam optics in the interaction regions; hence, this would become a moot point, but at the time it was a serious one.

Moreover, for the advocates of the FT approach, the advantage of the larger cross section in collider mode was partially offset by the higher event multiplicity and by the shorter flight path of beauty particles. In addition, while the p_T of the b decay products would to a good approximation be the same in the two modes, the p_T of the other collision products would be smaller in FT mode, thus making the trigger simpler. Active silicon targets were also possible with an extracted beam, where the track of a charged b-hadron would be directly measured.

Finally, $b\bar{b}$ production kinematics is forward peaked in the centre-of-mass (CM) system, but the Lorentz boost of the centre-of-mass in the FT mode ($\beta\gamma > 60$) concentrates the event at smaller angles than in collider mode. It was therefore possible, in principle, to build a more compact detector, achieving larger angular acceptance at lower cost. There was also the possibility of recycling components (in particular dipole magnets) from existing detectors. The cost was an important consideration, since a dedicated B experiment at the LHC (or SSC) was generally considered to have secondary importance with respect to the general-purpose experiments.

The anticipated demise of the SSC led three groups to study and propose dedicated b experiments at the LHC. The three Letters of Intent (LoI) were presented in 1993. COBEX [20], an acronym for Collider Beauty Experiment, with P. Schlein as spokesperson, was a collider experiment with a backward–forward geometry. The other two proposals, Gajet [21] (spokesperson T. Nakada) and LHB [22] (spokesperson G. Carboni), were fixed target experiments, the first, as the name suggests, using a gas jet target, the latter exploiting an extracted beam. Since no traditional beam extraction was foreseen for the LHC, LHB (large hadron beauty-factory) used a parasitic extraction technique, based on channeling in a bent silicon crystal placed close to one of the circulating beams (Fig. 2).

A dedicated R&D experiment, RD22, approved by the CERN DRDC [23] to test the feasibility of this idea at the SPS, demonstrated that high-efficiency beam

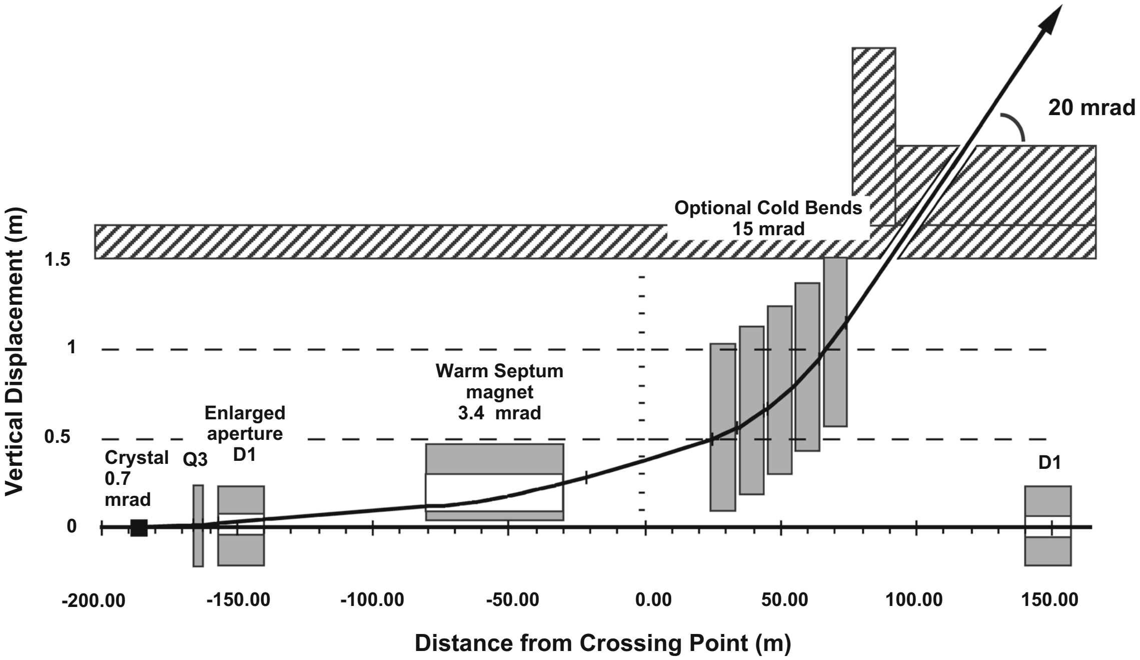

Fig. 2 Proposed LHC beam extraction scheme based on crystal channeling. The channeled beam, deflected by 0.7 mrad in a bent silicon crystal, was guided towards the beam transport tunnel by several conventional magnets. The cost of the extracted beam was a non-negligible fraction of the detector cost

extraction (larger than 10%) was possible [24]. The three proposed experiments were presented in their final form in 1994 at the Beauty'94 Conference [25]. It should also be noted that, by then, CDF had already contributed important b-physics results [25], offering a glimpse of what would later prove to be the extraordinary success of b-physics at hadronic machines.

Following the submission of the LoIs, the LHC Committee (LHCC) considered the proposals in June 1994. One of its concerns was the small size of the three collaborations: the total number of physicists involved was barely one hundred. In addition, the Committee remarked that beam extraction by channeling could not be guaranteed at that stage, because accelerator experts feared possible interference with normal LHC operation. Finally, the following recommendation was issued: *"The collider model approach has the greater potential in view of the very high rate of b production, the much better signal/background ratio and the possibility of exploring other physics in the forward direction at 14 TeV"*.

The LHCC encouraged the three collaborations to join together and design a new experiment, incorporating attributes of each, and operating in collider mode. The LHCC noted that its ambitious request was justified by the fact that, at the startup of the LHC, the experiment would not be an exploratory one, since CP violation would already have been observed "at HERA-B, FNAL or B Factories". The LHCC also issued guidelines requiring a number of issues to be addressed and solved. The three experiments combined into the new LHC-B Collaboration (then named), which published its Letter of Intent in 1995 [26].

The new experiment derived several of its characteristics from the parent proposals: notably the concept of a silicon vertex detector in retractable pots, the calorimeter design and the high p_{T} first-level trigger.

In the transition to LHC-B, a number of proponents from the former three collaborations decided not to continue. This unfortunately included P. Schlein and his UCLA colleagues who had pushed very strongly for the collider-mode idea with COBEX, and who had been a driving force up to that point. The LHCC decision sent a strong signal to the high-energy physics community: that CERN were prepared to give their strong support to one dedicated B experiment. This encouraged many physicists from institutions around the world to join the new collaboration over the subsequent years. T. Nakada, who was an instigator of the Gajet proposal, was elected LHC-B spokesperson. The 1995 Letter of Intent of LHC-B established the basis for the new detector design, which was refined in the following years, until its approval in 1998. By that time, the name had changed from LHC-B to simply LHCb. Figure 3 shows the detector as it appeared in the Letter of Intent.

Soon afterwards, a competing B-physics experiment, BTeV [27], was proposed to run at the Fermilab Tevatron, incorporating a single magnet, a double arm spectrometer and a vertex trigger at the first level, in order to recover the reduced b production cross section. Following the decision to shut down the Tevatron, BTeV was not approved; however, several of the experiment's innovative ideas were carried through to the future LHCb experiment.

2 The LHCb detector

The basic mechanism for heavy-quark production at the LHC is via gluon–gluon fusion. The angular distribution of $c\bar{c}$ or $b\bar{b}$ pairs is peaked at small angles with respect to the beam line, with high correlation between the constituents of the pair. This allows the detection with good acceptance of the resulting hadrons in a rather limited solid angle. QCD calculations give cross-section values of $\sigma_{c\bar{c}} \simeq 1.5$ mb and $\sigma_{b\bar{b}} \simeq 0.5$ mb, respectively. The large event multiplicity requires a high granularity of the detector, together with minimal thickness in terms of radiation and interaction lengths to reduce secondary interactions.

The LHC-B LoI [26] presented a forward spectrometer with 400 mrad acceptance and a single large dipole magnet. The apparatus would be located inside the former DELPHI cavern at LEP with little modifications to the existing infrastructure but, for reasons of cost, the detector sacrificed half of the solid angle by only being a *single* arm spectrometer. The LoI design inherited important features from the three ancestor experiments and from the contemporary HERA-B, which had rate and radiation issues similar to those expected at the LHC. In contrast to the latter experiment, LHC-B had in addition a hadron calorimeter and a second (upstream) RICH with two radiators. Initially it was thought that an efficient tracking system in a harsh environment would require a large number of tracking stations, so, paralleling HERA-B, LHC-B had twelve tracking stations in the large-angle region. This number was reduced to ten in the Technical Proposal presented in 1998 [28], which by then had changed its name to LHCb.

The disappointing performance of HERA-B was largely ascribed to the large amount of material in the detector, which prompted the LHCb collaboration to perform a thorough review of the apparatus, with the aim to reduce material without sacrificing performance. A Technical Design Report submitted in 2003 presented the LHCb "Reoptimized" Detector [29]. This is the basis on which the experiment was eventually built and is described in the following subsections.

2.1 Overview

The LHCb detector [30] is a forward spectrometer, as shown in Fig. 4, and is installed at Intersection Point 8 of the LHC. A modification to the LHC optics, shifting the interaction point by about 11 m from the centre, allowed maximum use of the cavern space. This results in a detector length of approximately 20 m, and with maximum transverse dimensions about 6×5 m^3. The angular acceptance ranges from approximately 10 mrad to 300 mrad (Fig. 5) in the horizontal magnetic-bending plane, and from 10 mrad to 250 mrad in the vertical plane (Fig. 4). With this geometry, the detector is able to reconstruct approximately 20% of all $b\bar{b}$ pairs produced.

To measure the momenta of charged particles, a dipole magnet producing a vertical magnetic field is used. It is a warm magnet providing an integrated field of 4 Tm, with saddle-shaped coils in a window-frame yoke, and with sloping poles in order to match the required detector acceptance. The design of the magnet allows for a level of fringe field inside the upstream Ring Imaging Cherenkov detector (RICH 1, see Sec. 2.4) of less than 2 mT while providing a residual field in the regions between the upstream tracking stations.

The tracking system consists of a silicon VErtex LOcator detector (VELO) [31], surrounding the interaction region, and four planar tracking stations, the TT tracker upstream of the dipole magnet and three tracking stations T1-T3 downstream of the magnet [32,33]. The T1-T3 stations consist of an inner tracker (IT), located at the centre of the stations and surrounding the beam pipe, and an outer tracker (OT) for the outer regions. A minimum momentum of around 1.5 GeV/c is required for a track to reach the downstream stations [34].

Particle identification (PID) is a fundamental to the goals of the LHCb experiment by separating pions, kaons and protons produced in heavy-flavour decays. Accurate reconstruction of electrons and muons is cru-

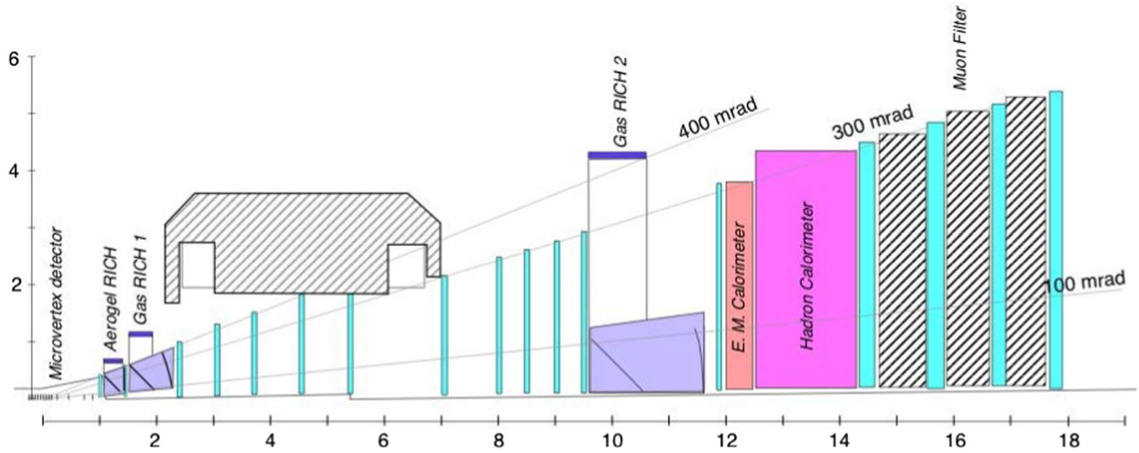

Fig. 3 The LHC-B detector as it was proposed in 1995. All the basic components shown would be part of the final detector, albeit with many refinements and optimisations that will be described in the following section

Fig. 4 The LHCb detector: side view

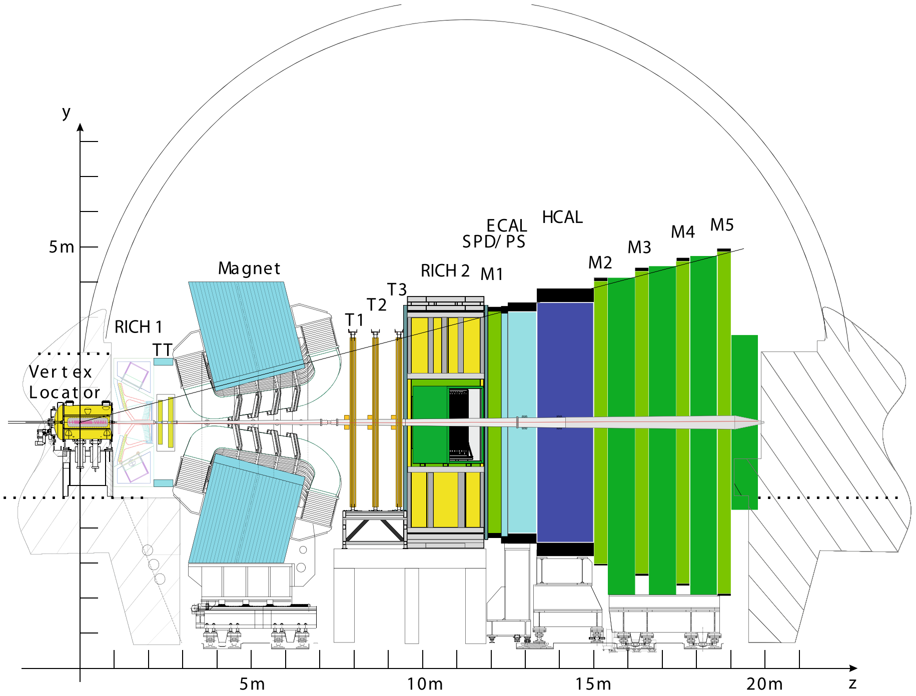

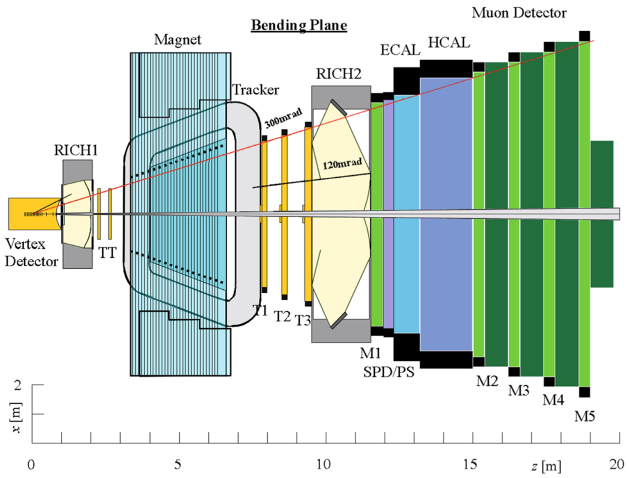

Fig. 5 The LHCb detector: top view

cial for flavour tagging. All aspects of PID are accomplished by a set of specialised detectors.

The PID system is based around two RICH detectors, designed to cover almost the full momentum range of tracks in LHCb. The upstream detector, RICH 1, covers the low momentum region from $\simeq 2$ to 60 GeV/c using aerogel (in Run 1 only) and C_4F_{10} radiators, while the downstream detector, RICH 2, covers the high momentum range from 15 GeV/c up to and beyond 100 GeV/c using a CF_4 radiator.

Two calorimeters, one electromagnetic (ECAL) and the other hadronic (HCAL), supplemented by a preshower detector (SPD/PS) [35], provide identification of electrons, photons and hadrons and a measurement of their energy. This measurement is used at the trigger level to select candidates on the basis of their transverse energy. Muons play a crucial role in many of LHCb's measurements because of the cleanliness of the signature. Their identification is achieved by five muon stations (M1–M5), interspersed with iron filters. The muon system also supplies measurements of muon transverse momenta for the trigger.

2.2 The vertex locator

The role of the VELO is to measure the impact parameters of all tracks relative to the primary vertex (PV), to reconstruct the production points and decay vertices of hadrons containing b- and c-quarks and to allow precision measurements of their mean lifetimes. The subdetector accepts particles with pseudorapidities in the range $1.6 < \eta < 4.9$ and which have PVs within $|z| < 10.6$ cm from the nominal collision point along the beam direction. The VELO is split into two halves surrounding the beam pipe, each containing 21 modules. Each module is then made up of two silicon half discs of 300 µm thickness, one with strips in the radial, r coordinate, the other in the polar, ϕ coordinate. This cylindrical geometry allows a fast track- and vertex-reconstruction to be made at the second stage of trigger. The strip segmentation is such to limit the highest occupancy of the strips to less than 1.1 %.

The VELO is positioned, with an accuracy better than 4 µm, at the closest distance possible from the beam, about 7 mm during data taking. The sensors operate within a so-called *Roman pot* configuration, located inside a secondary vacuum of less than $2{\cdot}10^{-7}$ mbar pressure, separated from the primary LHC vacuum. The sensors are retracted during beam injection and are then quickly moved in for physics operation when the LHC beams are stable.

The vessel containing the silicon discs and the front-end electronics (RF-box) has aluminium walls of 300 µm thickness to minimise multiple scattering. The average material budget of the detector for tracks in the LHCb acceptance is 0.22 X_0. In order to minimise radiation damage and to dissipate the produced heat, a cooling system keeps the temperature range between -10 and 0°C.

Figure 6 summarises the VELO performance in terms of impact parameter and decay time resolution [31].

2.3 The TT and downstream tracking system

Following the VELO, the tracking system is composed of the TT station, located between RICH 1 and the magnet, and three stations (T1,T2,T3) downstream of the magnet. The TT is composed of four stations grouped in pairs, called TTa and TTb, spaced by 30 cm. Each station consists of silicon microstrip planar modules covering a rectangular area of 150 cm × 130 cm (width times height), covering the LHCb acceptance of 300 mrad in the horizontal plane and 250 mrad in the vertical. The strips of the first and the fourth stations are vertical and measure the bending x coordinate, while the second and third planes have stereo angles of $\pm 5°$, respectively.

Tracking stations T1 - T3 each consist of an inner part (IT) surrounding the beam pipe, and an outer part (OT) beyond. Each IT station consists of four overlapping silicon layers, two rotated by a stereo angle of $\pm 5°$ and two aligned to the y (vertical) axis. Each layer is made up of four independent modules placed around the beam pipe, covering about a 120×40 cm^2 area, as shown in Fig. 7.

The spatial resolutions of both the TT and IT are approximately 50 µm per hit, with strip pitches of about 200 µm. The hit occupancies vary between 1.9% for the inner sectors to 0.2% for the outermost modules. To minimise radiation damage, the sensors operate at 5°C temperature.

The OT is a drift detector [32] consisting of straw tubes with internal diameters of 4.9 mm, each filled with an Ar/CO_2 gas mixture in a ratio 70−30%. The straws provide a 35 ns maximum drift time and 205 µm spatial resolution with 17% maximum straw occupancy. Each of the three stations is made of four modules, as shown schematically in Fig. 8. A picture of the assembled OD is shown in Fig. 9. In the first and third modules, the straw tubes are aligned to the vertical axis

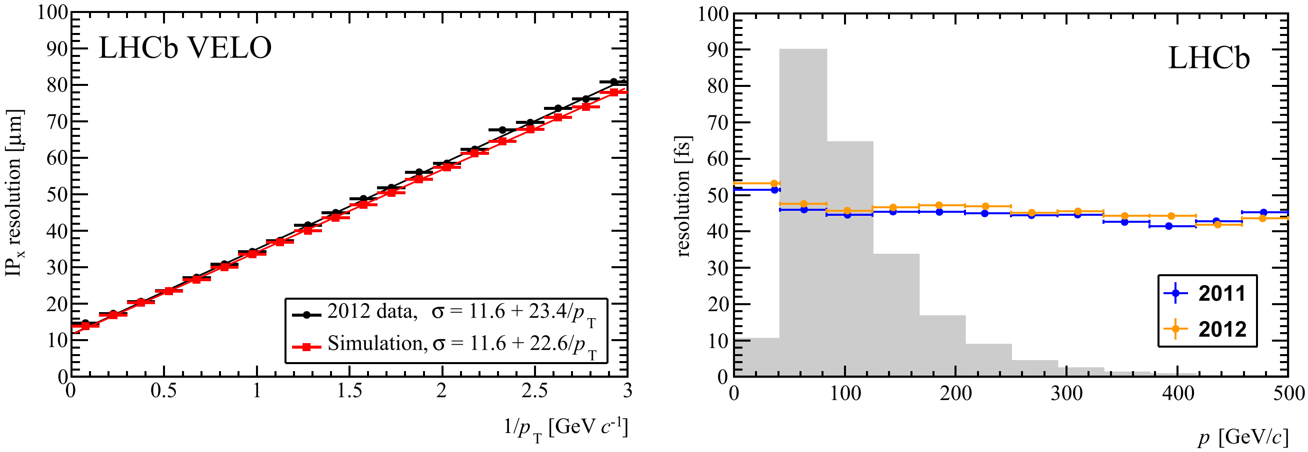

Fig. 6 Left: Projected impact parameter resolution as a function of $1/p_T$. Right: Decay time resolution (points) as a function of momentum for $B_s^0 \to J/\psi\phi$ decays. The superimposed histogram shows the distribution of momentum for the decay

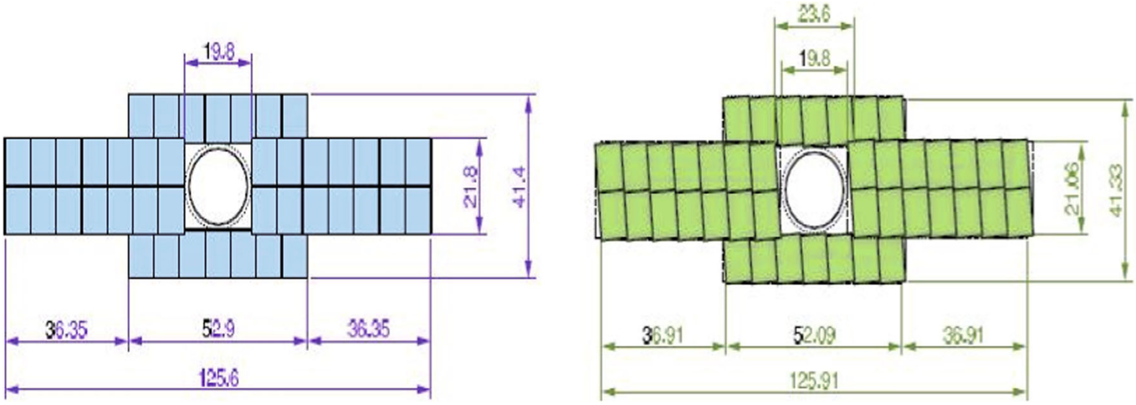

Fig. 7 The LHCb inner detector, (left) a vertically-aligned layer, (right) a stereo layer

while the third and fourth modules have stereo angles of ±5°. The total active area is about 5.97×4.85 m^2, covering the full LHCb acceptance.

The overall tracking efficiency for "long" tracks (i.e. those tracks measured in all the tracking detectors including the VELO) is greater than 96 % for $5 < p < 200$ GeV/c. The momentum resolution dp/p is 0.5% at low momentum, increasing to 1.1% at 240 GeV/c. The mass resolution is 14.3 MeV/c^2 for the J/ψ resonance.

2.4 The RICH system

The role of the RICH system [36] is to provide $\pi/K/p$ discrimination for LHCb, which is essential for most *CP*-violation studies, background rejection and flavour tagging. The momentum range which contains 90% of kaons, pions and protons from B meson decay is between 2 and 150 GeV/c and, to achieve this separation, two Cherenkov detectors, RICH 1 and RICH 2, are employed.

The RICH 1 detector differentiates particles with low and intermediate momenta, from 1 to ∼60 GeV/c. It is located close to the interaction region, upstream of the magnet, and covers the acceptance from ±25 mrad to ±300 mrad (horizontal plane) and to ±250 mrad (vertical plane). RICH 1 initially contained two different radiator materials: an aerogel layer 5 cm thick with refractive index $n = 1.03$ and a C_4F_{10} gas layer of length 85 cm with refractive index $n = 1.0014$. Aerogel has the power to provide π/K discrimination from about 1 up to 10 GeV/c; however, it was removed for Run 2 due to occupancy problems. The C_4F_{10} radiator extends the positive π/K identification from about 10 GeV/c to 60 GeV/c; however, π/K discrimination below 10 GeV/c is still possible by operating the RICH in kaon veto mode.

RICH 2 has a smaller angular acceptance of ±15 mrad to ±120 mrad (horizontal plane) and to ±100 mrad (vertical plane) and covers the region where high momentum particles are most abundant. It is located downstream of the magnet, between T3 and the first muon station M1. RICH 2 uses a CF_4 gas radiator with refractive index $n = 1.00046$.

In both detectors, Cherenkov photons are detected by a combined system of plane and spherical mirrors to focus photons onto a pair of photo-detector planes, where hybrid photon detectors are employed to detect the Cherenkov rings. The photo-detectors are located outside the detector acceptance, in regions of low magnetic field and relatively low radiation.

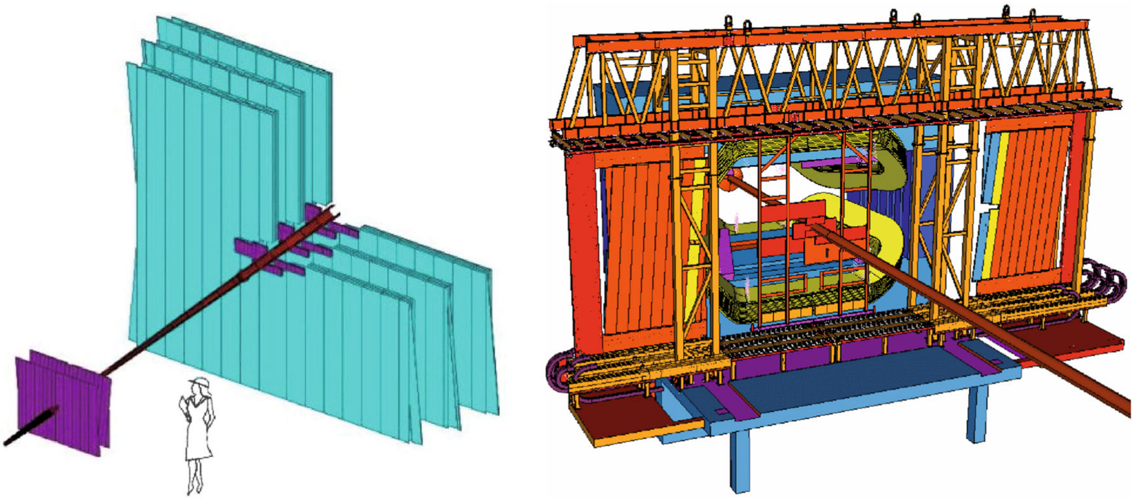

Fig. 8 Schematic views of the LHCb outer detector

Fig. 9 The LHCb outer detector in place on the beam line. Well visible is the beam pipe

The Cherenkov angles for the three different RICH radiators and for different particles as a function of momentum are shown in Fig. 10 (left). A measurement of RICH performance in LHCb data is shown for the two gaseous radiators in Fig. 10 (right) [36].

2.5 Calorimeters

The calorimeter system identifies hadrons, electrons and photons, and also measures their energies and positions for the Level-0 trigger. The system is composed of four sub-detectors: the scintillator pad detector (SPD), the preshower detector (PS), the electromagnetic calorimeter (ECAL) and the hadron calorimeter (HCAL). The SPD and PS are located just upstream of the ECAL. The ECAL, PS and SPD are segmented into three sections in the xy plane, with active pads growing from the inner to the outer regions. The HCAL is similarly divided into two sections. The corresponding granularities are outlined in Fig. 11.

The SPD and PS are used at the trigger level and offline, in association with the ECAL, to indicate the presence of electrons, photons and neutral pions. The detectors have two plastic scintillator layers separated by a 15-mm-thick lead plate where electrons and photons can radiate; the downstream scintillator then samples the radiated energy.

The light from the scintillators is sent to photomultipliers by wavelength-shifter (WLS) optical fibres.

The ECAL employs the *Shashlik* technology, where independent modules, constructed from scintillating tiles and lead plates, are alternated (see Fig. 12). The ECAL has 66 layers of such modules consisting of 2 mm of lead followed by 4 mm of scintillator mate-

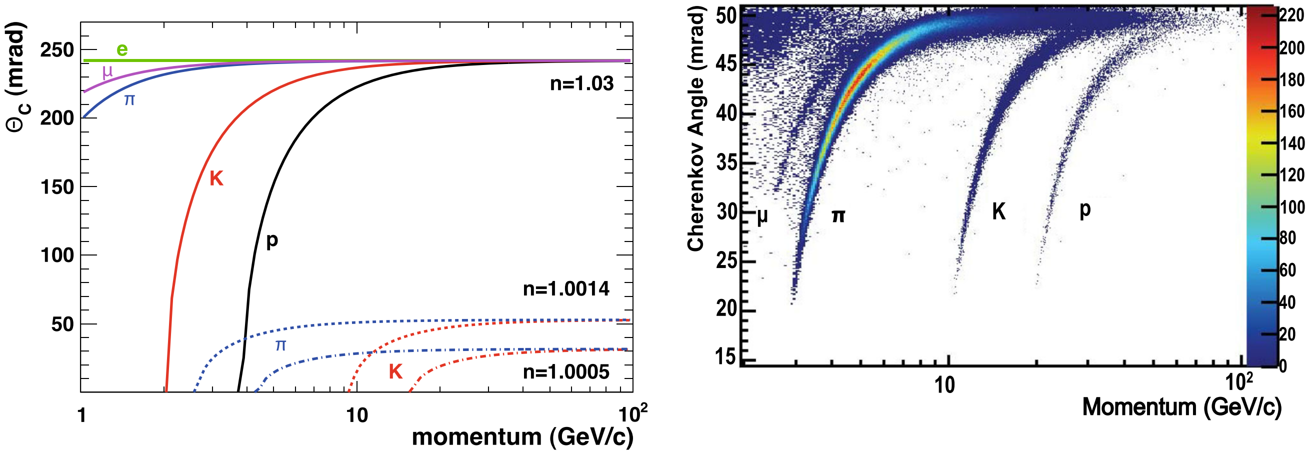

Fig. 10 (Left) Values of Cherenkov angle as a function of momentum for different particles for the three RICH radiators of refractive index n. (Right) Measured Cherenkov angles in LHCb data [36]

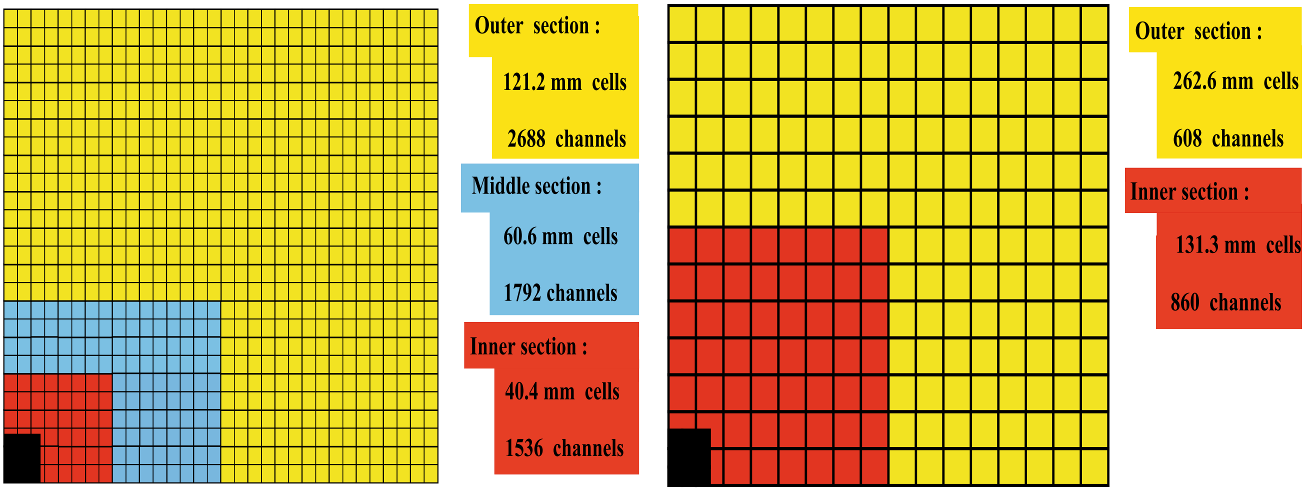

Fig. 11 The (left) LHCb electromagnetic calorimeter and (right) hadronic calorimeter. The bottom left regions indicate the areas occupied by the beam pipe

rial. The ECAL also uses WLS optical fibres to guide the light from the detector to photomultipliers, placed on the back face of each module. The energy resolution achieved [35] is

$$\frac{\sigma(E)}{E} = \frac{10\%}{\sqrt{E}} \oplus 1\% \tag{2.1}$$

where E is the electron energy expressed in GeV.

The HCAL is also a sampling calorimeter. It is constituted of iron absorber with scintillating tiles as the active material. The innovative feature of this sampling structure is the orientation of the scintillating material: the tiles run parallel to the beam axis. In the lateral direction, tiles are spaced with 1 cm iron, while longitudinally the length of the tiles and iron spacers correspond to the hadron interaction length $\lambda_I \simeq 20$ cm in steel. Light is collected by WLS optical fibres running along the detector towards the back side where the photomultiplier tubes are located (see Fig. 12).

The HCAL is used to measure the hadronic shower transverse energy for the Level-0 trigger and to improve the high-momentum electron/hadron separation. The energy resolution achieved is

$$\frac{\sigma(E)}{E} = \frac{(69 \pm 5)\%}{\sqrt{E}} \oplus (9 \pm 2)\% \tag{2.2}$$

where E is the hadron energy in GeV.

2.6 The Muon system

The Muon system consists of five stations, M1-M5, of rectangular shape. The complete system is made up by 1368 multi-wire proportional chambers supplemented by 12 triple GEM chambers in the inner region of the first station, to cope with the very high particle rate. The chambers employ a variety of readouts, optimised for a precise p_T measurement for the trigger. The complete system has an acceptance in the bending plane from 20 mrad to 306 mrad, and in the non-bending plane from 16 mrad to 258 mrad. This results in a total acceptance of about 20% for muons from semileptonic inclusive b decays.

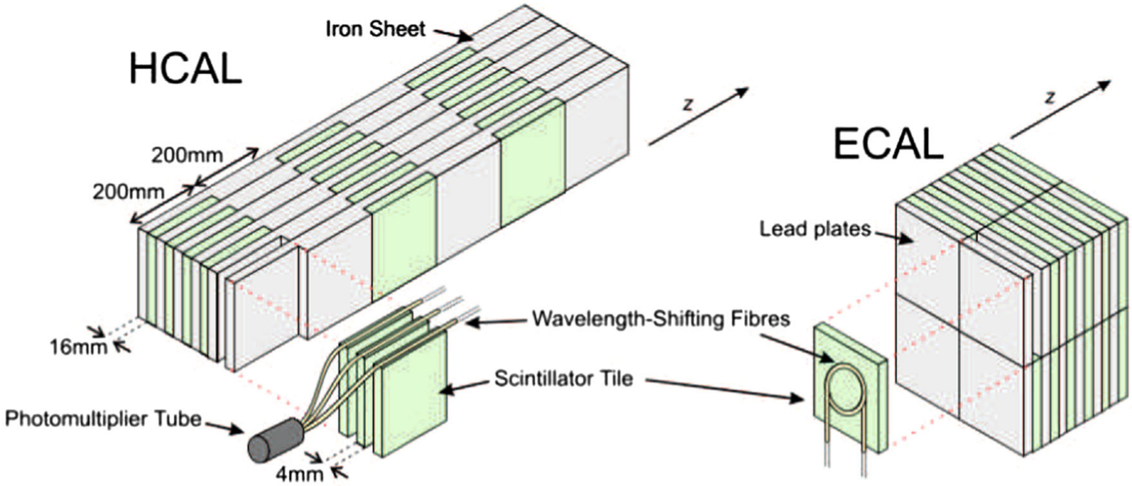

Fig. 12 A schematic showing the layout and segmentation of the LHCb ECAL and HCAL calorimeters

The M1 station is located in front of the calorimeters and is used in order to improve the p_t measurement for the trigger. The geometry of the five stations is projective; all the transverse dimensions scale as the distance from the interaction point. Stations M2-M5 are placed downstream of the calorimeters and are interleaved with 80-cm-thick iron absorbers. The total absorption thickness, calorimeters included, is about 20 interaction lengths. In this way, the minimum momentum for muons crossing the five stations is about 6 GeV/c.

Each muon station is designed to achieve an efficiency above 99% in a 20 ns time window with a noise rate below 1 kHz per physical channel, as described in [37]. To reach such an efficiency, four chamber layers per station are used in M2–M5 (two layers in M1). The time resolution is achieved by a fast gas mixture $\mathrm{Ar/CO_2/CF_4}$ in the ratio 40:55:5. A ratio 45:15:40 is employed in the Triple GEM chambers.

2.7 The trigger

Even with the relatively large $b\bar{b}$ cross section at LHC energies, only approximately 1% of visible pp interactions result in a $b\bar{b}$ event. Moreover, only about 15% of those events will produce at least one b-hadron with all decay products passing within the acceptance of the spectrometer. The branching fractions of decays used to study CP violation are typically less than 10^{-3}. Further reductions are unavoidable in the offline selection, where stringent cuts must be applied to enhance signal over background. Therefore, the purpose of the LHCb trigger is to achieve the highest efficiency for the events later selected in the offline analysis while rejecting drastically most of the uninteresting background events. To achieve this goal, the trigger uses information from all LHCb sub-detectors.

The trigger is organised in two different levels: the Level-0 (L0) trigger based on custom electronic boards, and the high-level trigger (HLT), implemented in a computer farm. Level-0 uses the information from the calorimeter and muon systems, performing a selection in order to reduce the event rate from 40 MHz to below 1 MHz, which is the maximum frequency allowed to read out the entire detector. The HLT is a software application running on a processor farm that further reduces the rate of events in the kHz range for storage (see Fig. 13).

The HLT has significantly evolved over time from the original design in the LHCb technical proposal (TP) [38] in 1998, to the trigger design in the technical design report (TDR) [39] in 2003, to the Run 1 (2010-2012) actual implementation [40] and finally to the additional features introduced during Run 2 (2015-2018) [41]. In the TP, it was assumed that a first HLT trigger level (L1) would reduce the 1 MHz input rate to a 40 kHz output rate with a variable latency of less than 256 μs, using coarse information from the vertex detector to reconstruct vertices and tracks with no momentum information (the VELO r-ϕ geometry was designed for this purpose). A second HLT trigger level (L2) was fashioned to extrapolate VELO tracks into the magnetic field to the tracking stations downstream of the magnet and reduce the output rate to 5 kHz with an average latency of 10 ms. Finally, a third level (L3) would implement the full-event reconstruction and a set of exclusive selections to bring down the rate to 200 Hz.

By the time of the trigger TDR in 2003, it became clear that the LHC was not going to start before the end of the decade when much more powerful processing units would become available. In addition, a series of test-beam and detailed simulation studies convinced the collaboration of the need to have momentum information at the first stage of the HLT. Therefore, a new tracking station just upstream of the magnet was introduced (the TT station). In addition, a shield which had been protecting RICH1 from stray magnetic fields was removed to allow for a rough estimation for the momentum of tracks reconstructed between the VELO and TT stations. The software trigger then had two levels: Level-1 able to reduce the output rate to 40 kHz using L0, VELO and TT information with an average latency of 1 ms, and HLT to reduce the output rate to 200 Hz with a combination of inclusive and exclusive selections. Between the time of the trigger TDR and the first physics run (Run 1), the interest in having a more performing HLT for charm physics ($c\bar{c}$ with a factor 20 larger production cross section than $b\bar{b}$) and a much more robust system convinced the collaboration to push for much more inclusive selections in the final trigger stage and a much larger trigger output rate (3–5 kHz). This implied a complete redefinition of the offline data processing model.

Furthermore, it had been assumed that the LHC would operate with a 25 ns bunch separation, limiting the number of overlapping events to a mean number of $\mu \simeq 0.4$ per bunch crossing at a luminosity of 2×10^{32} cm^{-2}s^{-1}. When, from 2011, a separation of 50 ns was adopted for early LHC operation, the experiment decided to run at $\mu \approx 1.4$ to compensate for the lower number of bunches. Therefore, the HLT had to adapt to running conditions rather different than first assumed. This was made possible by the highly flexible design of the HLT.

After the success of the LHCb trigger performance in Run 1, the good understanding of the trigger reconstruction allowed the introduction of the "real-time analysis" concept during Run 2. After the first HLT trigger level (HLT1), events are buffered to disc storage in the online system. This is done for two purposes, firstly events can be processed further during inter-fill periods, and secondly the detector can be calibrated and aligned run-by-run before the HLT2 stage. Once the detector is calibrated and aligned, events are passed to HLT2, where a full event reconstruction of "offline quality" is performed. This allows for a wide range of inclusive and exclusive final states to trigger and obviates the need for further offline processing. In addition, new techniques to reduce the amount of information saved per event [42] allowed to increase significantly the output rate to 10-15 kHz, as in Fig. 13, while the output of HLT1 could be increased to $\mathcal{O}(110$ kHz$)$. The decrease in requests for offline reconstruction also helped to mitigate the pressure on the offline computing model.

2.7.1 Level-0 hardware trigger

The L0 trigger is divided into three independent components: the L0-Calorimeter trigger, the L0-Muon trigger and the L0-PileUp trigger. The latter is used to reject multiple visible interactions in a bunch crossing by means of the "ad hoc" *Pile-Up System* detector housed in the VELO. The first two components are briefly described below.

The L0-Calorimeter part of the trigger obtains informations from the SPD, PS, ECAL and HCAL subdetectors and computes the transverse energy deposited by incident particles: $E_T = E_0 \cos\theta$, where E_0 is the energy of the particle and θ is the polar angle given by the cell hit in the detector. Together with energy information, the total number of hits in the SPD (SPD multiplicity) is also determined in order to veto large multiplicity events that would take too large a fraction of the available processing time in the HLT. From the calorimeter information, three types of candidates are built and selected according to specific E_T criteria: i) hadron candidate (L0Hadron); ii) photon candidate (L0Photon); and iii) electron candidate (L0Electron).

The L0-Muon part of the trigger requires a muon candidate to have a hit in all five muon stations. The L0 muon processor boards select the two highest p_T muon tracks in each quadrant of the muon system with a maximum of eight candidates. The trigger sets a single threshold either on the largest muon p_T (L0 muon trigger) or on the product of the largest and the 2nd largest (L0 dimuon trigger). Events with SPD multiplicity $>$ 600 are excluded in the L0 muon trigger in order to minimise the track multiplicity. This limit is raised to 900 in the L0 dimuon trigger at the expense of a small increase in rate.

The total output rate of the L0 trigger is limited to 1 MHz, which is the maximum rate accepted by the HLT1. Such an output rate consists of about 400 kHz of muon triggers, about 450 kHz of hadron triggers and about 150 kHz of electron and photon triggers (the individual triggers have an overlap of about 10%).

2.7.2 High-level trigger

Data from L0 are sent to the Event Filter computer Farm (EFF) which runs the HLT algorithms. The HLT is a software application whose 29500 instances run on the EFF. Each instance is made up of independently operating trigger lines; each line consists of selection parameters for a specific class of events.

The HLT is divided into two stages. The first stage (HLT1) processes the full L0 rate and uses partial event reconstruction to reduce the rate to about 110 kHz. The second stage (HLT2) reduces the rate to about 12.5 kHz, performimg a more complete event reconstruction [41].

HLT1 reconstructs the trajectories of charged particles traversing the full LHCb tracking system which have a p_T larger than 500 MeV. The hits in the VELO are combined to form straight-line tracks loosely pointing towards the beam line. Next, at least three hits in the TT are required in a small region around a straight-line extrapolation from the VELO. The TT is located in the fringe field of the LHCb dipole magnet, which allows the momentum to be determined with a relative resolution of about 20%, and this estimate is used to reject low p_T tracks. Tracks are then extrapolated to the T-stations downstream of the magnet. The search window in the IT and OT is defined by the maximum possible deflection of charged particles with p_T larger than 500 MeV. The search is also restricted to one side of the straight-line extrapolation by the charge estimate of the track. Subsequently, all tracks are fitted with a Kalman filter to obtain the optimal parameter estimate using a simplified geometry description of the LHCb detector. The set of fitted

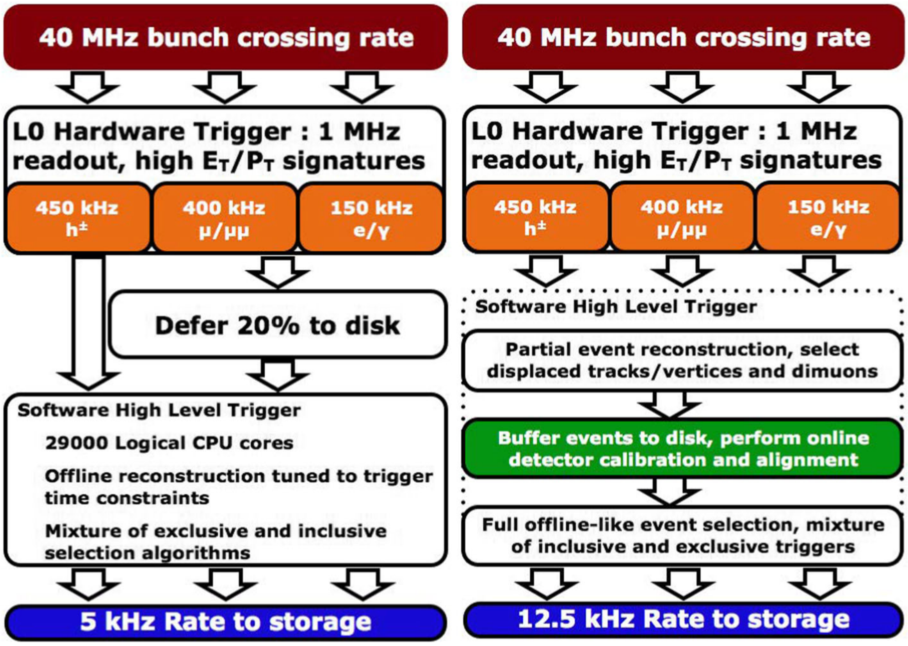

Fig. 13 Trigger overview in Run 1 (left) and Run 2 (right)

VELO tracks is re-used to determine the positions of the PVs.

Tight timing constraints in HLT1 mean that most particle-identification algorithms cannot be executed. The exception is muon identification due to its clean signature. Hits in the muon stations are searched for in momentum-dependent regions of interest around the track extrapolations. Tracks with $p < 3$ GeV cannot be identified as muons, as they would not be able to reach the muon detectors.

HLT1 has two inclusive trigger lines which select events containing a particle whose decay vertex is displaced from the PV: a line which selects a single displaced track with high p_{T}, and a line which selects a displaced two-track vertex with high p_{T}. Both lines start by selecting good quality tracks that are inconsistent with originating from the PV. The single-track trigger then selects events based on a hyperbolic requirement in the 2D plane of the track displacement and p_{T}. The two-track displaced vertex trigger selects events based on a multivariate discriminant whose input variables are the vertex-fit quality, the vertex displacement, the scalar sum of the p_{T} of the two tracks and the displacement of the tracks making up the vertex. The two-track line is more efficient at low p_{T}, whereas the single track line performs better at high p_{T}, such that in combination they provide high efficiency over the full p_{T} range.

The HLT1 muon lines select muonic decays of b and c hadrons, as well muons originating from decays of W and Z bosons. There are four main lines: one line that selects a single displaced muon with high p_T, a second single muon line that selects very high p_T muons without displacement for electroweak physics, a third line that selects a dimuon pair compatible with originating from a decay of a charmonium or bottonium resonance or from Drell-Yan production, and a fourth line that selects displaced dimuons with no requirement on the dimuon mass. During Run 2, typically about 80 kHz were allocated to the inclusive HLT1 lines, while about 20 kHz to the muon lines. The rest of the HLT1 output is dedicated to special low multiplicity triggers and calibration trigger lines.

HLT2 can perform the full-event reconstruction since the output of HLT1 is buffered. The full-event reconstruction consists of three major steps: the track reconstruction of charged particles, the reconstruction of neutral particles and particle identification. The HLT2 track reconstruction exploits the full information from the tracking sub-detectors, performing additional steps of the pattern recognition which are not possible in HLT1. Tracks with a p_{T} larger than 80 MeV are reconstructed in HLT2, without the requirement to have hits in the TT station. This is to avoid inefficiencies due to the TT acceptance, which is crucial for part of the charm and kaon physics programme. In addition, tracks produced by long-lived resonances that decay outside the VELO are reconstructed using T-station segments that are extrapolated backwards through the magnetic field and combined with hits in the TT. Similarly, the most precise neutral cluster reconstruction algorithms are executed. Finally, in addition to the muon identification available in HLT1, HLT2 exploits the full-particle identification from the RICH detectors and calorimeter system.

The HLT2 inclusive b-hadron trigger lines look for a two-, three-, or four-track vertex with sizeable p_{T}, significant displacement from the PV, and a topology compatible with the decay of a b-hadron, using a multivariate discriminant. Whenever one or more tracks are identified as muons, the requirements on the discriminant are relaxed to increase the efficiency. As in the case of HLT1, several muon lines are used to select muonic decays of b and c hadrons and of W and Z bosons. However in HLT2, the muon reconstruction is identical to the offline procedure, having access to exactly the same information. During Run 2, typically about 3 kHz of the trigger rate is from the inclusive b-hadron trigger while the muon lines take about 1 kHz. A large fraction of the trigger bandwidth (2-4 kHz) is allocated to exclusive selection of charm decays, where a reduced amount of information is saved per event. The rest of the trigger bandwidth is due to other special triggers and calibration trigger lines.

3 LHCb contributions to CKM measurements and *CP* violation

The violation of the combined operation of charge conjugation and parity, *CP*, was first observed in 1964 in decays of neutral kaons [43]. The BaBar [44] and Belle [45] B Factory experiments and the CDF experiment [46] established *CP* violation in the decays of neutral B^0 mesons. LHCb now extends measurements to much greater precision, and also probes the B_s system, which is vital to explore the full range of *CP* violation measurements.

In the Standard Model, the Cabibbo–Kobayashi–Maskawa (CKM) unitary matrix [4,47], V_{CKM}, describes the electroweak coupling strength V_{ij} of the W boson to quarks i and j:

$$V_{\mathrm{CKM}} = \begin{pmatrix} V_{ud} & V_{us} & V_{ub} \\ V_{cd} & V_{cs} & V_{cb} \\ V_{td} & V_{ts} & V_{tb} \end{pmatrix}. \tag{3.1}$$

CP is violated in the Standard Model if any element of the CKM matrix is complex. The parametrisation of the CKM matrix due to Wolfenstein [48] is given by

$$V_{\mathrm{CKM}} = \begin{pmatrix} 1-\frac{1}{2}\lambda^2-\frac{1}{8}\lambda^4 & \lambda & A\lambda^3(\rho-i\eta) \\ -\lambda+\frac{1}{2}A^2\lambda^5[1-2(\rho+i\eta)] & 1-\frac{1}{2}\lambda^2-\frac{1}{8}\lambda^4(1+4A^2) & A\lambda^2 \\ A\lambda^3[1-(1-\frac{1}{2}\lambda^2)(\rho+i\eta)] & -A\lambda^2+\frac{1}{2}A\lambda^4[1-2(\rho+i\eta)] & 1-\frac{1}{2}A^2\lambda^4 \end{pmatrix} \tag{3.2}$$

for the four Standard Model parameters (λ, A, ρ, η). The expansion parameter, λ, equal to the sine of the Cabibbo angle, has a value $|V_{us}| = 0.22$ [49], and in Eq. 3.2 the expansion is given for terms up to order λ^5.

The unitarity of the CKM matrix leads to six orthogonality conditions between any pair of columns or any pairs of rows of the matrix. The orthogonality means the six conditions can be represented as six triangles in the complex plane. The interesting relations for *CP* violation are those given by:

$$V_{ud}V_{ub}^* + V_{cd}V_{cb}^* + V_{td}V_{tb}^* = 0 \quad \text{: the unitarity triangle,} \tag{3.3}$$

$$V_{us}V_{ub}^* + V_{cs}V_{cb}^* + V_{ts}V_{tb}^* = 0 \quad \text{: the } B_s \text{ triangle, and} \tag{3.4}$$

$$V_{cd}V_{ud}^* + V_{cb}V_{ub}^* + V_{cs}V_{us}^* = 0 \quad \text{: the charm triangle.} \tag{3.5}$$

The unitarity triangle has sides with lengths that are the same order in λ, namely $\mathcal{O}(\lambda^3)$, which implies large *CP* asymmetries in B^0 and $B^{\pm}$ decays. The B_s triangle has two sides of $\mathcal{O}(\lambda^2)$ and the third of $\mathcal{O}(\lambda^4)$. Hence, *CP* violation in B_s mixing is significantly smaller than in the B^0 system. Moreover, the charm triangle has two sides of $\mathcal{O}(\lambda)$ and the third of $\mathcal{O}(\lambda^5)$, hence *CP* violation in the charm system is expected to be extremely small. Note that all three triangles have equal area [50].

To study *CP* violation, the $B-$physics experiments measure the complex phases of the CKM elements and measure the lengths of the sides of the triangles to check for a self-consistent picture. *CP* violation is predicted in many (often very rare) B hadron decays; hence, LHCb utilises large samples of B, B_s, B_c mesons and $B-$baryons. New physics can be discovered and studied when new particles appear in, for example, virtual loop processes of rare B decays, leading to observable deviations from Standard Model expectations, both in branching ratios and *CP* observables. Hence, the LHCb strategy is to determine with high precision the CKM elements and to compare measurements of the same parameters, especially those where one is sensitive to new physics and the other to Standard Model processes.

3.1 The status of the unitarity triangle before LHCb

The first generation B Factory experiments to study *CP* violation in the $B-$system, BaBar and Belle, made huge in-roads into testing the Standard Model description of *CP* violation; the status was summarised extensively at the Beauty 2009 Conference [51]. CDF and D0 extended these studies at the Tevatron, and make first explorations in the B_s sector. Figure 14 shows the status of the unitarity triangle measurements compiled by the CKM-Fitter Group [52] in 2009, when the B Factories had been running for around ten years. Here graphical results are displayed in the $\rho-\eta$ plane and the best fit to the apex of the triangle (Eq. 3.3) to the 95% confidence level is shown. The fit to the CKM parametrisations include measurements of the sides of the triangle through measurements of the CKM ele-

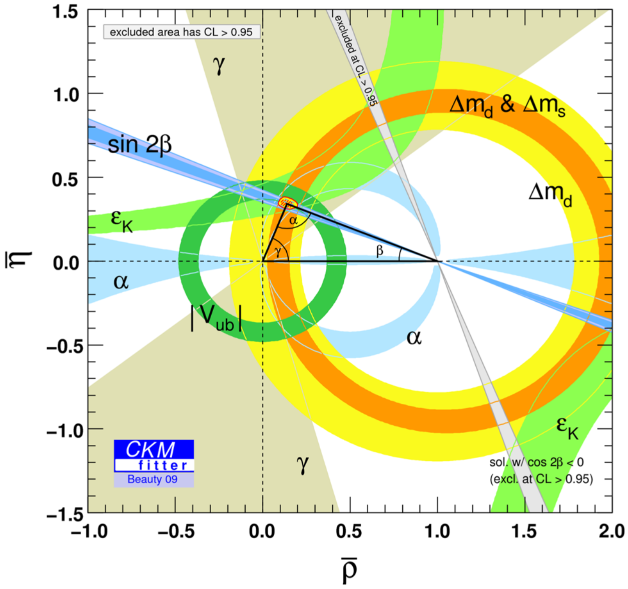

Fig. 14 The knowledge of the unitarity triangle as of autumn 2009 [52]

ments and the angles, information from rare K and B meson decays, and $B_s^0 - \overline{B_s^0}$ mixing.

Before 2009, when the LHC turned on, the B Factory experiments, CDF and, to a lesser degree D0, measured the parameters of the unitarity triangle with varying degrees of precision:

- The quantity $\sin 2\beta$ was measured in all channels, including the "gold plated" channel $B^0 \to J/\psi K_S^0$, to a precision of around $\sim$0.03;
- The sides $|V_{td}/V_{ts}|$ and $|V_{ub}/V_{cb}|$ were known from $B_s^0 - \overline{B_s^0}$ mixing and from $b \to u$ decays, respectively, each to $\sim$10%, but limited by theory. Only preliminary measurements had been made of the B_s mixing phase (ϕ_s) by CDF and D0 [53,54];
- The angle α was measured in the channels $B \to \pi\pi$, $\rho\pi$ and $\rho\rho$ with a statistical precision of $\sim 5°$;
- There was a statistics-limited measurement in $B \to DK$ modes of the angle γ to around $20 - 25°$. A measurement of γ from B_s modes such as $B_s^0 \to D_s^+ K^-$ had been completely unexplored.
- The parameter ε_K, measured in kaon decays, provided a very loose constraint on the triangle vertex;
- The B_s sector had been largely unexplored by the first-generation experiments, as had $b-$baryons. Running at the $\Upsilon(4S)$, the B Factories produced predominantly $B_{u,d}$ meson pairs; however, Belle recorded a significant sample of $\Upsilon(5S)$ data, allowing some interesting measurements of B_s pairs. At the LHC, B^0, $B^\pm$, B_s, B_c and $b-$baryons are produced in approximately in the ratios $\sim 40 : 40 : 10 : 0.1 : 10\%$;
- The B Factories were statistics limited for very rare processes with branching ratios $\lesssim 1 \times 10^{-6}$, such as $b \to s$ flavour-changing neutral current (FCNC) transitions, e.g. $b \to s\gamma$ and $b \to sl^+l^-$. Super-rare transitions such as $B_{(s,d)} \to \mu^+\mu^-$ were also unobserved.

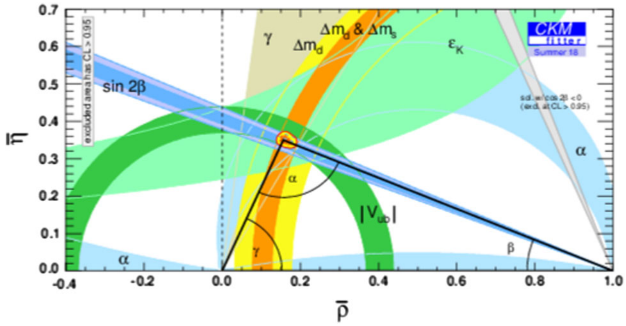

Fig. 15 The current knowledge of the unitarity triangle (as of Summer 2019) [52]

In contrast, Fig. 15 shows the status of the unitarity triangle measurements today [52].

3.2 Heavy quark mixing measurements

Since flavour is not conserved in the weak interaction, mixing between B_q^0 and $\overline{B}_q^0$ mesons (where $q = d$ or s) is possible via the box diagrams shown in Fig. 16. The probability for finding a $\overline{B}_q$ (or a B_q), given the initial state was a B_q (or a $\overline{B}_q$) at time Δt after production, is given by:

$$P_{mix}(\Delta t) = \exp - \frac{\Delta t}{\tau_{B^0}} \left(1 - \cos(\Delta m_q \Delta t)\right). \qquad (3.6)$$

Here Δm_q is the mass difference $m_H - m_L$, where $m_{H,L}$ are the masses of the heavy and light mass eigenstates and τ_{B^0} is the B lifetime. At the LHC, the two neutral B mesons produced can oscillate independently at any time after production.

Any CP measurement from a time-dependent analysis of neutral B decays needs the determination of the B flavour (b or $\bar{b}$) at production. This requires $b-$quark "tagging", and several algorithms have been developed by LHCb involving the combination of so-called opposite side [55] and same side taggers [56].

- $\boldsymbol{B^0}$ **mixing:** B^0 oscillations are measured in the channel $B^0 \to D^- \mu^+ \nu_\mu X$ and the charge conjugate modes. The oscillation measurements rely on tagging, and are shown for 3 fb^{-1} of data in Fig. 17 (left). The LHCb Δm_d measurement, which is the world's best, is $\Delta m_d = (505.0 \pm 2.1 \pm 1.0)$ ns^{-1} [57].
- $\boldsymbol{B_s}$ **mixing:** $B_s^0 - \overline{B}_s^0$ oscillations were first observed by CDF [58]. B_s oscillations are measured at LHCb in the mode $B_s^0 \to D_s^- \pi^+$ and its charge conjugate state. The oscillations are shown for 1 fb^{-1} of data in Fig. 17 (right). The plot shows the proper-time distribution of $B_s^0 \to D_s^- \pi^+$ candidates, in five different B_s^0 decay channels, that have been flavour-tagged as not having oscillated. The LHCb Δm_s

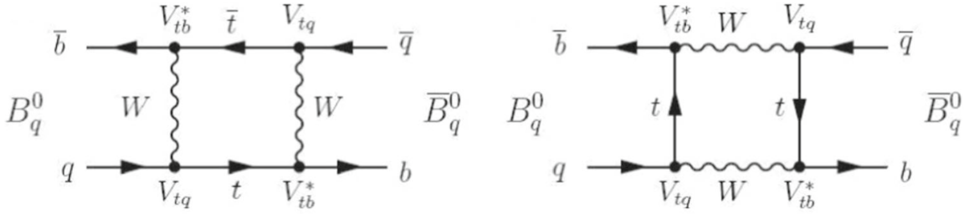

Fig. 16 The box diagrams representing mixing between B_q^0 and $\overline{B}_q^0$ mesons

measurement, which is again the world's best, is $\Delta m_s = (17.768 \pm 0.023 \pm 0.006)\,\text{ps}^{-1}$ [59].

- **Charm meson mixing:**
  $D^0 - \overline{D}^0$ mixing was established in a single experiment in 2013 by LHCb in $D^0 \to K^+\pi^-$ decays, although it was confirmed earlier by combining several B Factory results. The D^0 mixing parameters were measured in LHCb in a decay-time-dependent fit to the ratio $\frac{N_{D^0\to K^+\pi^-}}{N_{D^0\to K^-\pi^+}}$. The time-dependent fit is shown in Fig. 17 (lower) for 1 fb^{-1} of data. The no-mixing scenario is excluded at 9.1σ [60].

3.3 LHCb measurements of the unitarity triangle parameters

The LHCb experiment performs a high-statistics study of *CP* violation with unprecedented precision in many different and complimentary channels, providing a sensitive test of the Standard Model and physics beyond it.

3.3.1 Measurements of the CKM angle β

The time-dependent decay asymmetry of the channel $B^0 \to J/\psi K_S^0$ allows a measurement of the angle β. This is known as the "golden" decay mode because the channel is virtually free of penguin pollution (which enters with the same overall phase), resulting in very small theoretical uncertainty, of order 1% [61]. *CP* violation in this channel occurs in the interference between mixing and decay, where the mixing process introduces a relative *CP*-violating weak phase of 2β. Experimentally the *CP* asymmetry is measured from the ratio of the numbers of $\overline{B}$ and B mesons, $N_{\overline{B}\to f}$ and $N_{B\to f}$, decaying into final state f:

$$\begin{aligned}\mathcal{A}_{\mathcal{CP}} &= \frac{N_{\overline{B}\to f} - N_{B\to f}}{N_{\overline{B}\to f} + N_{B\to f}}\\ &= \sin(\Delta m_d t)\,\sin(2\beta) - \cos(\Delta m_d t)\,\cos(2\beta).\end{aligned} \tag{3.7}$$

The LHCb measured and fitted asymmetries for the $J/\psi\,(1S)$ and $(2S)$ states are shown in Fig. 18 for 3 fb^{-1} of data at 7 and 8 TeV [62]. These measurements are $\cos(\Delta m_d t) = -0.017 \pm 0.029$ and $\sin(\Delta m_d t) = 0.760 \pm 0.034$, where an observation of a direct *CP*-violation contribution proportional to $\cos(\Delta m_d t)$ would be an indication of new physics [61]. The LHCb measurement is now competitive with BaBar and Belle measurements; the current world average of $\sin 2\beta = 0.695 \pm 0.019$ [63] is dominated by LHCb together with the B Factory measurements in the complementary channels $B^0 \to J/\psi K_S^0$ and $B^0 \to J/\psi K_L^0$. The measurement by LHCb of $\sin 2\beta$ in gluonic penguins will further contribute to this study.

3.3.2 Measurements of the CKM angle α

The primary method at LHCb for the measurement of α is through an amplitude analysis via the $B \to \rho\pi$ decay modes [64]; however, these channels are difficult at LHCb due to the need to efficiently reconstruct π^0s. Penguin pollution is present and must be constrained, with the additional application of isospin symmetry. The precision on α at LHCb is expected to be dominated by systematic uncertainties, and any measurement is not expected to improve on a combination of the B Factory measurements, $\alpha = \left(86.4^{+4.5}_{-4,3}\right)^\circ$ [52].

3.3.3 Measurements of the CKM angle γ

A precise measurement of the angle γ is key to understand the closure (or otherwise) of the unitarity triangle. Constraints on the unitarity-triangle apex largely come from loop decay measurements which are very sensitive to the presence of new physics. γ is the only angle accessible at tree level and hence forms a SM benchmark to which the loop measurements can be compared (assuming no significant new physics in tree decays). The γ measurement also relies on theoretical input which is very well understood [65,66].

Determination of γ from a combined fit to all measured parameters of the unitarity triangle currently gives a value $\gamma = \left(65.8^{+1.0}_{-1.7}\right)^\circ$ [52]. Conversely the measurement of γ alone from a combination of all direct measurements from tree decays gives $\gamma = \left(72.1^{+5.4}_{-5.7}\right)^\circ$. Hence, reaching degree-level precision from direct γ measurements is crucial.

LHCb makes measurements of γ by a variety of methods, where complementary is vital. Examples of the most sensitive LHCb measurements are outlined below.

- **γ in the "time integrated" $B^\pm \to D^0 K^\pm$ modes**
  The measurement of γ is made in direct CP-violation via $B^\pm \to D^0 K^\pm$ by three different methods: the GLW method (decay into a *CP* eigenstate) [67,68], the ADS method (decay into a

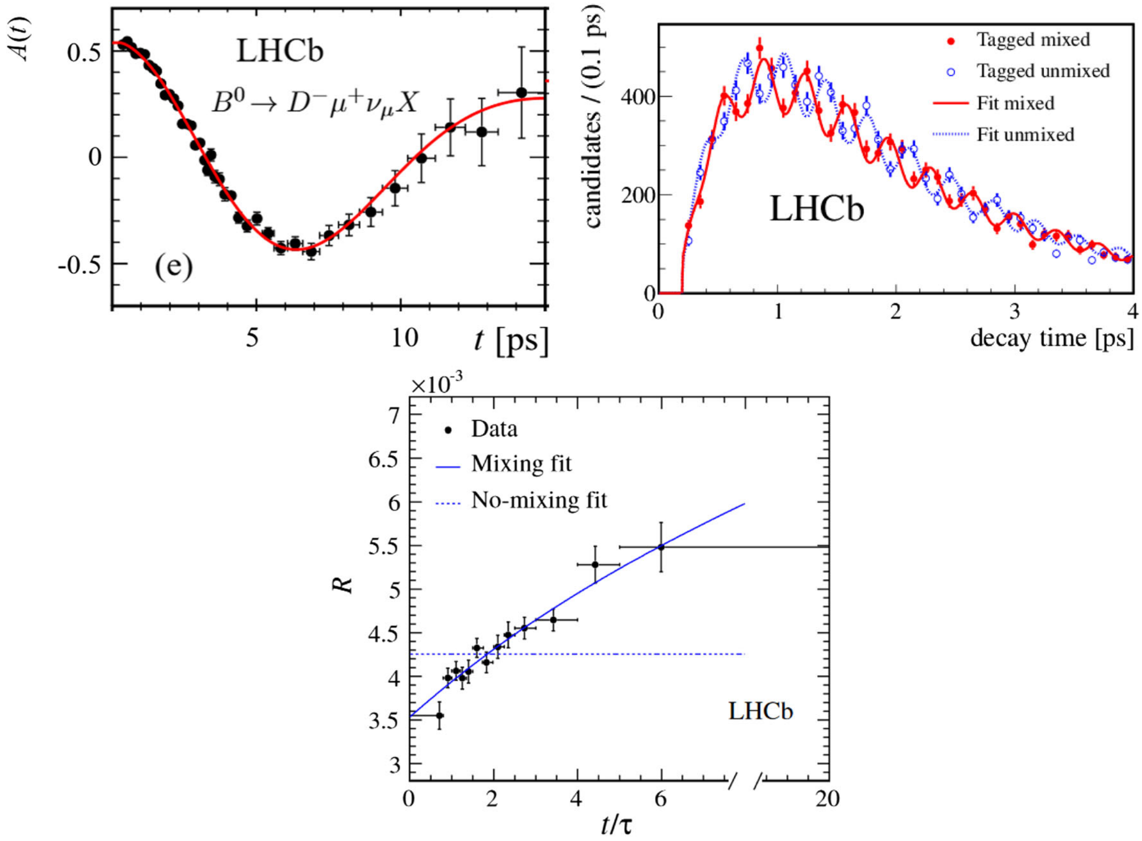

Fig. 17 Proper-time distribution of (left) $B^0 - \overline{B}^0$ oscillations in $B^0 \to D^- \mu^+ \nu_\mu X$ decays, (right) $B_s^0 - \overline{B}_s^0$ oscillations in $B_s^0 \to D_s^- \pi^+$ decays, and (lower) $D^0 - \overline{D}^0$ oscillations in $D^0 \to K^+ \pi^-$ decays. All distributions rely on flavour tagging, and the curves correspond to the fitted oscillations

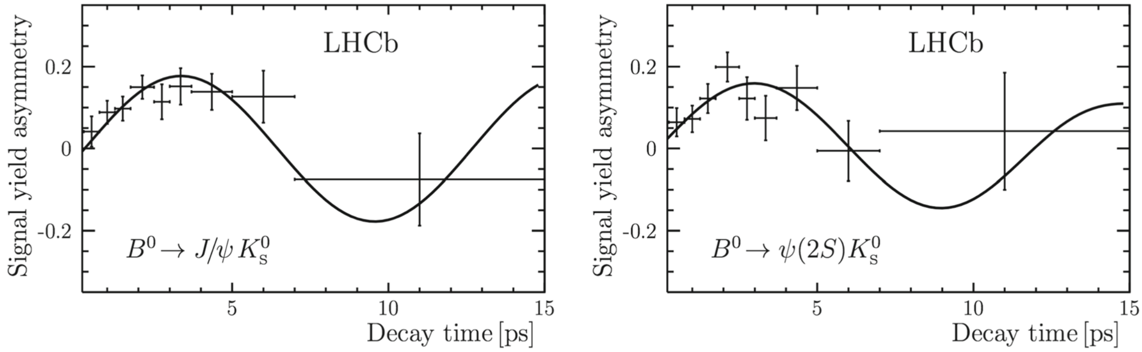

Fig. 18 The LHCb measured and fitted asymmetry in $B^0 \to J/\psi K_S^0$ decays for (left) the $J/\psi(1S)$ and (right) the $\psi(2S)$

Fig. 19 Example of a *CP* asymmetry in the ADS mode $B^\pm \to D^0 K^\pm$, where the D^0 and $\overline{D}^0$ both decay into $K^+ \pi^-$. The event yield is shown as a function of *DK* mass

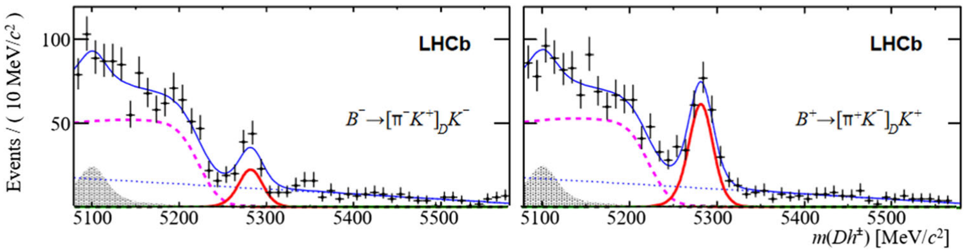

flavour-specific mode) [69] and the GGSZ method (Dalitz analysis) [70]. These all access γ through interference between the $B^\pm \to D^0 K^\pm$ and $B^\pm \to \overline{D}^0 K^\pm$ decay paths, where the D^0 and $\overline{D}^0$ decay to the same final state. When using these methods, the decay modes are self-tagging. In addition, time-dependent analyses are not necessary. For the ALD and GLW modes, the charge-conjugate event yields are simply counted to determine the CP asymmetries (i.e. effectively a "counting experiment").
Figure 19 shows an example of a *CP* asymmetry in the $B^\pm \to D^0 K^\pm$ ADS mode [71]. Here the D^0 is produced in a Cabibbo favoured mode (V_{cb}) but decays via a suppressed mode (V_{cd}) into $K^+\pi^-$. This interferes with the $\overline{D}^0$ charge-conjugate state which is produced in a suppressed mode (V_{ub}) but decays to the same final state $K^+\pi^-$ via a favoured mode (V_{cs}). The branching fraction for the favoured B decay is only $\sim 10^{-4}$, so these measurements require high statistics. The asymmetry observed in Fig. 19 has a magnitude of around 40% and has a significance of 7σ.
A specific example of an LHCb analysis using the GGSZ Dalitz method is in the decay $B^\pm \to D^0 K^\pm$ where $D^0 \to K^0_S \pi^+\pi^-$ or $D^0 \to K^0_S K^+ K^-$ [72]. There is a rich Dalitz plot structure with the presence of large interference effects. The Dalitz space is divided up into symmetric bins, chosen to optimise sensitivity. An amplitude analysis can then be used to extract γ.
In all $B^\pm \to D^0 K^\pm$ modes and decays listed above, γ can also be extracted from the corresponding $B^\pm \to D^0 K^{\star\pm}$ modes, albeit with reduced γ sensitivity. In addition $B^0 \to D^{(*)} K^{(*)}$, GGSZ modes are also included in the global fit to extract the γ average value.

- **γ from the "time-dependent" $B_s^0 \to D_s^- K^+$ mode**
The channel $B_s^0 \to D_s^- K^+$, and its charge conjugate states, provide a theoretically clean measurement of the angle $(\gamma + \phi_s)$ where ϕ_s is the (small valued) B_s mixing phase, with no significant penguin contribution expected [73]. Here both B_s^0, and via the mixing diagram $\overline{B}_s^0$, can decay to the same final state $D_s^- K^+$, resulting in interference which is sensitive to γ. The same is true for decay into the charge conjugate state $D_s^+ K^-$. Hence, four time-dependent decay rates are measured: $B_s^0 \to D_s^- K^+$, $B_s^0 \to D_s^+ K^-$, $\overline{B}_s^0 \to D_s^- K^+$ and $\overline{B}_s^0 \to D_s^+ K^-$. The method is then to fit two asymmetries of the form

$$\mathcal{A}_{C\mathcal{P}} = \frac{N_{\overline{B}\to f} - N_{B\to f}}{N_{\overline{B}\to f} + N_{B\to f}}\,. \tag{3.8}$$

These measurements yield values for the strong phase difference δ_{QCD} between the amplitudes $B \to f$ and $\overline{B} \to f$, the amplitude ratio, and $(\gamma + \phi_s)$. The current measurement by LHCb in 1 fb^{-1} of data yields a value $\gamma = \left(115^{+28}_{-43}\right)^\circ$ [74]. This complements the measurements in $B^\pm \to D^0 K^\pm$, although with less statistical precision.

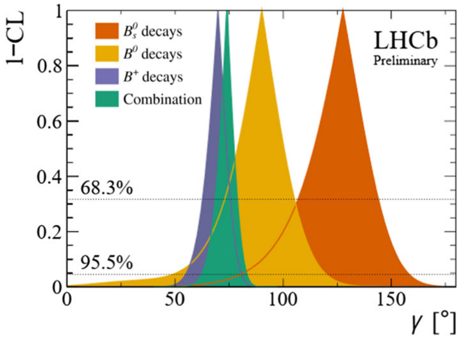

Fig. 20 Confidence limits as a function of γ in the LHCb combination for the various measurement channels

- **The γ combination**
The LHCb measurement of γ averaged over all the above methods, which includes all $B^0, B^\pm$ and B_s modes, is $\gamma = \left(74.0^{+5.0}_{-5.8}\right)^\circ$ [75]. This measurement dominates the current world average. The confidence limits as a function of γ for the combination are shown in Fig. 20 for the various measurement channels. The agreement between B_s and $B^\pm$ initial states is currently at the 2σ level.

3.3.4 The sides of the triangle

- **The side opposite to β**
Currently the closure test of the unitarity triangle is limited mainly by the side opposite to β which has a length proportional to $|V_{ub}|/|V_{cb}|$ in the Standard Model. This limitation is a consequence of tension between B Factory inclusive and exclusive $|V_{ub}|$ measurements which differ by $\sim 3.5\sigma$ [63].
$|V_{ub}|^2$ is directly proportional to the decay rate $B^0 \to X_u \mu^- \nu_\mu$, where X_u is a meson containing a u quark. Theoretical input from Heavy Quark Effective Theory and lattice calculations are also necessary to calculate $|V_{ub}|$, although several of the theoretical uncertainties cancel in the ratio to calculate the side.
$|V_{ub}|/|V_{cb}|$ is a very difficult measurement at LHCb due to presence of a neutrino, the identification of which was never in LHCb's original plans. Although the B Factory favoured channel $B^0 \to \pi^+\mu^-\nu_\mu$ cannot currently be identified at LHCb, the equivalent baryonic channel $\Lambda_b \to p\mu^-\nu_\mu$ has been measured. The signal is separated from the lower-mass backgrounds, as shown in Fig. 21. Using form factors from lattice calculations, LHCb measures [76]

$$\begin{aligned}|V_{ub}| &= (3.27 \pm 0.15\,(\mathrm{exp}) \pm 0.17\,(\mathrm{theory})\\ &\quad \pm 0.06\,(|V_{cb}|)) \times 10^{-3}\end{aligned}$$

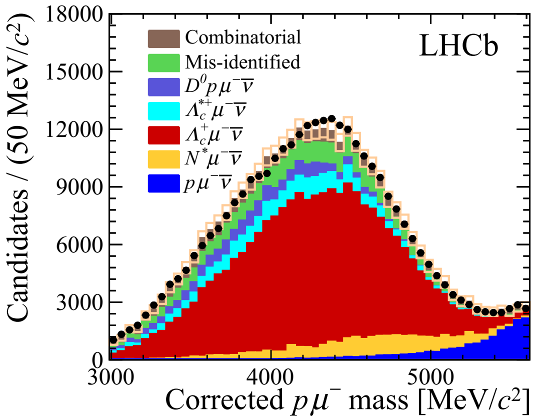

Fig. 21 The $(p\mu^-)$ mass distribution in the measurement of $|V_{ub}|$, showing the contribution from $\Lambda_b \rightarrow p\mu^-\nu_\mu$ decays and the various backgrounds

This is to be compared to the world average of $|V_{ub}| = (3.94 \pm 0.36) \times 10^{-3}$ [63].

- **The side opposite to α**
  The mass difference Δm_s measured in B_s^0 mixing (Fig. 16), which is dominated by the top-quark loop, provides a measurement of the third side of the triangle, $\frac{V_{td}}{\lambda V_{ts}}$. This is proportional to the ratio of mixing frequencies $\sqrt{\frac{\Delta m_d}{\Delta m_s}}$. Corrections are calculated from the lattice with a theoretical error of ∼5-10% and systematic errors largely cancel in the ratio. Following the measurement by LHCb of the mixing parameters presented above, the ratio $|V_{td}/V_{ts}|$ is $0.210 \pm 0.001 \pm 0.008$ [49]. Systematic errors can be reduced in the future by improved lattice QCD calculations.

3.4 Other *CP* violation measurements

3.4.1 B_s weak mixing phase ϕ_s in $B_s^0 \rightarrow J/\psi\phi$

It can be seen in Fig. 16 that V_{ts} appears twice in the $B_s^0 - \overline{B}_s^0$ mixing process, introducing a relative "weak mixing phase", of ϕ_s to fourth order in λ. The B_s mixing phase can be measured in the channel $B_s^0 \rightarrow J/\psi\phi$, which is governed by a single tree-level diagram with a negligible penguin contribution. Hence, this mode is the strange-quark analogue of the golden mode $B^0 \rightarrow J/\psi K_S^0$ in the B^0 system. In the B_s system, *CP* asymmetry arises from the interference of the $B_s^0 \rightarrow J/\psi\phi$ with the mixed process $B_s^0 \rightarrow \overline{B}_s^0 \rightarrow J/\psi\phi$. In the Standard Model, ϕ_s is expected to be very small, $\sim 0.036 \pm 0.002$ rad [52]; hence, this channel is a very sensitive probe for new physics.

LHCb reconstructs $B_s^0 \rightarrow J/\psi\phi$ events in the decay modes $J/\psi \rightarrow \mu^+\mu^-$, and $\phi \rightarrow K^+K^-$ [77]. This B_s^0 final state is an admixture of *CP*-even and odd contributions; therefore, an angular analysis of decay products is required. Good tagging performance of B_s^0 and $\overline{B}_s^0$ is important, with a total tagging power in this analysis of $4.73 \pm 0.34\%$.

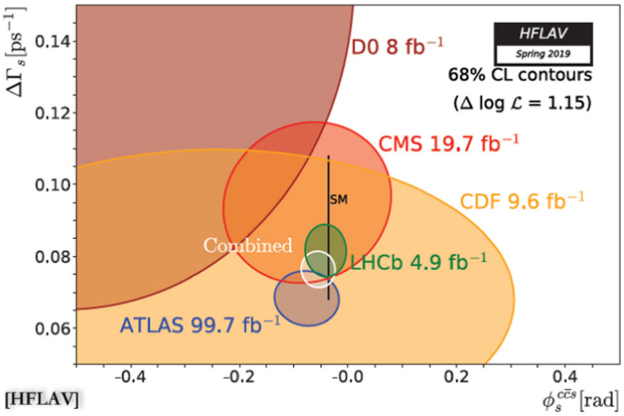

Fig. 22 The measurement of the B_s^0 weak mixing phase in the $(\phi_s, \Delta\Gamma_s)$ plane, showing the LHCb result in combination with those from other experiments, the Standard Model expectation and the 1σ contour of the combination [63]

The fitted value of ϕ_s is correlated with $\Delta\Gamma_s$, the width difference of the B_s^0 mass eigenstates. The decay $B_s^0 \rightarrow J/\psi\pi^+\pi^-$ is also added to improve the sensitivity [78]. Contours in the $(\phi_s, \Delta\Gamma_s)$ plane are plotted in Fig. 22. The LHCb measurements are $\Delta\Gamma_s = 0.0816 \pm 0.0048$ ps^{-1} with the *CP*-violating phase $\phi_s = -0.041 \pm 0.025$ rad. Figure 22 also shows the world-averaged measurement of ϕ_s versus $\Delta\Gamma_s$ showing the LHCb result in combination with those from other experiments and the Standard Model expectation [63].

3.4.2 *CP* violation in charm

The Standard Model prediction of *CP* violation in the charm system is expected to be very small $\mathcal{O}\left(10^{-4}\right) \rightarrow \mathcal{O}\left(10^{-3}\right)$, where *CP* violation can arise in Cabibbo-suppressed (CS) decays in the interference between tree and penguin amplitudes. In particular, LHCb has measured asymmetries in the direct *CP*-violating channels $D^0(\overline{D}^0) \rightarrow \pi^+\pi^-$ and $D^0(\overline{D}^0) \rightarrow K^+K^-$ [79].

In the LHCb analysis, D^0 and $\overline{D}^0$ decays are identified via two self-tagging decay paths. "Prompt" decays (D decays originating from the primary vertex) are characterised by the presence of a "soft" low-momentum pion from a D^*, i.e. $D^{*+} \rightarrow D^0\pi^+_{\mathrm{soft}}$ and the charge-conjugate mode. "Semileptonic" decays are secondary D's which originate from prompt B decays, i.e. $B^+ \rightarrow \overline{D}^0\mu^+X$ and the charge-conjugate states.

The raw asymmetry ($\mathcal{A}$) for $D^0 \rightarrow h^+h^-$ decays ($h = K$ or π) is defined as

$$\mathcal{A}(D \rightarrow f) = \frac{N(D \rightarrow f) - N(\overline{D} \rightarrow \overline{f})}{N(D \rightarrow f) + N(\overline{D} \rightarrow f)} \tag{3.9}$$

which includes both physics and detector terms: $\mathcal{A} = \mathcal{A}_{CP} + \mathcal{A}_D + \mathcal{A}_P$. Detection asymmetry arises from small charge differences associated with the $\pi^{\pm}_{\text{soft}}$ or $\mu^{\pm}$. Production asymmetry arises from different production rates of D^* and B in pp collisions. To eliminate these two contributions and cancel associated systematics, the $\Delta\mathcal{A}_{CP}$ parameter is measured in LHCb:

$$\begin{aligned} \Delta\mathcal{A}_{CP} &= \mathcal{A}\left(K^+K^-\right) - \mathcal{A}\left(\pi^+\pi^-\right) \\ &= \mathcal{A}_{CP}\left(K^+K^-\right) - \mathcal{A}_{CP}\left(\pi^+\pi^-\right). \end{aligned} \tag{3.10}$$

The raw symmetries are obtained from mass fits, and then by simply counting the numbers of D's decaying to $\pi^+\pi^-$ and K^+K^-, respectively.

A measurement performed with Run 1 and Run 2 LHCb data combined gives $\Delta\mathcal{A}_{CP} = (-15.4 \pm 2.9) \times 10^{-4}$. This is a 5.3σ measurement of CP violation in the charm system and opens a new window for the study of CP violation in the future.

3.4.3 *CP* violation in beauty baryons

CP violation has been observed in B, K, and D decays, but not yet in baryon decays. A search for CP violation in the multi-body mode $\Lambda_b^0 \rightarrow p^+\pi^-\pi^+\pi^-$ was performed on LHCb Run 1 data [80]. This decay proceeds via tree and loop diagrams with similar contributions and through numerous intermediate resonances, enhancing the possibility for CP violation, although in areas where re-scattering effects can play a role. A 3.3σ deviation from CP symmetry was observed; however, introducing 6.6 fb^{-1} of Run 2 data has not confirmed this result [81]. Hence, this measurement awaits further statistics and will be improved when cleaner 2-body B-baryon decays can be added to the study.

3.4.4 *CP* violation in charmless 3-body $B^{\pm}$ decays

Yields of $B^+ \rightarrow \pi^+K^+K^-$ and $B^- \rightarrow \pi^-K^-K^+$ decays show striking asymmetries in the region of phase space dominated by re-scattering effects [82]. Similarly huge CP-violating effects between $B^+ \rightarrow \pi^+\pi^+\pi^-$ and $B^- \rightarrow \pi^-\pi^-\pi^+$ decays are observed in a region of phase space including the $\rho^0(770)$ and $f_2(1270)$ resonances [83,84]. Figure 23 shows an example of the spectacular asymmetries observed in $B \rightarrow \pi KK$ decays, which exceed 50% at low values of K^+K^- mass.

4 Rare decays

Within the SM, the interplay of weak and Higgs interactions implies that flavour changing neutral currents (FCNCs) can occur only at higher orders in the electroweak interactions and are strongly suppressed by the GIM mechanism. This strong suppression makes FCNC processes natural candidates to search for physics beyond the SM. If the new degrees of freedom do not have the same flavour structure of the quarks/leptons-Higgs interactions present in the SM, then they could contribute to FCNCs at a comparable (or even larger) level to the SM amplitudes.

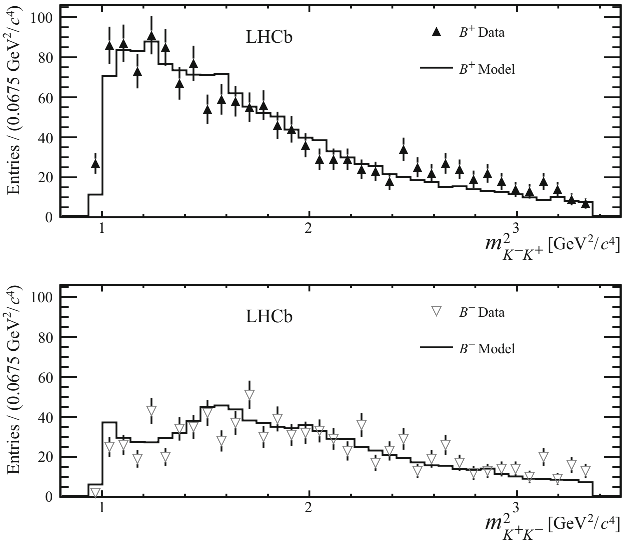

Fig. 23 Yields of (top) $B^+ \rightarrow \pi^+K^+K^-$ and (bottom) $B^- \rightarrow \pi^-K^-K^+$ decays as a function of K^+K^- mass squared

In B-meson decays, experimenters have measured $b \rightarrow s$ and $b \rightarrow d$ quark transitions, while $c \rightarrow u$ and $s \rightarrow d$ transitions have been measured in D-meson and K-meson decays, respectively. At first order, these transitions can occur through two kinds of Feynman diagram shown in Fig. 24. The first corresponds to the so-called box diagram and describes the mixing between neutral mesons, discussed in Sect. 3; the example of Fig. 24 shows B_s^0 mixing. The second kind of diagram, the so-called penguin diagram, is responsible for a large variety of FCNC rare decays. The example shown in Fig. 24 is that of a $b \rightarrow s\ell^+\ell^-$ transition. In particular, if the radiated bosons are of electroweak type (Z, W or γ-like), the uncertainties in the calculation of the SM predictions due to non-perturbative QCD effects are drastically reduced as compared with the case where a gluon is radiated. These "electroweak penguins" are the subject of the discussions in this section.

Before the first physics run of the LHC accelerator in 2010, the main contributors to the study of rare B and D-meson decays were the B Factory experiments (BaBar and Belle) and the Tevatron experiments (CDF and D0). However, the production rate of $b\bar{b}$ pairs in the e^+e^- B Factories was typically five orders of magnitude smaller than at the LHC. In addition, the lower pp collision energy of the Tevatron (with a correspondingly reduced $b\bar{b}$ cross section which is proportional to the collision energy), and the detector's reduced trigger acceptance for rare B and D-meson decays, implied that LHCb would already be the most sensitive experiment even after 1 fb^{-1} accumulated in 2011. For example, prior to the LHC, the rarest B-meson decay ever

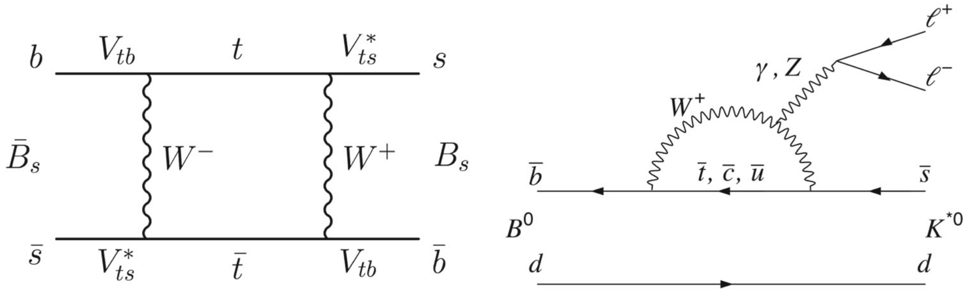

Fig. 24 Examples of loop processes within the SM that allow FCNC $b \to s$ quark transition. On the left is an example of a box diagram and on the right an example of a penguin diagram

measured was $\mathcal{B}(B^+ \to K^+\mu^+\mu^-) \sim 5 \times 10^{-7}$ with a 20% precision; Belle and BaBar had analysed $\mathcal{O}(200)$ $B^0 \to K^{*0}\ell^+\ell^-$ events and CDF had reached a sensitivity of $\mathcal{B}\,(B_s^0 \to \mu^+\mu^-) < 3 \times 10^{-8}$ at the 95% C.L. As will be clear from the next sections, LHCb has already reached after Run 1 of the LHC an order of magnitude larger statistical power.

4.1 $B^0_{(s)} \to \mu^+\mu^-$

The pure leptonic decays of K, D and B mesons are a particular interesting case of electroweak penguins, where the final quark leg in Fig. 24 (right) needs to be swapped to the initial state. The helicity configuration of the purely leptonic final state suppresses the vector and axial-vector contributions by a factor in terms of masses proportional to $\left[\frac{m_\mu}{m_{K,D,B}}\right]^2$. Therefore, these decays are particularly sensitive to new (pseudo-) scalar interactions. In the case of B^0 and B_s^0-meson decays, the contribution of the absorptive part can be safely neglected. As a consequence, the rate is well predicted theoretically [85] : $\mathcal{B}(B_s^0 \to \mu^+\mu^-) = (3.66 \pm 0.05) \times 10^{-9}$ and $\mathcal{B}(B^0 \to \mu^+\mu^-) = (1.03 \pm 0.05) \times 10^{-10}$. In the B_s^0 case, this prediction corresponds to a flavour-averaged time-integrated measurement, taking into account the correction due to the non-negligible width difference.

The experimental signature is sufficiently clean to reach an expected signal over background ratio $S/B \sim 3$ for the B_s^0 decay, assuming the SM branching fraction. The main background in the region around the B_s^0 invariant mass is due to combinations of uncorrelated muons and can be estimated from the mass sidebands. The most important handle to reduce this combinatorial background is the invariant mass resolution of the experiment, $\sigma \sim 23$ MeV, which is also crucial to differentiate between B^0 and B_s^0 decays ($\Delta m \sim 87$ MeV). Moreover, the large fraction of $B \to h^+h'^-$ decays is an important source of background due to hadrons being misidentified as muons in the region around the B^0 mass (this background is very small in the B_s^0 mass region).

Given their experimental detector resolution and trigger acceptance during Run 1 and Run 2, the CMS experiment with 61 fb^{-1} of data has similar sensitivity to the LHCb experiment with 4.4 fb^{-1} of data collected in the same period. Both experiments have provided a clear observation of the decay $B_s^0 \to \mu^+\mu^-$ (CMS and LHCb observe about 90 and 30 B_s^0 signal candidates with a background of about 40 and 10 events, respectively, within the invariant mass interval expected to contain 95% of the signal). Neither experiment has yet reached the sensitivity to observe the decay $B^0 \to \mu^+\mu^-$. The invariant mass distribution obtained by the LHCb experiment is shown in Fig. 25 and the LHCb [86] and CMS [87] results are $\mathcal{B}(B_s^0 \to \mu^+\mu^-) = (3.0 \pm 0.6^{+0.3}_{-0.2}) \times 10^{-9}$ and $\mathcal{B}(B_s^0 \to \mu^+\mu^-) = (2.9^{+0.7}_{-0.6} \pm 0.2) \times 10^{-9}$, respectively, while for the B^0 decay only limits can be quoted. The ATLAS collaboration has also published after a measurement [88] using 51 fb^{-1} of data, $\mathcal{B}(B_s^0 \to \mu^+\mu^-) = (2.8^{+0.8}_{-0.7}) \times 10^{-9}$ in agreement with the previous results.

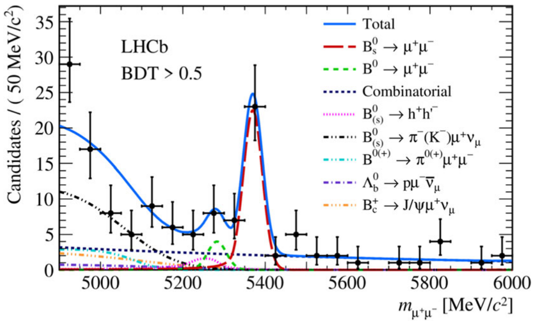

Fig. 25 Invariant mass distribution of dimuons selected from Ref. [86]. Superimposed on the data points in blue (solid line) is the combined fit, and its components as quoted in the insert

The $B_s^0 \to \mu^+\mu^-$ very rare decay has been searched for ever since the discovery of B mesons, around 40 years ago. Thanks to the ingenuity and persistence of the experimenters, it has been eventually measured at the LHC and found to be in agreement with the SM within current uncertainties, as shown in Fig. 26. Over the next decade, it will be extremely interesting to see how the measurement of $\mathcal{B}\,(B^0 \to \mu^+\mu^-)$ evolves, for which only upper limits are currently available.

4.2 $B^0 \to K^{*0}\mu^+\mu^-$

The language of effective field theory is used to parameterise NP contributions in terms of a sum of local four-fermion operators (Q_i) which depend only on SM fermions modulated by Wilson coefficients (C_i) which

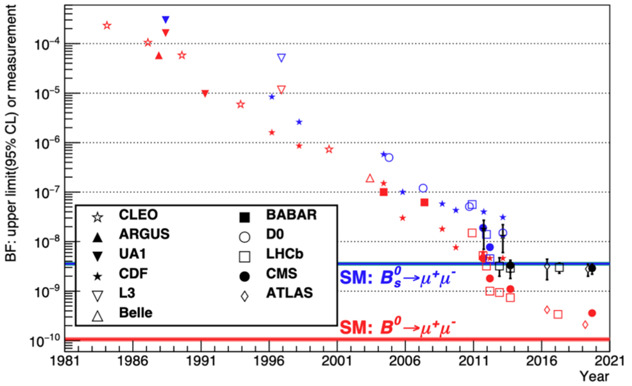

Fig. 26 Upper limits ($B^0 \to \mu^+\mu^-$) and eventual measurements of the $B_s^0 \to \mu^+\mu^-$ branching ratio by several experiments over the last 40 years

in turn depend on the heavy degrees of freedom, i.e. NP particles. The decay $B^0 \to K^{*0}\mu^+\mu^-$ is the so-called "golden mode" to test new vector (axial-vector) couplings, i.e. the C_9 and C_{10} Wilson coefficients contributing to the $b \to s$ transition. The $B^0 \to K^{*0}\mu^+\mu^-$ channel also complements the $b \to s\gamma$ decay which is mostly sensitive to NP dipole operators (i.e. C_7) and also the $B_s^0 \to \mu^+\mu^-$ decay which is mostly sensitive to NP (pseudo-) scalar operators (i.e. C_S and C_P). The charge of the pion in the decay $K^* \to K\pi$ defines the flavour of the B meson and an angular analysis can be performed unambiguously to test the helicity structure of the electroweak penguin.

The above system is completely defined by four variables: q^2, the square of the invariant mass of the dimuon system, θ_l, the angle between the positive lepton and the direction opposite to the B-meson in the dimuon rest frame, θ_K, the equivalent angle of the K^+ in the K^* rest frame and ϕ the angle between the two planes defined by (K, π) and (μ^+, μ^-) in the B-meson rest frame. The fourfold differential distribution contains a total of eleven angular terms that can be written in terms of seven q^2-dependent complex decay amplitudes. These amplitudes can be expressed in terms of five complex Wilson coefficients (C_S, C_P, C_7, C_9 and C_{10}), their five helicity counterparts and six form-factors, which play a role of nuisance parameters in the fit.

The LHCb experiment, with 3 fb^{-1} of data collected in Run 1, has triggered and selected about 2400 $B^0 \to K^{*0}\mu^+\mu^-$ candidates in the range $0.1 < q^2 < 19$ GeV^2 with signal over background $(S/B) > 5$. This is about one order of magnitude larger than the samples available at previous experiments (BaBar, Belle and CDF) and similar to the samples collected by ATLAS and CMS with ten times the luminosity, however with significantly worse S/B.

The statistics and the quality of the data accumulated by the LHCb experiment allow for a full angular analysis of $B^0 \to K^{*0}\mu^+\mu^-$ decays to be performed for the first time. The results [89] of this "tour de force" analysis mostly agree with SM predictions, however with some hints of disagreement for some specific distributions. In Fig. 27, two examples of the *CP*-averaged angular coefficients (i.e. the average of the coefficients measured with B^0 and $\overline{\text{B}}^0$ decays) are shown as a function of q^2. For these two examples, A_{FB} (modulating the $\sin^2\theta_K \times \cos\theta_l$ angular term) and S_5 (modulating the $\sin(2\theta_K) \times \sin\theta_l \times \cos\phi$ angular term) seem to agree less well with SM predictions. However, these are early days, and more data will be required (the Run 2 data analysis will be released soon). Also a careful reassessment of the SM uncertainties are needed before drawing definitive conclusions.

Several authors have already attempted to see if the overall pattern of the angular measurements is consistent with a given value of the relevant Wilson coefficients. As previously discussed, the inclusive $b \to s\gamma$ measurements strongly constrain non-SM values for C_7. The scalar C_S and pseudo-scalar C_P coefficients are constrained, for example, by the measurement of the branching fraction of the very rare decay $B_s^0 \to \mu^+\mu^-$. Therefore, the small disagreements observed in the angular analysis of the decay $B^0 \to K^{*0}\mu^+\mu^-$ and other decays seem to be consistent with a non-SM value of the C_9 Wilson coefficient, as can be seen in Fig. 28 taken from Ref. [90].

4.3 Lepton universality

In the SM, the electroweak couplings of leptons are flavour independent, or lepton "universal". However, this may not necessarily be the case for new particles beyond the SM. In particular, if the hints described in the previous section are an indication of new particles modifying the penguin diagram in Fig. 24, it is interesting to measure the ratios of branching fractions

Fig. 27 Two examples of the *CP*-averaged coefficients in the $B^0 \to K^{*0}\mu^+\mu^-$ angular terms as a function of q^2. The shaded boxes show the SM predictions taken from Ref. [91]

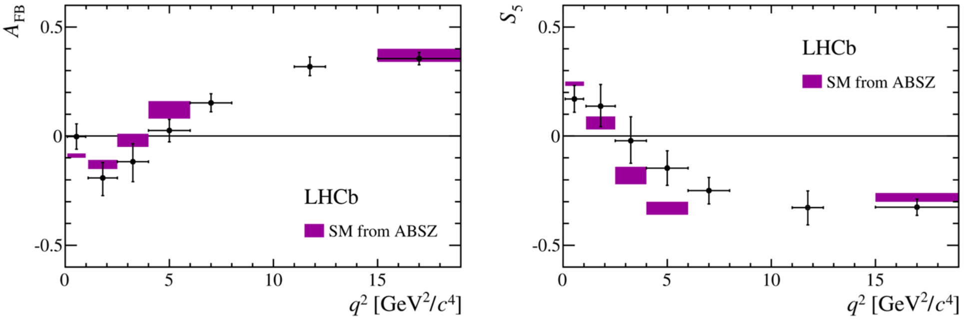

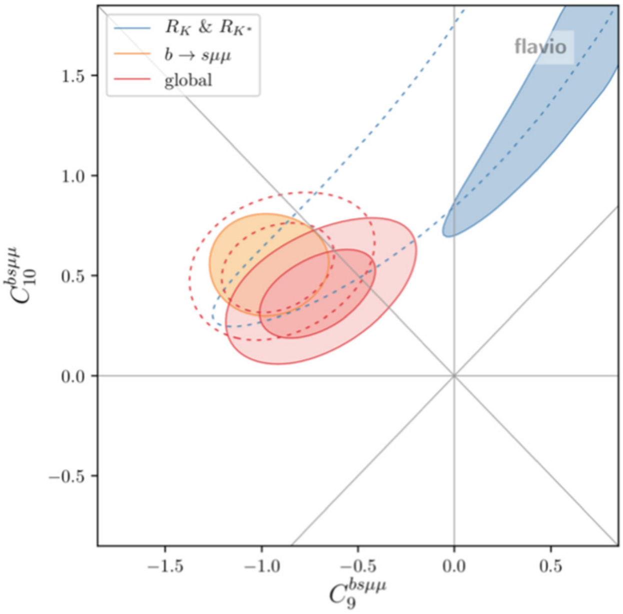

Fig. 28 Constrains on the contribution of NP to the real parts of C_9 and C_{10} at the 1σ and 2σ level taken from Ref. [90], corresponding to different measurements as indicated in the insert. The dotted lines correspond to the status before the latest updates for the 2019 physics winter conferences

in decays of different lepton families. For example, the ratios

$$R_X = \int \frac{d\Gamma(B^0 \to X\mu\mu)}{dq^2} dq^2 \bigg/ \int \frac{d\Gamma(B^0 \to Xee)}{dq^2} dq^2 \tag{4.1}$$

between B decays to final states with muons and electrons, where X is a hadron containing an s-quark or d-quark, are predicted to be very close to unity in the SM [92–94]. The uncertainties from QED corrections are found to be at the percentage level [95].

LHCb has measured the above ratio in several channels. Using Run 1 and part of Run 2 data (4.4 fb^{-1}), LHCb measures [96] $R_K = 0.846^{+0.060}_{-0.054}(\text{stat})^{+0.014}_{-0.016}(\text{syst})$ in the range $1.1 < q^2 < 6$ GeV^2, about 2.5σ below the SM prediction, and using only Run 1 data (3 fb^{-1}) LHCb measures [97] $R_{K^*} = 0.69^{+0.11}_{-0.07}(\text{stat}) \pm 0.05(\text{syst})$ in the same q^2 range, with a similar level of disagreement with the SM prediction. The latest R_K results from LHCb in bins of q^2 can be seen in Fig. 29, compared with previous results from the BaBar and Belle collaborations. The consistency between different experiments, and different channels, although with very different precision, has motivated many theoretical studies that relate these hints of lepton non-universality with the discrepancies described in the previous section. Figure 28 shows the status of the compatibility of both sets of measurements when assuming that only the $bs\mu\mu$ Wilson coefficients are modified (and $bsee$ coefficients are as predicted by the SM). While the initial results showed remarkable consistency between different sets of measurements as shown by the dotted lines in Fig. 28, the 2019 latest updates show a less clear picture. As of today, it is difficult to draw reliable conclusions, and more data is eagerly awaited.

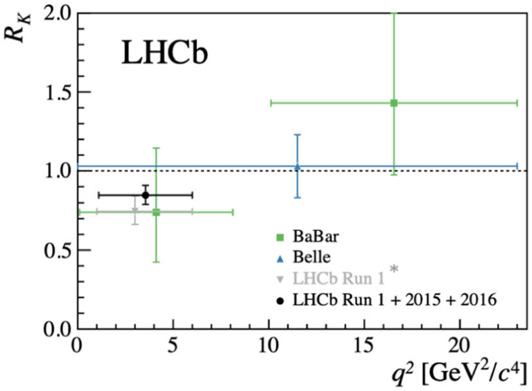

Fig. 29 Measurement of R_K as a function of the q^2 bins by different experiments

5 Spectroscopy

A deep understanding of quantum chromodynamics, the theory of strong interactions, is vital for precision tests of the Standard Model and in searches for new physics beyond. QCD is intensively tested in deep-inelastic-scattering processes and heavy vector boson production; however in the low-energy regime, there is a lack of precise QCD predictions. QCD, being a non-perturbative theory, does not calculate hadron properties, namely masses and decay widths from first principles. Alternative theoretical approaches are developed, such as heavy quark effective theory, heavy quark expansion or lattice calculations. These approaches require verification with experiment in various regimes, *e.g.* testing the agreement with data for hadrons with different quark content and quantum numbers. Spectroscopic measurements of hadron masses and widths or lifetimes provide a wide variety of tests for QCD models.

Huge production cross sections of charm and beauty in high-energy pp collisions in the forward region at LHCb [98–114], together with a good reconstruction efficiency, versatile trigger scheme and an excellent momentum and mass resolution, opens up exciting opportunities for spectroscopy measurements. The employment of LHCb's powerful hadron identification system [34,36,115] enables a substantial reduction in the combinatorial background specific to high-energy hadron-hadron collisions. The unique hadron identification is also especially important for spectroscopy measurements involving charged kaons and/or protons in the final state. The excellent momentum and vertex resolutions provided by the LHCb tracking system allows unprecedented precision on mass and width measurements: indeed the most precise measurements of mass for all open beauty particles and lifetimes of all open heavy flavour particles, currently result from the LHCb experiment [116]. Additional good control over the momentum scale and the detector alignment [117,118] also allows the natural widths of hadronic resonances to be probed with world-leading sub-MeV precision [119–125].

Almost 30 new hadrons have been discovered [126] using the Run 1&2 data-set, among them several open charm mesons and baryons, double-charm baryon, a charmonium state, several beauty mesons, fifteen beauty baryons and pentaquark-like $P_c(4312)^+$, $P_c(4400)^+$ and $P_c(4457)^+$ states. The quantum numbers of many hadrons, especially for charm mesons and charmonia-like exotic candidates, have been determined using amplitude analysis techniques. In the case of exotic particles such as pentaquark and tetraquark candidates, the determination of quantum numbers is vital for the understanding of their nature. Large statistics and low levels of background in decays of beauty hadrons with $J/\psi \to \mu^+\mu^-$ or $\psi(2S) \to \mu^+\mu^-$ final states allow the study of the spectroscopy of light unflavoured or strange hadrons [127–146]. Selected spectroscopy highlights are discussed in this chapter.

5.1 Charm hadrons

Two complementary methods for the study of spectroscopy of charm hadrons have been exploited in LHCb:

- the study of promptly produced charm hadrons,
- the study of charm particles produced in weak decays of beauty hadrons, *e.g.* from exclusive $B \to D^{(*)}\pi\pi$ decays.

The first technique allows the most efficient exploitation of the huge prompt $c\bar{c}$ production cross section in high-energy hadron collisions, but this is usually affected by a large background from light hadrons produced at the pp collision vertex. The second technique exploits a full amplitude analysis of the exclusive decays of beauty hadrons and therefore involves much lower statistics; however, the method often allows the determination of quantum numbers of the charm hadrons. The study of $D\pi$ final states enables a search for natural spin-parity resonances, ($P = (-1)^J$, labelled as D^*) while the study of $D^*\pi$ final states provides the possibility of studying both natural and unnatural spin-parity states, except for the $J^P = 0^+$ case, which is forbidden because of angular momentum and parity conservation. In inclusive $D^{(*)}\pi$ production, the production of any J^P state is permitted. An amplitude analysis of B decays allows a full spin-parity analysis of the charmed mesons present in the decay.

Both the above approaches are complementary and have resulted in discoveries of several new charm hadrons, among them the excited charm mesons. Many previous meson and baryon states, discovered earlier by other experiments, have been confirmed with high statistical significance, and their masses and widths have been measured with high precision. For many, the quantum numbers were either measured or constrained.

Excited charm mesons in the $D^{*+}\pi^-$, $D^+\pi^-$ and $D^0\pi^+$ *spectra* have been studied in LHCb using a 1 fb^{-1} data-set collected at $\sqrt{s} = 7\,\text{TeV}$ [147]. Four resonances labelled $D_0(2550)$, $D_J^*(2600)$, $D(2740)$ and $D_3^*(2750)$ have been observed. The $D_0(2550)$ and $D(2740)$ decay angular distributions are consistent with an unnatural spin-parity, while the $D_J^*(2600)$, and $D_3^*(2750)$ states are assigned natural parities. For the $D_0(2550)$, meson, angular distributions are consistent with a $J^P = 0^-$ assignment; however, for the other states, no definite assignment exists.

The excited charm mesons were also studied in B-decay amplitude analyses of $B^0 \to \overline{D}^0\pi^+\pi^-$ and $B^- \to D^+\pi^-\pi^+$ decays using the Run 1 data-set [148, 149] and $B^- \to D^{*+}\pi^-\pi^+$ [150] using a data-set corresponding to 4.7 fb^{-1}, collected at $\sqrt{s} = 7$, 8 and 13 TeV. The $D_3^*(2760)^0$ and $D_2^*(3000)^0$ states were observed for the first time [149], and the most precise determination of masses, widths and quantum numbers has been performed for the $D_0^*(2400)^-$, $D_2^*(2660)^-$, $D_3^*(2760)^-$ [148], $D_2^*(2660)^0$, $D_1^*(2680)^0$, $D_3^*(2760)^0$, $D_2^*(3000)^0$ [149] and for the $D_1(2420)^0$, $D_1(2430)^0$, $D_0(2550)^0$, $D_1^*(2600)^0$, $D_2(2740)^0$, $D_3^*(2750)^0$ [150] states.

Excited D_s^+ *mesons* were studied both in inclusive production in the $D^+K_S^0$ and D^0K^+ spectra using a data-set of 1 fb^{-1} collected at $\sqrt{s} = 7\,\text{TeV}$ [151], and through the amplitude analysis of $B_s^0 \to \overline{D}^0K^-\pi^+$ decays using Run 1 data [152]. It has been shown that the previously reported $D_{sJ}^*(2860)^+$ state [151,153,154] is an admixture of spin-1 and spin-3 resonances. The masses and width of new states, dubbed $D_{s1}^*(2860)^+$ and $D_{s3}^*(2860)^+$, are precisely measured, as well as the masses and widths of the $D_{s2}^*(2573)^+$ and $D_{s1}^*(2700)^+$ [151,152].

Excited Λ_c^+ *baryons* were studied in their decays to the D^0p final state via the amplitude analysis of Λ_b^0 baryon decays using an integrated luminosity sample of 3 fb^{-1} collected at $\sqrt{s} = 7$ and 8 TeV [155]. The analysis uses a sample of 11 212 ± 126 signal $\Lambda_b^0 \to D^0p\pi^-$ decays, where the D^0 mesons are reconstructed in the $K^-\pi^+$ final state. The amplitude fit is performed in the four-phase space regions in the Dalitz plot. For the near-threshold m_{D^0p} region, an enhancement in the D^0p amplitude is studied. The enhancement is consistent with being a resonant state, dubbed the $\Lambda_c(2860)^+$, with quantum numbers $J^P = \frac{3}{2}^+$ and with the parity measured relative to that of the $\Lambda_c(2880)^+$ state. The other quantum numbers are excluded with a significance greater than 6 standard

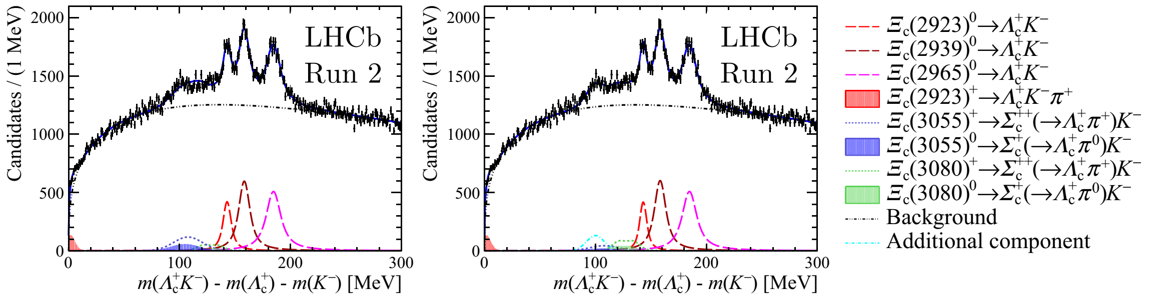

Fig. 30 Mass difference $\Delta m = m_{\Lambda_c^+ K^-} - m_{\Lambda_c^+} - m_{K^-}$ distributions [156]. Fits accounting for (left) three and (right) four excited Ξ_c^{*0} states are superimposed

deviations. The phase motion of the $\frac{3}{2}^+$ component with respect to the non-resonant amplitudes is obtained in a model-independent way and is consistent with resonant behaviour. The mass of the $\Lambda_c(2860)^+$ state is consistent with predictions for an orbital D-wave Λ_c^+-excitation with quantum numbers $\frac{3}{2}^+$, based on the nonrelativistic heavy quark-light diquark model and from QCD sum rules in the HQET framework. Also the fit allowed the most precise determination of the masses and widths of the known resonances $\Lambda_c(2880)^+$ and $\Lambda_c(2940)^+$, as well as constraining their quantum numbers.

Three excited Ξ_c^{*0} baryons have been observed in the $\Lambda_c^+ K^-$ mass spectrum using the Run 2 data-set [156]. The mass difference $\delta m \equiv m(\Lambda_c^+ K^-) - m(\Lambda_c^+) - m(K^-)$ spectrum for selected $\Lambda_c^+ K^-$ combinations is shown in Fig. 30. Three narrow structures, denoted $\Xi_c(2923)^0$, $\Xi_c(2939)^0$ and $\Xi_c(2965)^0$ are clearly visible with a significance exceeding 20σ for each signal. The data and fit show the least compatibility in the region $\delta m \approx 110\,\mathrm{MeV}$, that could be evidence for a fourth Ξ_c^{*0} state. Figure 30 (right) shows the δm distribution for the signal samples, where a structure in this region is added into the fit. A large improvement in the fit quality is achieved.

Five narrow excited Ω_c^* baryons have been observed in the $\Xi_c^+ K^-$ mass spectrum using the Run 1 data-set [157]. A large sample of Ξ_c^+ candidates were reconstructed in their Cabibbo-suppressed mode $\Xi_c^+ \to pK^-\pi^+$. In total around 1.05×10^6 $\Xi_c^+ \to pK^-\pi^+$ candidates with a purity of 83% were selected, as shown in Fig. 31 (left). The mass distribution for $\Xi_c^+ K^-$ combinations is shown in Fig. 31 (right), and five narrow peaks are clearly visible. The natural widths of the peaks are found to be between 0.8 and 8.7 MeV, and two of them, named $\Omega_c(3050)^0$ and $\Omega_c(3119)^0$, are found to be extremely narrow, with 95%CL limits of 1.2 and 2.8 MeV, respectively. It is found that the fit improves if an additional broad Breit–Wigner function is included in the 3188 MeV mass region. This broad structure may represent a single resonance, be the superposition of several resonances, be a feed-down from higher states, or some combination of the above. The interpretation of the narrow states is still an open question. The naive quark model expects five states in the region, but some have to be relatively broad. The molecular model predicts two states with $J^P = \frac{1}{2}^+$ and two with $J^P = \frac{1}{2}^+$, and three of the observed states are in remarkable agreement, both in mass and width, with this hypothesis [158].

5.2 Double-charm baryons

Three weakly decaying states with charm number $C = 2$ are expected in the quark model: one isospin doublet Ξ_{cc} and one isospin singlet Ω_{ccs}, each with spin-parity $J^P = \frac{1}{2}^+$. The properties of these baryons have been calculated with a variety of theoretical models. In most cases, the masses of the Ξ_{cc} states are predicted to lie in the range 3500 to 3700 MeV/c^2 [159]. The masses of the Ξ_{cc}^{++} and Ξ_{cc}^+ states are expected to differ by only a few MeV/c^2 due to approximate isospin symmetry. Most predictions for the lifetime of the Ξ_{cc}^+ baryon are in the range 50 to 250 fs, and the lifetime of the Ξ_{cc}^{++} baryon is expected to be three to four times longer at 200 to 700 fs, while both are expected to be produced at hadron colliders the longer lifetime of the Ξ_{cc}^{++} baryon should make it significantly easier to experimentally observe than the Ξ_{cc}^+ baryon.

Experimentally, there is a longstanding puzzle in the Ξ_{cc} system. Observations of the Ξ_{cc}^+ baryon in the $\Lambda_c^+ K^- \pi^+$ final state at a mass of 3519 ± 2 MeV/c^2 with signal yields of 15.9 events over 6.1 ± 0.5 events background (6.3σ significance), and 5.62 events over 1.38 ± 0.13 events background in the final state pD^+K^- (4.8σ significance), were reported by the SELEX collaboration [160,161]. The SELEX results included a number of unexpected features, notably a short lifetime and a large production rate relative to that of the singly charmed Λ_c^+ baryon. The lifetime was reported to be shorter than 33 fs at the 90% confidence level, and SELEX concluded that 20% of all Λ_c^+ baryons observed by the experiment originated from Ξ_{cc}^+ decays, implying a relative Ξ_{cc} production rate several orders of magnitude larger than theoretical expectations. Searches from the FOCUS [162], BaBar [163] and Belle [164] experiments did not find evidence for a state with the properties reported by

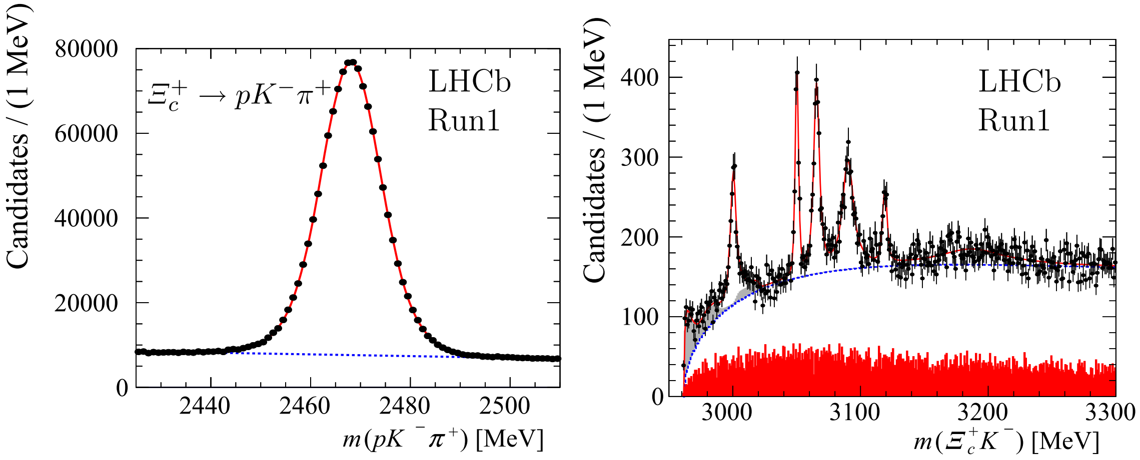

Fig. 31 (left) Distribution of the reconstructed invariant mass $m_{pK^-\pi^+}$ for all Ξ_c^+ candidates. The solid (red) curve shows the result of the fit, and the dashed (blue) line indicates the fitted background. (right) Distribution of the reconstructed invariant mass of $\Xi_c^+K^-$ combinations; the solid (red) curve shows the result of the fit, and the dashed (blue) line indicates the fitted background [157]. The shaded (red) histogram shows the corresponding mass spectrum from the Ξ_c^+ side-bands and the shaded (light grey) distributions indicate the feed-down from partially reconstructed $\Omega_c(X)^0$ resonances

the SELEX collaboration, and neither did a search at LHCb with data corresponding to an integrated luminosity of 0.65 fb^{-1} [165]. However, because the production environments at all the above experiments differ from that of SELEX, which studied collisions of a hyperon beam on fixed nuclear targets, these null results do not exclude the original observations.

LHCb has searched for the Ξ_{cc}^{++} decaying into $\Lambda_c^+K^-\pi^+\pi^+$ using a sample of pp collision data at 13 TeV, corresponding to an integrated luminosity of 1.7 fb^{-1}. A highly significant structure is observed in the mass spectrum, where the Λ_c^+ baryon is reconstructed into $pK^-\pi^+$, as shown in Fig. 32 (left). The structure is consistent with originating from a weakly decaying particle, identified as the doubly charmed baryon Ξ_{cc}^{++}. The observation of the state is confirmed using an additional sample of data collected at 8 TeV. Soon after, the observation was further confirmed by observing the same state in the decay $\Xi_{cc}^{++} \to \Xi_c^+\pi^+$, as shown in Fig. 32 (right). The mass of the Ξ_{cc}^{++} state was measured to be in very good agreement with the value measured in the $\Xi_{cc}^{++} \to \Lambda_c^+K^-\pi^+\pi^+$ decay channel [166]. The lifetime and mass of the Ξ_{cc}^{++} baryon were also precisely measured [167,168], where the lifetime favours smaller values in the range of the theoretical predictions.

5.3 Beauty hadrons

Excited B^+ and B^0 mesons have been investigated in the mass distributions of $B^+\pi^-$ and $B^0\pi^+$ combinations using a 3 fb^{-1} data sample at 7 and 8 TeV. The B^+ and B^0 candidates were reconstructed through the $B^+ \to \overline{D}^0\pi^+$, $B^+ \to \overline{D}^0\pi^+\pi^+\pi^-$, $B^+ \to J/\psi K^+$, $B^0 \to D^-\pi^+$, $B^0 \to D^-\pi^+\pi^+\pi^-$ and $B^0 \to J/\psi K^{*0}$ decay chains. Samples of about 1.2 million B^0 and 2.5 million B^+ candidates have been obtained with purity depending on decay mode, but always better than 80%. The $B^+\pi^-$ and $B^0\pi^+$ mass spectra with requirements that $p_{\mathrm{T}} > 2\,\mathrm{GeV}/c$ are shown in Fig. 33, where ten peaking structures are reconstructed. Out of these, six narrow low-mass structures correspond to the decays of the four $B_1(5721)^{0,+}$ and $B_2^*(5747)^{0,+}$ states observed by the CDF and D0 collaborations [170–172]: $B_1(5721) \to B^*\pi$ and $B_2(5747) \to B^{(*)}\pi$. The high statistics of LHCb had allowed the most precise measurements of the masses and widths of the $B_1(5721)^{0,+}$ and $B_2^*(5747)^{0,+}$ states to be made.

In addition to the six low-mass structures, four wider high-mass structures are observed, particularly prominent at high pion transverse momentum. These structures are consistent with the presence of four new excited B mesons, labeled $B_J(5840)^{0,+}$ and $B_J(5960)^{0,+}$, whose masses and widths are obtained under different hypotheses of their quantum numbers [173].

Orbitally excited B_s^0 mesons have been studied using only 1 fb^{-1} of data, collected at $\sqrt{s} = 7$ TeV. The B^+K^- mass spectra were investigated with the B^+ mesons being reconstructed in four decay modes. Previously, two narrow peaks had been observed in the B^+K^- mass distribution by the CDF and D0 collaborations [174, 175], named the $B_{s1}^*(5830)^0$ and $B_{s2}^*(5840)^0$. They are putatively identified as members of $j_q = \frac{3}{2}$ HQET doublet [176]. The two states are also visible in LHCb data, here as three narrow peaks shown in Fig. 34 (left), corresponding to the decays $B_{s1}(5830)^0 \to B^{*+}K^-$, $B_{s2}^*(5840)^0 \to B^{*+}K^-$, and $B_{s2}^*(5840)^0 \to B^+K^-$,

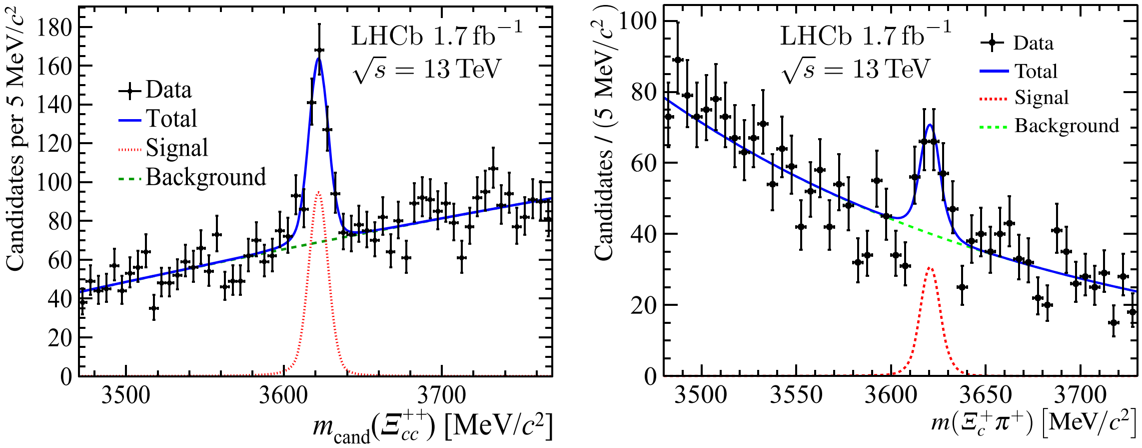

Fig. 32 (Left) Mass distribution of $\Lambda_c^+K^-\pi^+\pi^+$ candidates with fit projections overlaid [169]. (Right) Mass distribution of $\Xi_c^+\pi^+$ candidates [166]

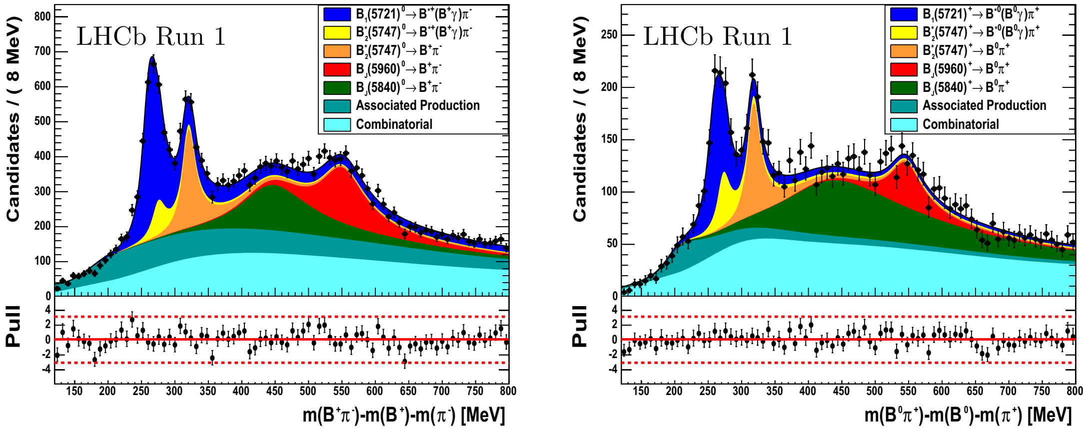

Fig. 33 Spectra of $\Delta m \equiv m_{B\pi} - m_B - m_\pi$ for (left) $B^+\pi^-$ and (right) $B^0\pi^+$ candidates with $p_{\rm T}(\pi) > 2\,{\rm GeV}/c$ [173]

where a soft photon from $B^{*+} \to B^+\gamma$ is undetected. This is the first observation of the $B_{s2}^*(5840)^0 \to B^{*+}K^-$ decay mode and a $J^P = 2^+$ assignment is favoured for this state. Large statistics, low background and LHCb's excellent mass resolution have allowed the first determination of the $B_{s2}^*(5840)^0$ width as well as the most precise mass measurements of both states. Due to the small energy release, the position and the shape of the peaks depends on the mass of the B^{*+} states, allowing the most precise determination of the $m_{B^{*+}}$ mass, as well as the mass difference $m_{B^{*+}} - m_{B^+}$.

Excited B_c^+ mesons have been searched for via their decays into the $B_c^+\pi^+\pi^-$ final state. A wide peak, interpreted as the $B_c(2S)^+$, was observed by the ATLAS collaboration using a sample of about 300 reconstructed $B_c^+ \to J/\psi\pi^+$ candidates [177], with a large relative production rate with respect to the base B_c^+ state. LHCb has searched for this state using 2 fb^{-1} of data collected at $\sqrt{s} = 8$ TeV, observing a sample of 3325 ± 73 reconstructed $B_c^+ \to J/\psi\pi^+$ decays. No signal is observed and an upper limit on the relative production rate has been obtained [178]. This upper limit is smaller than the relative production rate reported by ATLAS.

In 2018, the CMS collaboration, using a huge data set corresponding to 143 fb^{-1} collected at $\sqrt{s} = 13$ TeV and containing of 7629 ± 225 signal $B_c^+ \to J/\psi\pi^+$ decays, reported observation of a doublet of two narrow states, interpreted as spin-triplet $B_c(2S)^{*+}$ and spin-singlet $B_c(2S)^+$ states [179]. These observations were confirmed by LHCb using a 8.5 fb^{-1} data-set collected at $\sqrt{s} = 7, 8$ and 13 TeV [180], with 3785 ± 73 signal $B_c^+ \to J/\psi\pi^+$ decays. Two narrow peaks with a width compatible with the detector resolution are seen in the mass-difference $m_{B_c^+\pi^+\pi^-} - m_{B_c^+}$ spectrum, as shown in Fig. 34 (right). The local (global) significances of the two peaks are estimated to be 6.8σ (6.3σ) and 3.2σ (2.2σ) for the low-mass and high-mass states, respectively. The low-mass signal is interpreted as the spin-triplet state $B_c(2S)^{*+}$, decaying into $B_c^{*+}\pi^+\pi^-$ with the subsequent decay of the B_c^{*+} into $B_c^+\gamma$. The high-mass peak is attributed to the decay of the spin-singlet $B_c(2S)^+$ state into the $B_c^+\pi^+\pi^-$ final state.

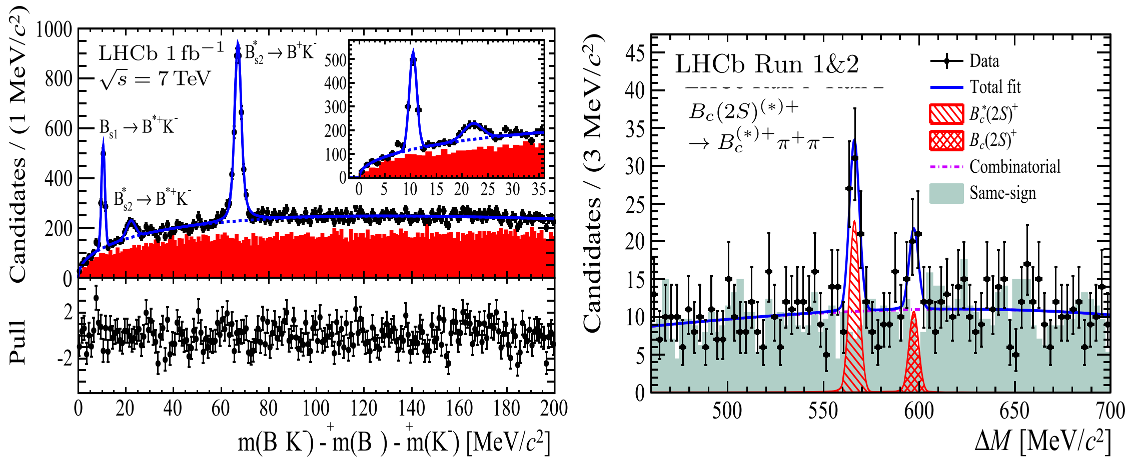

Fig. 34 (left) The mass difference distribution $m_{B^+K^-} - m_{B^+} - m_{K^-}$ in the B^+K^- mass spectra. The three peaks are identified as (left-to-right) $B_{s1}(5830)^0 \to B^{*+}K^-$, $B^*_{s2}(5840)^0 \to B^{*+}K^-$, and $B^*_{s2}(5840)^0 \to B^+K^-$. The total fit function is shown as a solid blue line, while the shaded red region is the spectrum of like-charge B^+K^+ combinations. The inset shows an expanded view of the $B_{s1}(5830)^0/B^*_{s2}(5840)^0 \to B^{*+}K^-$ region. (right) Distribution of $\Delta M \equiv m_{B_c^+\pi^+\pi^-} - m_{B_c^+}$ in the $B_c^+\pi^+\pi^-$ mass spectra with fit results overlaid. The same-sign distribution has been normalised to the data in the $B_c(2S)$ side band region

Excited Λ_b^0 *baryons* were discovered in the $\Lambda_b^0\pi^+\pi^-$ mass spectrum using only 1 fb^{-1} of LHCb data, accumulated at $\sqrt{s} = 7$ TeV in 2011 [119]. The Λ_b^0 candidates were reconstructed via $\Lambda_b^0 \to \Lambda_c^+\pi^-$ followed by $\Lambda_c^+ \to pK^-\pi^+$. In total $(70.54 \pm 0.33) \times 10^3$ signal Λ_b^0 decays were selected and then combined with $\pi^+\pi^-$ pairs. The $\Lambda_b^0\pi^+\pi^-$ spectrum in the region $5.90 \leq m_{\Lambda_b^0\pi^+\pi^+} \leq 5.95\,\text{GeV}/c^2$ is shown in Fig. 35 (left), where two narrow peaks, consistent with detector resolution, are visible. The significances of the observations are 5.2 and 10.2 standard deviations for the low-mass and high-mass peaks, respectively. The observed states are interpreted as the doublet of orbitally-excited $\Lambda_b(1P)^0$ states with quantum numbers $J^P = \frac{1}{2}^+$ and $\frac{3}{2}^+$. In 2020, the analysis was updated using the full Run 1 and 2 data-sets, as shown in Fig. 35 (right). The masses of these states are measured with unprecedented precision [123].

Using the full Run 1 and 2 data-sets, the mass spectrum of $\Lambda_b^0\pi^+\pi^+$ combinations, where $\Lambda_b^0 \to \Lambda_c^+\pi^-$ and $\Lambda_b^0 \to J/\psi pK^-$, was explored for higher masses of $\Lambda_b^0\pi^+\pi^-$ combinations. A significant broad structure is found at $m \approx 6.150\,\text{GeV}/c^2$ with a width around 10 MeV, as shown in Fig. 36 (left) [181]. The mass and width agree well when measured in the two decay modes $\Lambda_b^0 \to \Lambda_c^+\pi^-$ and $\Lambda_b^0 \to J/\psi pK^-$, where the significance exceeds 26 and 9 standards deviations, respectively. Since the mass of the new structure is above the $\Sigma_b^{(*)\pm}\pi^\mp$ kinematic thresholds, the $\Lambda_b^0\pi^+\pi^-$ mass spectrum is investigated in the $\Lambda_b^0\pi^\pm$ mass regions populated by the $\Sigma_b^{(*)\pm}$ resonances.

The data are split into three non-overlapping regions: candidates with a $\Lambda_b^0\pi^\pm$ mass within the natural width of the known $\Sigma_b^\pm$ mass, candidates with a $\Lambda_b^0\pi^\pm$ mass within the natural width of the known $\Sigma_b^{*\pm}$ mass and the remaining nonresonant (NR) region. The $\Lambda_b^0\pi^+\pi^-$ mass spectra in these three regions are shown in Fig. 36 (right). The spectra in the Σ_b and Σ_b^* regions look different and suggest the presence of two narrow peaks with very similar widths. The two-signal hypothesis is favoured over the single-signal hypothesis with a statistical significance exceeding seven standard deviations. The masses of the two states measured are consistent with predictions for the doublet of $\Lambda_b(1D)^0$ states with quantum numbers $J^P = \frac{3}{2}^+$ and $\frac{5}{2}^+$.

In 2020, the fifth excited Λ_b state was observed in the $\Lambda_b^0\pi^+\pi^-$ mass spectra, using the full LHCb Run 1 and 2 data-sets. Two decay modes of the Λ_b^0 baryon were used, $\Lambda_b^0 \to \Lambda_c^+\pi^-$ and $\Lambda_b^0 \to J/\psi pK^-$, and the significance of the new state, denoted Λ_b^{**0}, is in excess of 14 and 7 standard deviations in the two decay modes, respectively. This is shown in Fig. 37. Unlike the previously observed four narrow Λ_b states, $\Lambda_b(5912)^0$, $\Lambda_b(5920)^0$, $\Lambda_b(6146)^0$ and $\Lambda_b(6152)^0$, the new state is rather broad, $\Gamma = 72 \pm 11 \pm 2$ MeV. The measured mass and width agree with the interpretation of this state being the first radial excitation, the $\Lambda_b(2S)^0$ resonance [182]. This resonance is also consistent with a broad excess of events in the $\Lambda_b^0\pi^+\pi^-$ mass spectrum, previously reported by the CMS collaboration [183].

Excited $\Sigma_b^\pm$ *baryons* have been studied in the $\Lambda_b^0\pi^\pm$ mass spectra using the Run 1 LHCb data-set [184]. In total $(234.27 \pm 0.90) \times 10^3$ signal Λ_b^0 baryons were reconstructed in the decay mode $\Lambda_b^0 \to \Lambda_c^+\pi^-$. Distributions of the energy release in the decay, $Q \equiv m_{\Lambda_b^0\pi^\pm} - m_{\Lambda_b^0} - m_\pi$, are shown in Fig. 38. At low values of Q, there are previously-known signals from $\Sigma_b^{(*)\pm}$ states, observed

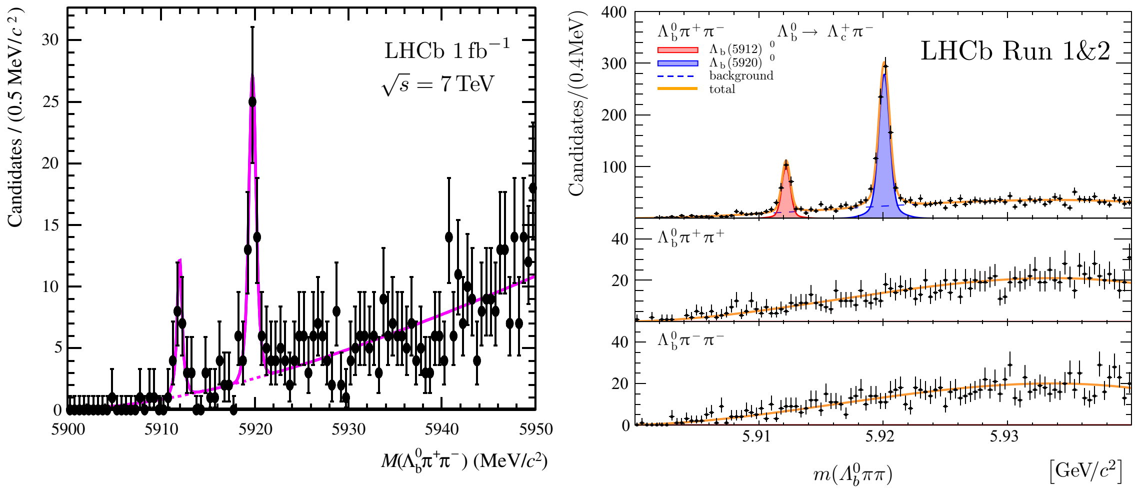

Fig. 35 (Left) Mass spectrum of $\Lambda_b^0\pi^+\pi^-$ combinations [119]. The points with error bars are the data, the solid line is the result of a fit, and the dashed line is the background contribution. (Right) Mass spectrum of (top) $\Lambda_b^0\pi^+\pi^-$, (middle) $\Lambda_b^0\pi^+\pi^+$ and (bottom) $\Lambda_b^0\pi^-\pi^-$ combinations in the full Run 1 and 2 datasets [123]

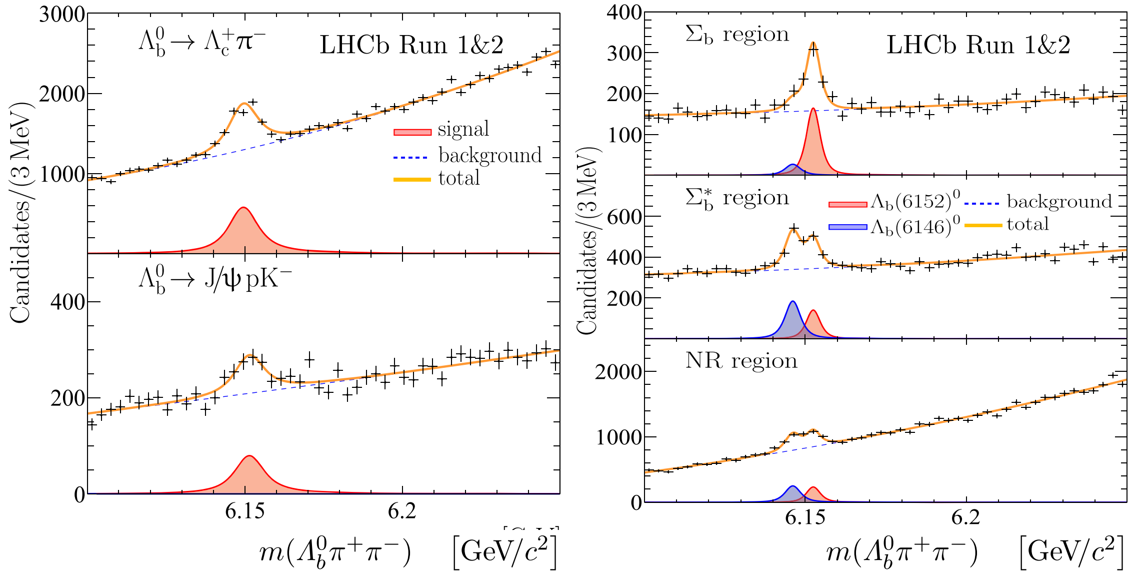

Fig. 36 (left) The mass distribution of selected $\Lambda_b^0\pi^+\pi^-$ candidates for (top) the $\Lambda_b^0 \to \Lambda_c^+\pi^-$ and (bottom) the $\Lambda_b^0 \to J/\psi pK^-$ decay modes. (right) Mass distributions of selected $\Lambda_b^0\pi^+\pi^-$ candidates for the three regions in $\Lambda_b^0\pi^\pm$ mass: (top) Σ_b, (middle) Σ_b^* and (bottom) the nonresonant (NR) region [181]

and characterised by the CDF collaboration [185,186]. New peaks in the $\Lambda_b^0\pi^-$ ($\Lambda_b^0\pi^+$) spectra are visible at $Q = 338.8 \pm 1.7\,\mathrm{MeV}$ ($336.6 \pm 1.7\,\mathrm{MeV}$), with a local significance of 12.7σ (12.6σ), based on the differences in log-likelihoods between the fits with zero signal and the nominal fit. In the heavy-quark limit, five $\Sigma_b(1P)$ states are expected, and several predictions of their masses have been made. Since the expected density of baryon states is high, it cannot be excluded that the new observed structures are the superposition of more than one (near-)degenerate state. Taking into account that the predicted mass and width depend on the as-yet-unknown spin and parity, the newly observed structures are compatible with being $\Sigma_b(1P)^\pm$ excitations. Other interpretations, such as molecular states, may also be possible.

$\Xi_b'^-$ and Ξ_b^{*-} baryons have been observed in the $\Xi_b^0\pi^-$ mass spectrum using the LHCb Run 1 dataset [120]. Signal Ξ_b^0 candidates were reconstructed in the final state $\Xi_c^+\pi^-$ with $\Xi_c \to pK^-\pi^+$. Two peaks are clearly visible in the $\delta m \equiv m_{\Xi_b^0\pi^-} - m_{\Xi_b^0} - m_{\pi^-}$ spectrum, as shown in Fig. 39 (left), a narrow state at $\delta m \approx 3.7\,\mathrm{MeV}/c^2$ and a broader state at

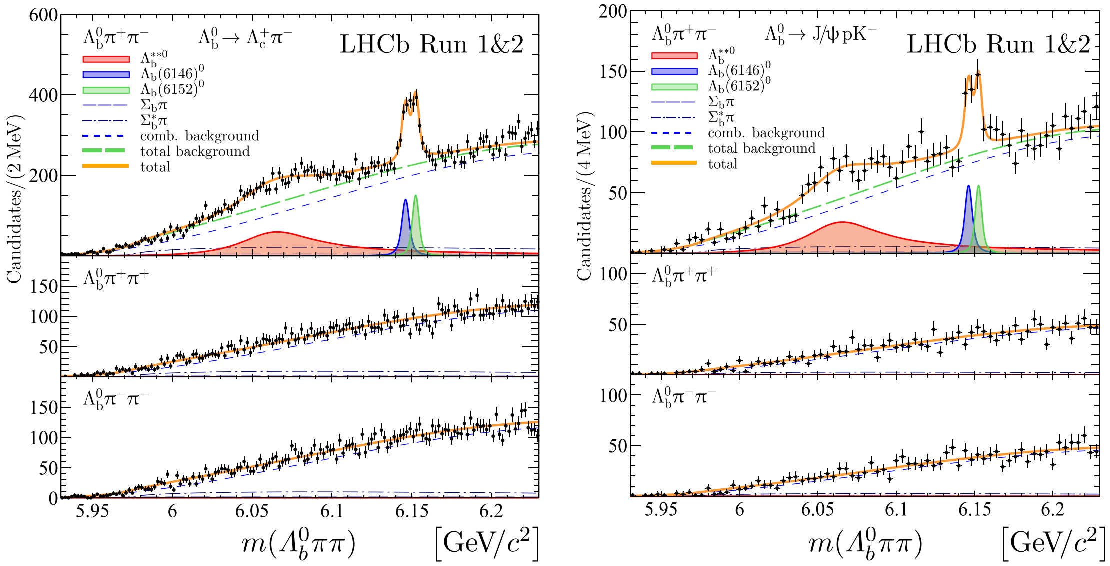

Fig. 37 Mass distribution of selected (top) $\Lambda_b^0\pi^+\pi^-$, (middle) $\Lambda_b^0\pi^+\pi^+$ and (bottom) $\Lambda_b^0\pi^-\pi^-$ candidates for the (left) $\Lambda_b^0 \to \Lambda_c^+\pi^-$ and (right) $\Lambda_b^0 \to J/\psi pK^-$ decay modes [123]

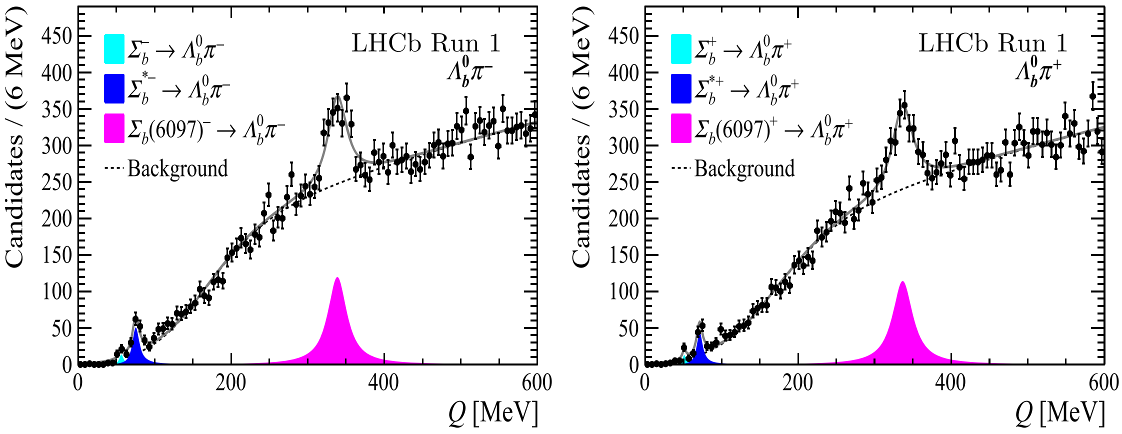

Fig. 38 The distributions of energy release $Q \equiv m_{\Lambda_b^0\pi^\pm} - m_{\Lambda_b^0} - m_\pi$ for selected $\Lambda_b^0\pi^\pm$ candidates [184]. The points show experimental data. The left (right) plot shows $\Lambda_b^0\pi^+$ ($\Lambda_b^0\pi^-$) combinations

$\delta m \approx 24\,\mathrm{MeV}/c^2$. No structure is observed in the wrong-sign sample, nor in the Ξ_b^0 mass side bands. The fitted natural width of the lower-mass state is found to be consistent with zero. The fitted yields of the lower and higher-mass peaks are 121 ± 12 and 237 ± 24 events, respectively, with statistical significance in excess of 10 standard deviations. The non-zero value of the natural width of the higher-mass state, $\Gamma = 1.65 \pm 0.31 \pm 0.10\,\mathrm{MeV}$ is significantly different from zero. The signals are interpreted as $\Xi_b'^-$ and Ξ_b^{*-} baryons.

The Ξ_b^{*0} *baryon* was first observed at CMS [187], and later studied in detail by the LHCb collaboration using the Run 1 data-set [121]. The Ξ_b^{*0} candidates have been reconstructed in the decay $\Xi_b^{*0} \to \Xi_b^-\pi^+$, with $\Xi_b^- \to \Xi_c^0\pi^+$ and $\Xi_c^0 \to pK^-K^-\pi^+$. The δm distribution, defined as $m_{\Xi_b^-\pi^+} - m_{\Xi_b^-} - m_{\pi^+}$, is shown in Fig. 39 (right). A narrow peak is clearly visible with a fitted signal yield of 232 ± 19 events. The non-zero value of the natural width of the peak, $\Gamma = 0.90 \pm 0.16\,\mathrm{MeV}$, is also highly significant; the change in log-likelihood when the width is fixed to zero exceeds 30 units. No other statistically significant structures are seen. The peak position and the width are consistent with, and about a factor of ten more precise than, the CMS measurements [187]. The measured width of the state is in line with theory expectations; a calculation based on lattice QCD predicts a width of $0.51 \pm 0.16\,\mathrm{MeV}$ [188], and another using the $^3P_0$ model obtains a value of 0.85 MeV [189]. The measured production ratio with respect to the Ξ_b^- state is measured to be $(28 \pm 3 \pm 1)\%$, suggesting that in high energy pp collisions at 7 and

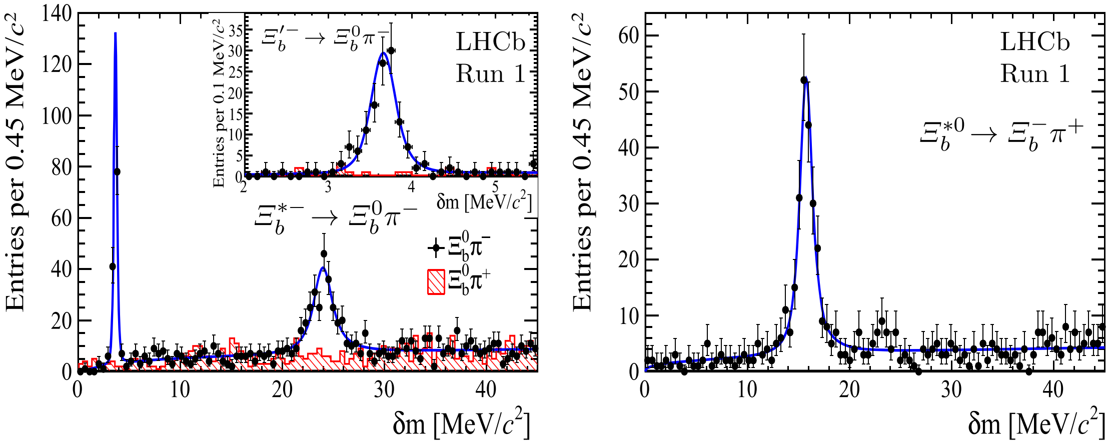

Fig. 39 (left) The distribution of the mass difference, $\delta m \equiv m_{\Xi_b^0\pi^-} - m_{\Xi_b^0} - m_{\pi^-}$, for $\Xi_b^0\pi^-$ candidates [120]. The points with error bars show right-sign candidates in the Ξ_b^0 mass signal region, and the hatched histogram shows wrong-sign candidates with the same selection. The curve shows the nominal fit to the right-sign candidates. Inset: detail of the region 2.0-5.5 MeV/c^2. (right) Distribution of δm and the fit for $\Xi_b^-\pi^+$ candidates [121]

8 TeV, a large fraction of Ξ_b^- baryons are produced through feed-down from higher-mass states.

A high-mass excited Ξ_b^- baryon has been observed in the $\Lambda_b^0 K^-$ and $\Xi_b^0\pi^-$ mass spectra, using a 3.5 fb^{-1} LHCb data-set at $\sqrt{s}$ = 7, 8 and 13 TeV [190]. The Λ_b^0 baryons were reconstructed via $\Lambda_b^0 \to \Lambda_c^+\pi^-$ and $\Lambda_b^0 \to \Lambda_c^+\mu^- X$, with the Ξ_b^0 decaying to $\Xi_b^0 \to \Xi_c^+\mu^- X$, with $\Lambda_c^+, \Xi_c \to pK^-\pi^+$. Full reconstruction of the Λ_b^0 baryon allows the excellent resolution of the $\Lambda_b^0 K^-$ mass spectra to be reached. In addition, partial reconstruction of Λ_b^0 and Ξ_b^0 baryons in their semileptonic modes allows a significant increase in the sample of Λ_b^0 and Ξ_b^0 baryons, where the missing neutrinos do not prevent a peaking structure in the spectra of mass differences $(m_{''\Lambda_b^0{}''K} - m_{''\Lambda_b^0{}''})$ and $(m_{''\Xi_b^0{}''\pi^-} - m_{''\Xi_b^0{}''})$. The resolution is improved by applying the 4-vector constraint $(p_{H_c^+} + p_{\mu^-} + p_{\text{miss}})^2 = m^2_{H_b^0}$, where H_c^+ stands for Λ_c^+ and Ξ_c^+ and H_b^0 stands for Λ_b^0 and Ξ_b^0.

The mass-difference spectra are shown in Fig. 40, where the peak locations for all three modes are seen to agree well. The statistical significances of the new excited baryon, dubbed the $\Xi_b(6227)^-$, are found to be 7.9σ for the $\Xi_b(6227)^- \to \Lambda_b^0 K^-$ followed by $\Lambda_b^0 \to \Lambda_c^+\pi^-$, 25$\sigma$ for the $\Xi_b(6227)^- \to \Lambda_b^0 K^-$ followed by $\Lambda_b^0 \to \Lambda_c^+\mu^- X$ and 7.2σ for the $\Xi_b(6227)^- \to \Xi_b^0\pi^-$ followed by $\Xi_b^0 \to \Xi_c^+\mu^- X$.

Four narrow excited Ω_b states have been observed in the $\Xi_b^0 K^-$ mass spectrum using the full Run 1 and 2 LHCb data-sets [191]. The Ξ_b^0 candidates were reconstructed in $\Xi_c^+\pi^-$ final states with $\Xi_c \to pK^-\pi^+$. After multivariate selection, a low-background sample of $(19.2 \pm 0.2) \times 10^3$ $\Xi_b^0 \to \Xi_c^+\pi^-$ decays has been obtained. The mass-difference spectrum $m(\Xi_b^0 K^-) - m(\Xi_b^0)$ for $\Xi_b^0 K^-$ combinations exhibits four narrow peaks, as shown in Fig. 41. The natural widths of the three lower mass states are consistent with zero, while the width of the high-mass state is found to be $1.4^{+1.0}_{-0.8} \pm 0.1$ MeV. The peaks have local significances that range from 3.6 to 7.2 standard deviations. After accounting for the look-elsewhere effect, the significances of the two low-mass peaks are reduced to 2.1σ and 2.6σ, respectively, while the two higher-mass peaks exceed 5σ. The observed $\Xi_b^0 K^-$ peaks seen here are similar to those observed in the $\Xi_c^+ K^-$ invariant mass spectrum [157]. Arguably, the simplest interpretation is that the peaks correspond to excited Ω_b^- states, in particular the $L = 1$ angular momentum excitation of the ground state, or possibly an $n = 2$ radial excitation.

Many of the quark-model calculations predict $L = 1$ states in this mass region, and at least some of the states should be narrow. In particular, using the ${}^3P_0$ model, five states in this mass region are predicted, with approximately 8 MeV mass splittings; the four lightest have partial widths, $\Gamma(\Xi_b^0 K^-)$, below 1 MeV, while the one with the largest mass has $\Gamma(\Xi_b^0 K^-)$ = 1.49 MeV. Conversely, predictions using the chiral quark model indicate that the $J^P = (3/2)^-$ and $(5/2)^-$ states are narrow, but the $(1/2)^-$ states are wide [192]. Quark-diquark models have also predicted several excited Ω_b^- states in the region around 6.3 GeV, with mass splittings similar to that observed here; however, there are no predictions for the decay widths. Molecular models have also been employed, where two narrow $J^P = (1/2)^-$ states are predicted at 6405 MeV and 6465 MeV [158], however do not match well with the LHCb measurements.

An alternate interpretation for one or more of the observed peaks is that they arise from the decay of a higher-mass excited Ω_b^{**-} state to $\Xi_b^{\prime 0}(\to \Xi_b^0\pi^0)K^-$, where the π^0 meson is undetected. If the mass of a not-

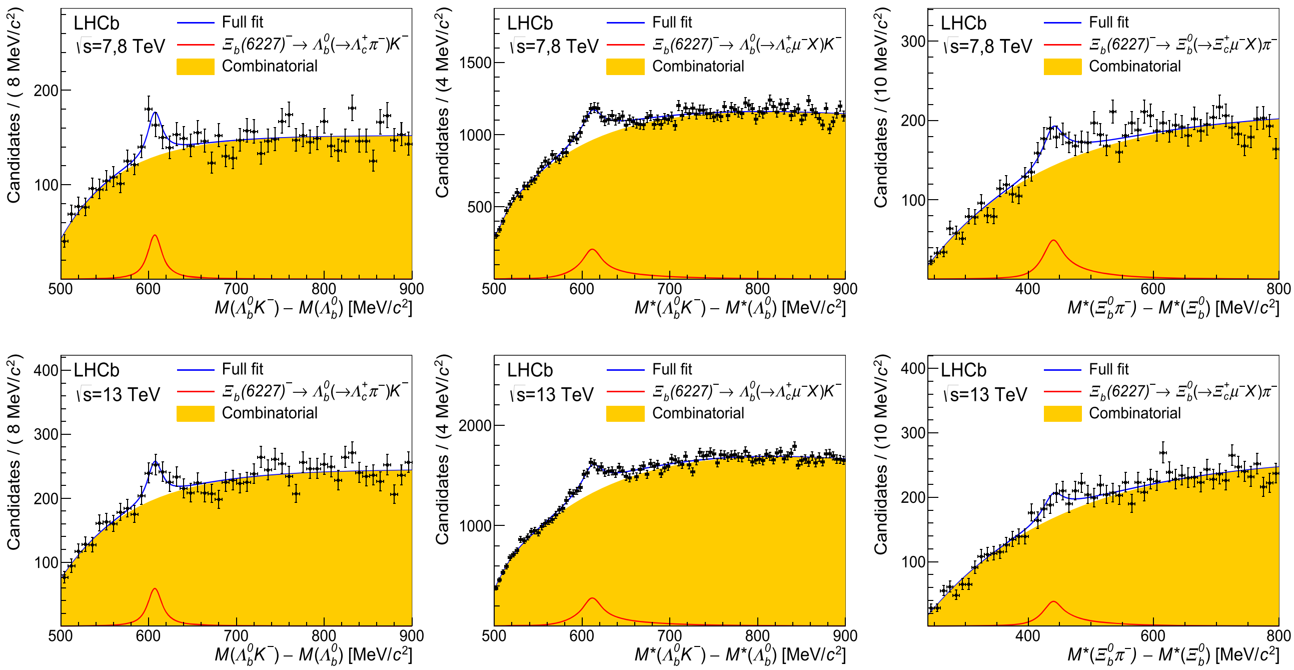

Fig. 40 Spectra of mass differences for Ξ_b^* candidates, reconstructed in the final states (left) $\Lambda_b^0 K^-$, with $\Lambda_b^0 \to \Lambda_c^+\pi^-$, (middle) $\Lambda_b^0 K^-$, with $\Lambda_b^0 \to \Lambda_c^+\mu^- X$, and (right) $\Xi_b^0\pi^-$, with $\Xi_b^0 \to \Xi_c^+\mu^- X$, along with fits to the data [190]. The top row is for 7 and 8 TeV data and the bottom is for 13 TeV. The symbol M^* represents the mass after the 4-vector constraint $(p_{H_c^+} + p_{\mu^-} + p_{\mathrm{miss}})^2 = m^2_{H_b^0}$ is applied

yet-observed $\Xi_b'^0$ state is in the region $m_{\Xi_b^0} + m_{\pi^0} < m_{\Xi_b'^0} < m_{\Xi_b'^-}$, each of the observed narrow peaks can be interpreted as having come from the above decay, provided that the corresponding excited Ω_b^{**-} state is narrow, $\Gamma_{\Omega_b^{**-}} \le 1\,\mathrm{MeV}$. In this case, their masses can be evaluated as $m_{\Omega_b^{**-}} = m_{\Xi_b'^0} + \delta m_{\mathrm{peak}}$, where δm_{peak} is a measured position of the peak in the $m(\Xi_b^0 K^-) - m(\Xi_b^0)$ spectrum.

5.4 Conventional charmonia and bottomonia

Charmonium states in $D\bar{D}$ mass spectra near threshold have been studied using the full LHCb statistical sample collected in Runs 1 and 2 [193]. D^0 and D^+ candidates were reconstructed in the $D^0 \to K^-\pi^+$ and $D^+ \to K^-\pi^+\pi^+$ decay modes. In total, 3.6×10^6 D^0D^0 and 2.0×10^6 D^+D^- pairs have been selected. The mass spectra for $D^0\overline{D}^0$ and D^+D^- combinations are shown in Fig. 42 (left), with the zoomed-in region between $3.80 \le m_{D\overline{D}} \le 3.88\,\mathrm{GeV}/c^2$ presented in Fig. 42 (right).

Four peaking structures are observed in the spectra. Two of the peaks correspond to the known $\psi(3770)$ and $\chi_{c2}(3930)$ charmonium states. A narrow peak close to threshold represents partially reconstructed $\chi_{c1}(3872) \to D^{*0}\overline{D}^0$ decays, subsequently with $D^{*0} \to D^0\gamma$ or $D^{*0} \to D^0\pi^0$ with the γ or π^0 meson missing. The narrow peak with mass around 3840 MeV/c^2 is identified as a new charmonium state. Its mass value and small natural width suggest an interpretation as the $\psi_3(1^3D_3)$ charmonium state with quantum numbers $J^{PC} = 3^{--}$ [194]. In addition, prompt hadroproduction of the $\chi_{c2}(3930)$ and $\psi(3770)$ charmonium states have been observed for the first time, and precise measurements of their resonance parameters have been performed.

Observation of the decays $\chi_c \to J/\psi\mu^+\mu^-$ using a $4.9\,\mathrm{fb}^{-1}$ data-set collected at $\sqrt{s} = 7$, 8 and 13 TeV enabled the most precise direct determination of the masses of the χ_{c1} and χ_{c2} states and the width of the χ_{c2} to be performed with unprecedented precision [122]. The observation of these decay modes provides opportunity for the precise measurements of the $\chi_{c1,c2}$ production and polarisation, that in turn is vital for tests of QCD models of charmonia production.

Observation of $\psi_2(3823) \to J/\psi\pi^+\pi^-$ in $B^+ \to (\psi_2(3823) \to J/\psi\pi^+\pi^-)K^+$ decays using the full LHCb Run 1 and 2 data-sets, has allowed the most precise determination of the mass of the tensor $\psi_2(3823)$ state and the best constrained upper limit of its width [125]. The observed mass distribution is shown in Fig. 43. Within the factorization approach, the branching fraction for the decay $B^+ \to \psi_2(3823)K^+$ vanishes, and a non-zero value for this branching fraction allows

Fig. 41 The mass difference $\delta m \equiv m(\Xi_b^0 K^-) - m(\Xi_b^0)$ for selected $\Xi_b^0 K^-$ candidates [191]

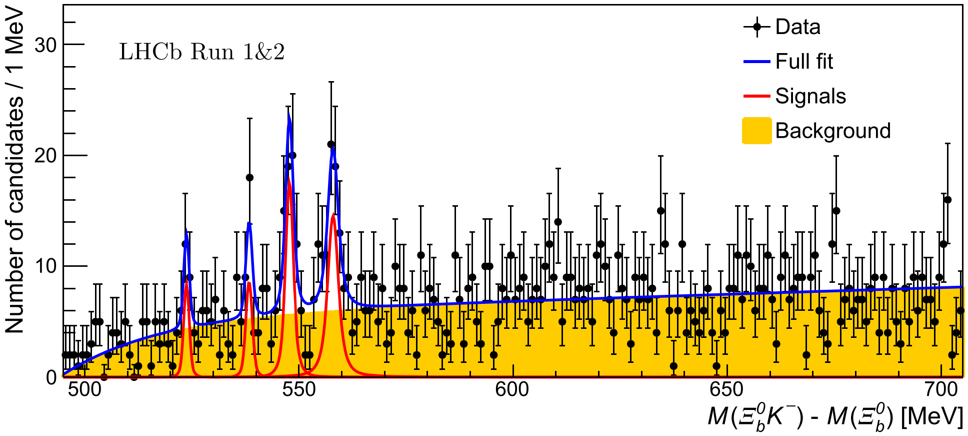

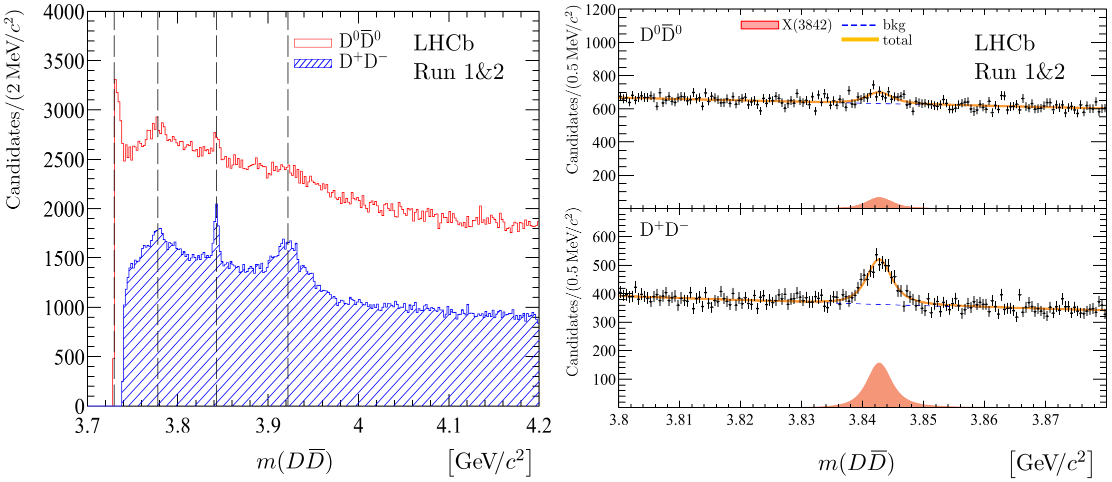

Fig. 42 (left) The $D\bar{D}$ mass spectra. The open (red) histogram shows $D^0\bar{D}^0$ combinations while the dashed (blue) histogram shows D^+D^-. (right) The mass spectra of (top) $D^0\bar{D}^0$ and (bottom) D^+D^- combinations in the narrow mass region $3.80 \leq m_{D\bar{D}} \leq 3.88\,\mathrm{GeV}/c^2$, with fits superimposed. Different components employed in the fit are indicated in the legend

an evaluation of the contribution of the $D_s^{(*)+}\bar{D}^{(*)0}$ rescattering amplitudes in the $B^+ \to c\bar{c}K^+$ decays.

5.5 Pentaquarks

The LHCb collaboration studied $\Lambda_b^0 \to J/\psi pK^-$ decays using the Run 1 data-set [195]. In total $(26.0\pm0.2)\times10^3$ signal Λ_b^0 candidates were selected, and an anomalous peak in the $J/\psi p$ mass spectrum is observed, as shown in Fig. 44 (left). If the peak structure represents a resonance which strongly decays into $J/\psi p$, the minimal valence quarks would be $c\bar{c}uub$, a charmonium pentaquark state. A full six-dimensional amplitude fit with resonance invariant masses, three helicity angles and two differences between decay planes has been applied to describe the data. The amplitude model in the fit contains 14 well-defined Λ^* states and two pentaquark states, labelled as $P_c(4380)^+$ and $P_c(4450)^+$. The projections of the fit are shown in Fig. 44. The masses and widths of the wide $P_c(4380)^+$ and narrow $P_c(4450)^+$ states have been measured. The preferred spin-parity assignments are $\left(\frac{3}{2}^-, \frac{5}{2}^+\right)$, $\left(\frac{3}{2}^+, \frac{5}{2}^-\right)$ and $\left(\frac{5}{2}^+, \frac{3}{2}^-\right)$, where the first value is the J^P assignment given by the best fit.

Following the first observation, the exotic hadronic character of the $J/\psi p$ structure around $4450\,\mathrm{MeV}/c^2$ was confirmed in a model-independent way [143]. This analysis gave similar results and excluded that the data could be described by the pK^- constributions alone. Further confirmation comes from the amplitude analysis of the Cabibbo-suppressed decay $\Lambda_b^0 \to J/\psi p\pi^-$ [196], where 1885 ± 50 signal candidates were investigated. There are different theoretical interpretations suggested, including a tightly bound $duuc\bar{c}$ state a loosely bound molecular baryon–meson state or a triangle-diagram processes.

A partial update of the above analysis was made using the full Run 1&2 data sample [197]. A ninefold increase in statistics is achieved due to the larger data sample, an improved selection criteria, and increased $pp \to b\bar{b}$ cross section at $\sqrt{s} = 13$ TeV in Run 2. For

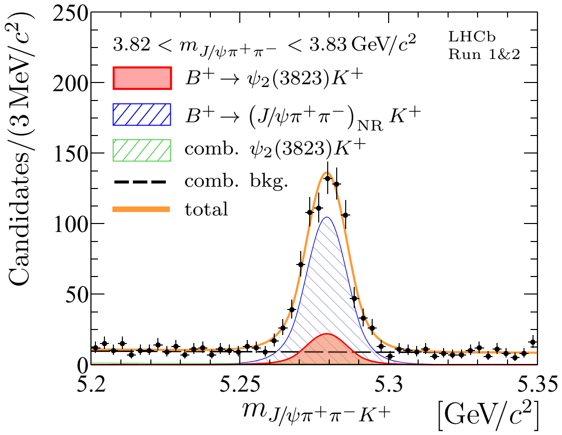

Fig. 43 Distributions of the (left) $J/\psi\pi^+\pi^-K^+$ and (right) $J/\psi\pi^+\pi^-$ mass for selected $B^+ \to \left(\psi_2(3823) \to J/\psi\pi^+\pi^-\right) K^+$ candidates [125]

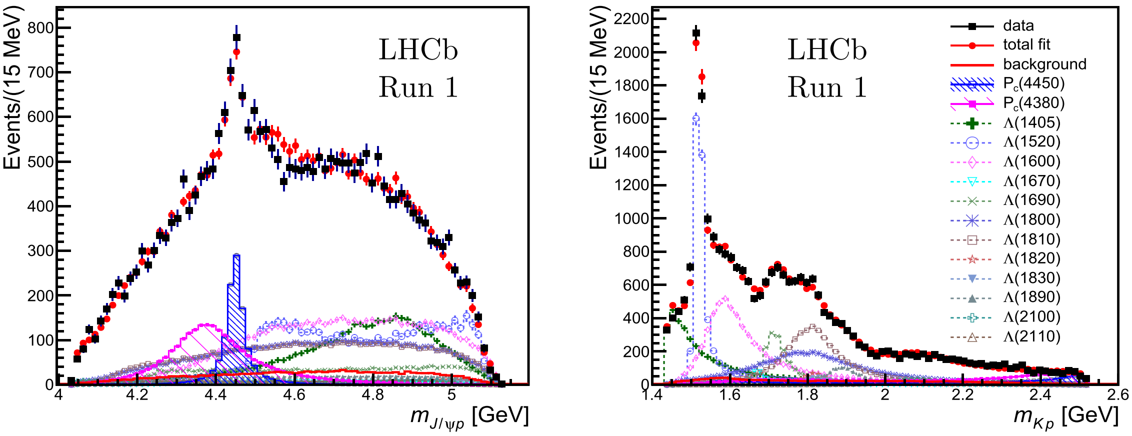

Fig. 44 The (left) $m_{J/\psi p}$ and (right) m_{Kp} mass distributions, showing superimposed fit projections as solid (red) points. The solid (red) histogram shows the background distribution, the blue shaded histogram represents the $P_c(4450)^+$ state, and the shaded purple histogram represents the $P_c(4380)^+$. Each Λ^* component is also shown

candidates with a mass consistent with the nominal Λ_b^0 baryon mass, the $J/\psi p$ and pK^- mass spectra were investigated. In the distribution of $J/\psi p$ mass, the previously reported peaking structure around 4450 MeV/c^2 was confirmed, and a new narrow peak with mass around 4312 MeV/c^2 was found. The $\Lambda^* \to pK^-$ contributions are clearly seen in the Dalitz plot, as shown in Fig. 45 (left).

Since the newly observed peaks are narrow, the full amplitude analysis faces computational challenges. This is because resolution effects should be included in the formalism which complicates the fitting procedure. Conversely, narrow peaks cannot be due to reflections from Λ^* states, motivating the validity of the one-dimensional fit approach to study the $J/\psi p$ invariant mass. The $J/\psi p$ mass in the narrow-resonance region together with the result of the fit is shown in Fig. 45 (right). The previously reported peak around the 4450 MeV/c^2 mass is now resolved into a two-peak structure of $P_c(4440)^+$ and $P_c(4457)^+$ states. In total, three narrow pentaquark states are observed. The statistical significance of the two-peak interpretation of the previously-reported single $P_c(4450)^+$ structure is 5.4σ. The statistical significance of a new $P_c(4312)^+$ state is 7.3σ. The masses and widths of the pentaquark candidates are measured. Taking into account systematic uncertainties, the widths are consistent with the mass resolution. Hence, upper limits on the natural widths at the 95 % confidence level (CL) are obtained.

In summary, while the existence of pentaquark-like resonances is certainly beyond doubt, their exact nature is still unclear. They can be genuine five-quark bound states, or *e.g.* near-threshold meson-baryon molecules. More studies are required to clarify this.

5.6 Charmonium-like exotic states

The enigmatic $X(3872)$ *particle* was discovered in B^+ decays by the Belle bollaboration [198]. Subsequently, its existence has been confirmed by several other experiments [199–201]. The nature of this state is rather

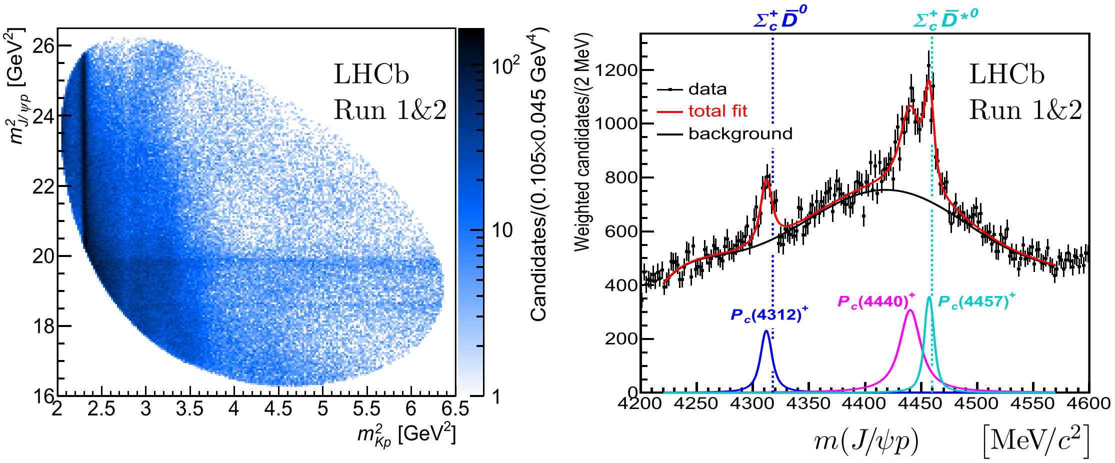

Fig. 45 (left) Dalitz plot of $\Lambda_b^0 \rightarrow J/\psi p K^-$ candidates. The vertical bands correspond to Λ^* resonances. The horizontal bands correspond to the $P_c(4312)^+$, $P_c(4440)^+$ and $P_c(4457)^+$ structures at $m^2_{J/\psi p} = 18.6$, 19.7 and 19.9 GeV^2, respectively. (right) Projection of the Λ^*-suppressed $m_{J/\psi p}$ distribution showing a fit with three Breit−Wigner amplitudes and a sixth-order polynomial background. The mass thresholds for the $\Sigma_c \bar{D}^0$ and $\Sigma_c \bar{D}^{*0}$ final states are superimposed

unclear. Among the open possibilities are conventional charmonium and exotic states such as $D^{*0}\bar{D}^0$ molecules [202], tetra-quarks [203] or their mixtures [204]. Determination of the J^{PC} quantum numbers is important to shed light on this ambiguity. The C-parity of the state is positive since the $X(3872) \rightarrow J/\psi\gamma$ decay has been observed [205,206]. The CDF experiment analysed three-dimensional angular correlations in a relatively high-background sample of 2292 ± 113 inclusively reconstructed $X(3872) \rightarrow J/\psi\pi^+\pi^-$, $J/\psi \rightarrow \mu^+\mu^-$ decays, dominated by prompt production in $p\bar{p}$ collisions. The unknown polarisation of the $X(3872)$ limits the sensitivity of the measurement of J^{PC} [207]. A χ^2 fit of J^{PC} hypotheses to the binned three-dimensional distribution of the J/ψ and $\pi^+\pi^-$ helicity angles and the angle between their decay planes [208–210] excluded all spin-parity assignments except for 1^{++} and 2^{-+}.

Using $\sqrt{s} = 7$ TeV pp collision data corresponding to 1 fb^{-1} collected in 2011, the LHCb collaboration performed the first analysis of the complete five-dimensional angular correlations of the $B^+ \rightarrow X(3872)K^+$, $X(3872) \rightarrow J/\psi\pi^+\pi^-$, $J/\psi \rightarrow \mu^+\mu^-$ decay chain [211]. About 38 000 candidates passed the multivariate selection in a $\pm 2\sigma$ range around the B^+ $m_{J/\psi\pi^+\pi^-K^-}$ mass distribution, with a signal purity of 89%. The $\Delta m \equiv m_{J/\psi\pi^+\pi^-} - m_{J/\psi}$ distribution is shown in Fig. 46 (left). The fit yields 5642 ± 76 and 313 ± 26 candidates for $\psi(2S) \rightarrow J/\psi\pi^+\pi^-$ and $X(3872) \rightarrow J/\psi\pi^+\pi^-$ signals, respectively.

The angular correlations in the B^+ decay carry information about the $X(3872)$ quantum numbers. To discriminate between the 1^{++} and 2^{-+} assignments, a likelihood-ratio test is used. A test statistic t is defined as $-2\ln[\mathcal{L}(2^{-+})/\mathcal{L}(1^{++})]$. Positive (negative) values of the test statistic for the data, t_{data}, favour the 1^{++} (2^{-+}) hypothesis. The value of the test statistic observed in the data is $t_{\text{data}} = +99$, thus favouring the 1^{++} hypothesis. A rejection of the 2^{-+} hypothesis with greater than 5σ significance is demonstrated using a large sample of pseudo-experiments. As shown in Fig. 46 (right), the distribution of t is reasonably well approximated by a Gaussian function. Based on the mean and r.m.s. spread of the t distribution for the 2^{-+} experiments, this hypothesis is rejected with a significance of 8.4σ. Hence, the obtained results correspond to an unambiguous assignment of the $X(3872)$ state to be 1^{++}.

The above result rules out the explanation of the $X(3872)$ as a conventional $\eta_{c2}(1^1D_2)$ state. Among the remaining possibilities are the $\chi_{c1}(2^3P_1)$ charmonium state, and unconventional explanations such as a $D^{*0}\bar{D}^0$ molecule tetraquark state charmonium–molecule mixture.

With a larger 3 fb^{-1} data-set at $\sqrt{s} = 7$ and 8 TeV, the analysis has been repeated in the decay $X(3872) \rightarrow J/\psi\rho^0$ without an assumption on the orbital angular momentum [212]. The analysis confirmed the $J^{PC} = 1^{++}$ assignment for the $X(3872)$ state and also set an upper limit of 4% at 90% C.L. on the D-wave contribution.

A precise determination of the mass and width of the $X(3872)$ state was performed using two minimally overlapping data-sets. The first was the 3 fb^{-1} Run 1 data-set in which the $X(3872)$ particles were now selected from decays of hadrons containing b quarks [124]. The second was the full Run 1 and 2 data-sets using a sample of $(547.8 \pm 0.8) \times 10^3$ $B^+ \rightarrow J/\psi\pi^+\pi^-K^+$ decays [125]. In both cases, the $X(3872)$ was reconstructed in the $X(3872) \rightarrow J/\psi\pi^+\pi^-$ final state. The mass and width were determined from a fit to the $J/\psi\pi^+\pi^-$ mass distribution assuming a Breit–Wigner line shape for

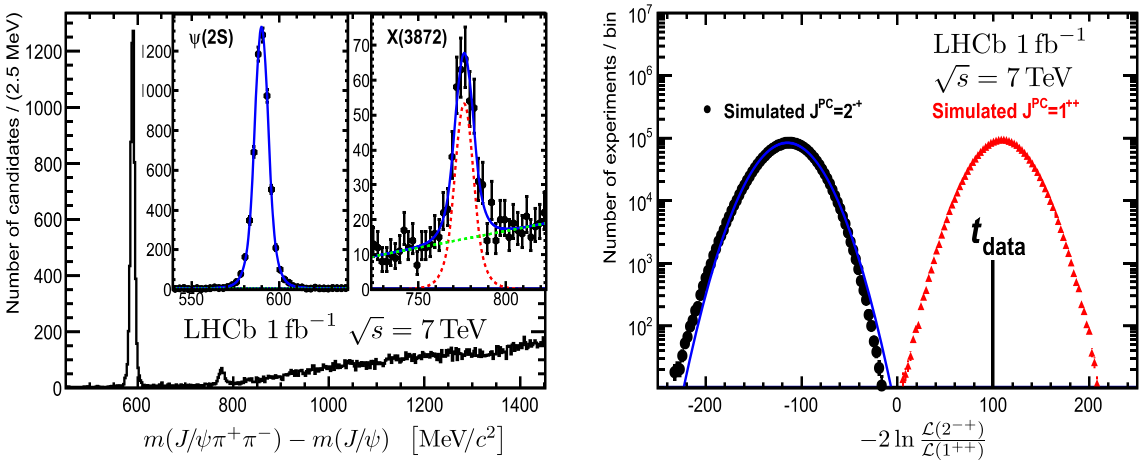

Fig. 46 (left) Distribution of $\Delta m \equiv m(J/\psi\pi^+\pi^-) - m(J/\psi)$ for $B^+ \to J/\psi\pi^+\pi^-K^-$ candidates. The fits of the $\psi(2S)$ and $X(3872)$ signals are displayed. The solid blue, dashed red and dotted green lines represent the total fit, signal component and background component, respectively. (right) Distribution of the test statistic $t \equiv -2\ln\frac{\mathcal{L}(2^{-+})}{\mathcal{L}(1^{++})}$ for the simulated experiments with $J^{PC} = 2^{-+}$ (black circles on the left) and with $J^{PC} = 1^{++}$ (red triangles on the right). The value of the test statistic for the data, t_{data}, is shown by the solid vertical line

the $X(3872)$ state, measured as follows:

$$\begin{aligned} \mathrm{m}_{X(3872)} &= 3871.70 \pm 0.07 \pm 0.07\,\mathrm{MeV}/c^2\,, \\ \Gamma_{\mathrm{BW}} &= 1.39 \pm 0.24 \pm 0.10\,\mathrm{MeV}\,, \\ \mathrm{m}_{X(3872)} &= 3871.60 \pm 0.06 \pm 0.03\,\mathrm{MeV}/c^2\,, \\ \Gamma_{\mathrm{BW}} &= 0.96^{+0.19}_{-0.18} \pm 0.21\,\mathrm{MeV}\,, \end{aligned}$$

where the first and the second lines correspond to Refs. [124] and [125], respectively. The above measurements represent the most precise determination of the mass of the $X(3872)$ state and the first measurements of its width. The measured mass corresponds to the binding energy δE, defined as $m_{D^0}c^2 + m_{D^{*0}}c^2 - m_{X(3872)}c^2$, which is 70 ± 120 keV.

While the proximity of the measured mass of the $X(3872)$ to the $D^0\overline{D}^{*0}$ threshold [213–217] favours the interpretation of this state as a $D^0\overline{D}^{*0}$ molecule, the large production cross section of the $X(3872)$ [199,200,215,218,219] disfavours this. The pure molecular interpretation is further disfavoured by the observation of the decay $X(3872) \to \psi(2S)\gamma$. The ratio of the decay rates to $\psi(2S)\gamma$ and $J/\psi\gamma$ final states is very sensitive to the nature of the $X(3872)$ state. This is predicted to be in the range $(3-4)\times 10^{-3}$ for a $D\overline{D}^*$ molecule $1.2 - 15$ for a pure charmonium state and $0.5 - 5$ for a molecule–charmonium mixture.

LHCb performed the search for $X(3872) \to \psi(2S)\gamma$ decays using the decay chain $B^+ \to X(3872)K^+$, $X(3872) \to \psi(2S)\gamma$. The analysis was based on a 1 fb^{-1} data sample at 7 TeV and 2 fb^{-1} at 8 TeV. The significance of the $B^+ \to (X(3872) \to \psi(2S)\gamma)\,K^+$ signal is 4.4 standard deviations. The branching fraction, normalised to that of the $X(3842) \to J/\psi\gamma$ decay mode, is measured to be

$$\frac{\mathcal{B}(X(3842) \to \psi(2S)\gamma)}{\mathcal{B}(X(3842) \to J/\psi\gamma)} = 2.46 \pm 0.64 \pm 0.29.$$

This result is compatible with, but more precise than, previous measurements [206,220], and strongly disfavours a pure molecular interpretation of the $X(3872)$ state.

Structures in the $J/\psi\phi$ system have acquired great experimental and theoretical interest since the CDF collaboration reported 3.8σ evidence $(14 \pm 5$ events) for a narrow $(\Gamma = 11.7^{+8.3}_{-5.0} \pm 3.7\,\mathrm{MeV})$ near-threshold $X(4140)$ mass peak in a sample of 75 ± 11 reconstructed $B^+ \to J/\psi\phi K^+$ decays [221]. Much larger widths are expected for charmonia states at this mass; therefore, its possible interpretations as a molecular state, a tetraquark state, a hybrid state or a rescattering effect have been discussed. The $X(4140)$ structure was confirmed by CMS [222] and D0 [223,224]; however, searches in $B^+ \to J/\psi\phi K^+$ decays were negative in the Belle [225,226] and BaBar [227] experiments.

Using a 0.37 fb^{-1} data-set at $\sqrt{s} = 7$ TeV $(346 \pm 20$ signal $B^+ \to J/\psi\phi K^+$ decays) LHCb initially found no evidence for the narrow $X(4140)$ structure [228], in 2.4σ disagreement with the measurement by CDF, as seen in Fig 47 (left). However, using a significantly larger sample of 4286 ± 151 $B^+ \to J/\psi\phi K^+$ decays (the Run 1 data-set), with roughly uniform efficiency across the entire $J/\psi\phi$ mass region, LHCb performed a full amplitude analysis, including resonant contributions from K^* resonances decaying into ϕK^+ and possible resonances in the $J/\psi\phi$ sys-

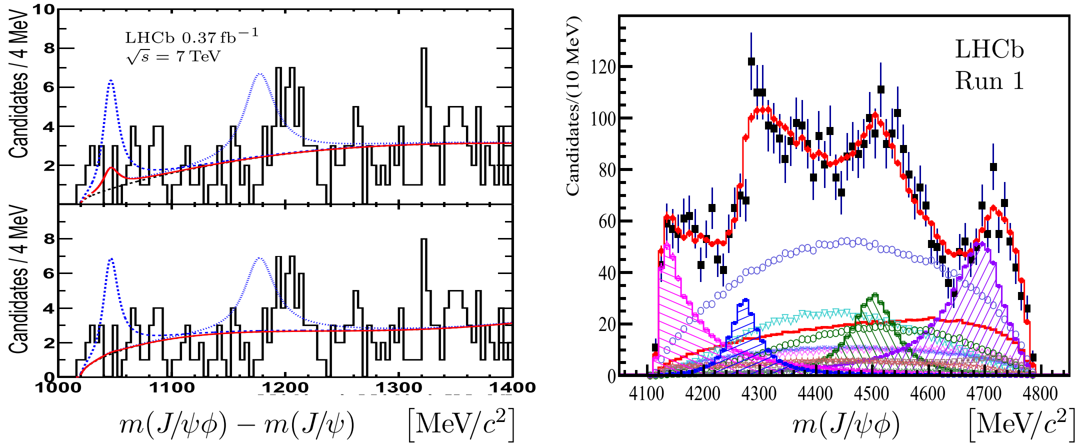

Fig. 47 (left) The distribution of mass difference $m(J/\psi\phi) - m(J/\psi)$ in a $0.37\,\mathrm{fb}^{-1}$ data-set for selected $B^+ \to J/\psi\phi K^+$ candidates [228]. A fit of the $X(4140)$ signal on top of a smooth background is superimposed (solid red line). The dashed blue (dotted blue) lines illustrate the expected $X(4140)$ ($X(4274)$) signal yield from the CDF measurement [221]. The top and bottom plots differ by the background function used in the fit: (top) an efficiency-corrected three-body phase-space; (bottom) a quadratic function multiplied by the efficiency-corrected three-body phase-space factor. (right) The distribution of $J/\psi\phi$ mass in the full Run 1 data-set for $B^+ \to J/\psi\phi K^+$ candidates (black data points) compared with the results of the amplitude fit containing eight $K^{*+} \to \phi K^+$ contributions (shown with open symbols) and five $X \to J/\psi\phi$ resonance contributions (shown as hatched histograms) [144,145]. The total fit is given by the red histogram

tem [144,145]. Four resonance contributions labeled as $X(4140)$, $X(4274)$, $X(4500)$ and $X(4700)$ with quantum numbers 1^{++}, 1^{++}, 0^{++} and 0^{++}, respectively, are observed, as shown in Fig. 47 (right). The statistical significance varies from 5.6 to 8.4σ. The widths of the states are found to be between 56 and 120 MeV, significantly exceeding the narrow-width of the $X(4140)$ reported by CDF.

The charged charmonium-like state $Z_c(4430)^-$ was first observed by the Belle collaboration in the $\psi(2S)\pi^-$ mass spectrum of $B^0 \to \psi(2S)K^-\pi^-$ decays [229]. The state appeared as a narrow ($\Gamma = 44^{+17+30}_{-13-11}$ MeV) structure with a significance of 6.5σ. Later, the collaboration performed a full amplitude analysis of $2010 \pm 50 \pm 40$ $B^0 \to \psi(2S)K^-\pi^-$ signal decays, determining the quantum numbers as $J^P = 1^+$, and finding a much broader width of $\Gamma = 200^{+41+26}_{-46-35}$ MeV [230].

The LHCb experiment has collected about 25,000 signal B^0 decays (the Run 1 data set) and observed the $Z_c(4430)^-$ with a significance exceeding 13.9σ [139]. Model-independent as well as full amplitude analyses were performed. The spin-parity is confirmed as 1^+, other hypotheses are excluded by at least 9.7σ.

Exotic particles with quantum numbers which can decay into $\eta_c\pi^-$ are predicted in several models [231]. Using a $4.7\,\mathrm{fb}^{-1}$ data sample at 7, 8 and 13 TeV, the LHCb collaboration has performed a Dalitz-plot analysis of $B^0 \to \eta_c K^+\pi^-$ decays, where the η_c meson is reconstructed in the $\eta_c \to p\bar{p}$ final state [232]. Evidence was found for a new exotic resonance in the $\eta_c\pi^-$ system, later dubbed the $X(4100)^-$ by the PDG. The significance of this new resonance exceeds three standard deviations.

5.7 Structures in the $J/\psi J/\psi$ mass spectrum

The production of $J/\psi J/\psi$ pairs in high-energy pp collisions was observed for the first time by the LHCb experiment using a $37.5\,\mathrm{pb}^{-1}$ data sample collected in 2010 at $\sqrt{s} = 7$ TeV [233]. The $J/\psi J/\psi$ mass spectrum was studied in a sample of 116 ± 16 signal pairs, and no structures was found. The subsequent analysis of $279\,\mathrm{pb}^{-1}$ of data collected in 2015 at $\sqrt{s} = 13$ TeV [234] showed the dominant role of the double-parton scattering (DPS) mechanism for $J/\psi J/\psi$ production over the single-parton scattering mechanism (SPS). This in turn includes both a non-resonant SPS contribution and $cc\bar{c}\bar{c}$ tetraquark production. Using the full Run 1 and 2 data-set, the $J/\psi J/\psi$ mass spectrum was studied in more detail [235]. The data, shown in Fig. 48, were found to be inconsistent with the hypothesis of non-resonant SPS plus DPS in the range $6.2 < m_{J/\psi J/\psi} < 7.4\,\mathrm{GeV}/c^2$, where $cc\bar{c}\bar{c}$ tetraquarks decaying into $J/\psi J/\psi$ pairs are expected. A narrow peaking structure at $m_{J/\psi J/\psi} \approx 6.9\,\mathrm{GeV}/c^2$ matching the lineshape of a resonance, and a broader structure near to threshold, were found.

The global significances of the broader structure close to threshold or the narrow peak around $6.9\,\mathrm{GeV}/c^2$ (provided that the other structure exists) are determined to be larger than 5 standard deviations. The structures are consistent with hadron states made up of four charm quarks, alternatively they may also result from near-threshold rescattering effects, as the $\chi_{c0}\chi_{c0}$ and $\chi_{c1}\chi_{c0}$ thresholds sit at $6829.4\,\mathrm{MeV}/c^2$ and $6925.4\,\mathrm{MeV}/c^2$, respectively.

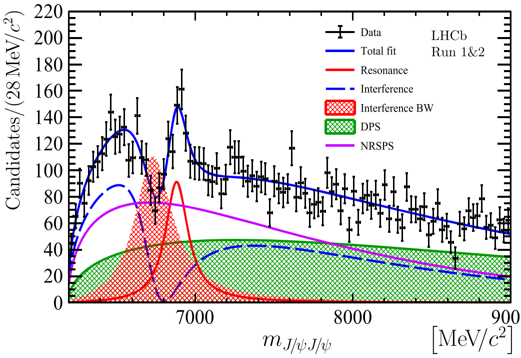

Fig. 48 The J/ψ-pair mass spectrum with the fit result superimposed. The fit accounts for the interference between a resonance and non-resonant SPS contribution [235]

5.8 Light hadron spectroscopy

$\eta-\eta'$ mixing has been studied by LHCb in $B^0_{(s)} \to J/\psi\eta^{(\prime)}$ decays, resulting in four observed decays modes, using the Run 1 data-set [236]. The η and η' were identified in the decay modes $\eta' \to \eta\pi^+\pi^-$, $\eta \to \pi^+\pi^-\pi^0$ and $\eta' \to \rho^0\gamma$. For decays of B^0_s (B^0) mesons, the $\eta^{(\prime)}$ mesons are formed from initial $s\bar{s}$ ($d\bar{d}$) quark pairs; hence, the measurement of the ratios of branching fractions of these decays allows a precise measurement of the $\eta-\eta'$ mixing angle. It also probes the gluonium component in the η' meson.

Excited strange mesons have been studied in the ϕK^+ system from a full amplitude fit of $B^+ \to J/\psi\phi K^+$ decays using the LHCb Run 1 data-set [144,145]. Even though no peaking structures are observed in the ϕK^+ mass distributions. Correlations in the decay angles reveal a rich spectrum of K^{*+} resonances. In addition to the angular information contained in the K^{*+} and ϕ decays, the J/ψ decay also helps to probe these resonances, as the helicity states of the K^{*+} and J/ψ mesons originating from the B^+ decay must be equal. Unlike the earlier scattering experiments investigating $K^* \to \phi K$ decays, a good sensitivity to states with both natural and unnatural spin-parity combinations is achieved.

The dominant 1^+ partial wave has a substantial non-resonant component, and at least one resonance that has a significance of 7.6σ. There is also 2σ evidence that this structure can be better described with two resonances matching expectations for two $2P_1$ excitations of the kaon. Also prominent is the 2^- partial wave which contains at least one resonance at 5.0σ significance. This structure is also better described with two resonances at 3.0σ significance. Their masses and widths are in good agreement with the well-established $K_2(1770)$ and $K_2(1820)$ states, matching the predictions for the two $1D_2$ kaon excitations. The 1^- partial wave exhibits 8.5σ evidence for a resonance which matches the $K^*(1680)$ state, which was well established in other decay modes, and matches expectations for the 1^3D_1 kaon excitation. This is the first observation of its decay to the ϕK final state. The 2^+ partial wave has a smaller intensity but provides 5.4σ evidence for a broad structure that is consistent with the $K_2^*(1980)$ state, previously observed in other decay modes, and matches expectations for the 2^3P_2 state. The $K(1830)$ state (3^1S_0 candidate), earlier observed in the ϕK decay mode in K^-p scattering, is also confirmed at 3.5σ significance. Its mass and width is now properly evaluated with uncertainties for the first time.

6 Measurements not originally planned in LHCb

While originally designed to study the production and decay of b and c hadrons, LHCb has extended its physics programme to also include other areas, such as physics with jets, the production of W and Z bosons, searches for new particles in open mode and nuclear collisions. Selected highlights are summarised below.

6.1 Production of EW bosons W and Z

LHCb has measured the production of Z and W bosons inclusively [237] and in association with jets, reconstructed in mainly muonic final states, using the data collected at $\sqrt{s} = 8$ TeV [238]. Also decays to e^+e^- [239], $\tau^+\tau^-$ [240] and $e\nu$ [241] have been measured; however, the muon channel is the most efficient due to the excellent performance of the muon system (see Sect. 2.6). The $Z \to \mu^+\mu^-$ decay shows a spectacularly clean signal, as shown in Fig. 49a [242]. The $W \to \mu\nu$ channel also manifests in a clear signal, as shown in Fig. 49b [237]. The absolute and differential cross sections, their ratios and charge asymmetries have been measured and compared to theoretical predictions. Figure 50 (Left) shows the comparison of W and Z cross-section measurements to SM predictions, showing good agreement.

6.2 Jets in LHCb

Measurements of jets at LHCb address several interesting areas of study:

- Jet properties and heavy-quark jet tagging;
- The constraining of proton parton density functions (PDFs) and to probe hard QCD in a unique kinematic range. Figure 51 shows the domain in the (x,Q^2) plane covered by the LHCb detector, complementing the kinematic ranges of ATLAS and CMS;
- Direct searches for the Higgs boson decaying to $b\bar{b}$ and $c\bar{c}$ final states;
- Direct searches for long-lived beyond-the-SM particles decaying into jets.

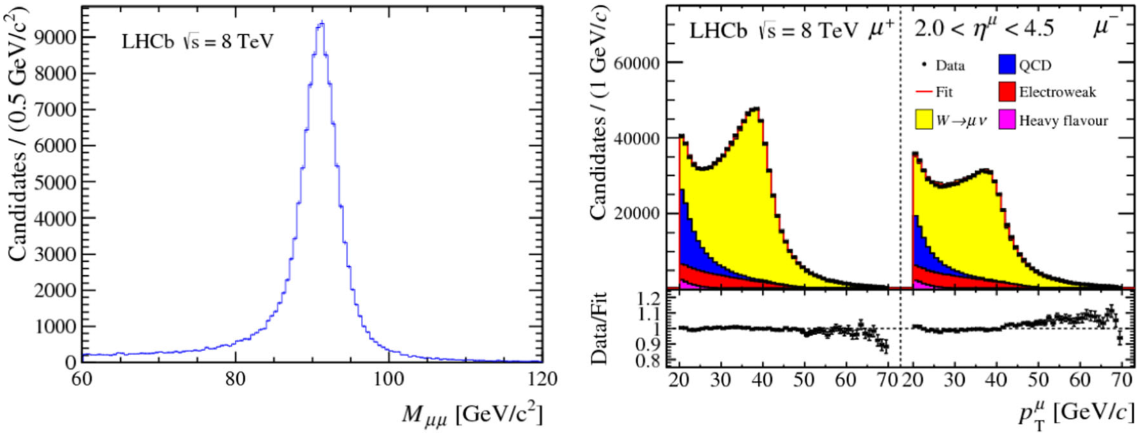

Fig. 49 **a** Invariant mass distribution of dimuon pairs in the Z-candidate sample. **b** LHCb data compared to QCD, electroweak and heavy flavour background, for positive (left) and negative (right) muon p_{T} spectra of W candidates [237]

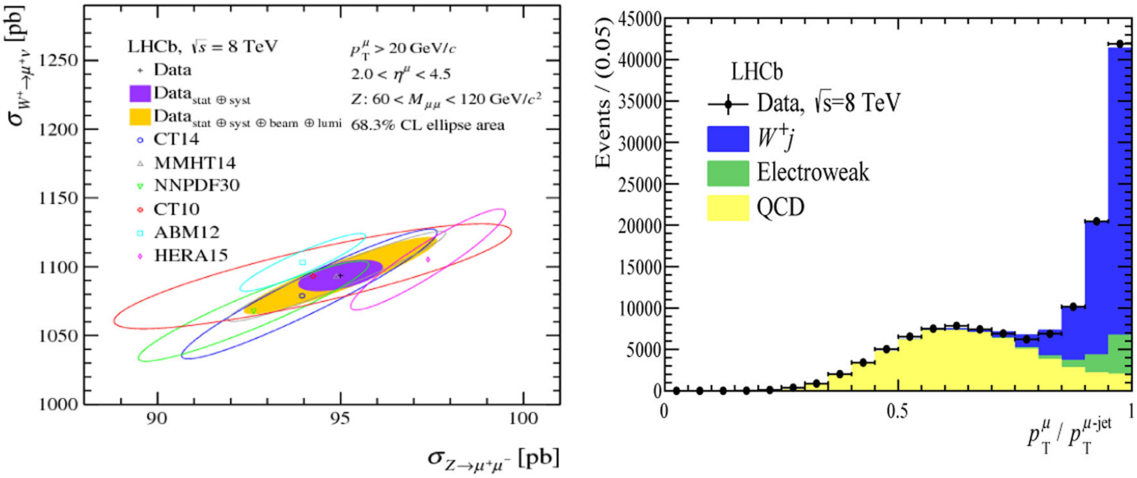

Fig. 50 (Left) The W versus Z measured production cross sections, showing comparison with theoretical predictions. (Right) Contributions to the selected W plus jet sample in the discriminating variable $p_T^\mu/p_T^{\mu-jet}$ (described in the text)

Jets are reconstructed in LHCb using a particle flow algorithm [243] clustered using the anti-kT algorithm with $\mathrm{R} = 0.5$ [244]. The calibration of jet reconstruction is performed in data using $Z \to \mu^+\mu^-$ decays which also contain a jet, where the jet is reconstructed back-to-back with respect to the Z. The efficiency for reconstructing and identifying jets is around 90% for jets with transverse momentum $p_{\mathrm{T}} > 20$ GeV/c. Furthermore, LHCb has developed a method to tag jets [243] and to determine whether they correspond to a b or c quark or to a lighter quark. Jets are tagged whenever a secondary vertex (SV) is reconstructed close enough to the jet in terms of $\mathrm{R} = \sqrt{(\Delta\phi^2 + \Delta\eta^2)}$. This provides a light-jet mistag rate below 1%, with an efficiency for b (c) jets of $\sim 65\%$ ($\sim 25\%$).

Moreover, using the SV and jet properties, two boosted decision trees (BDTs) have been developed, one to separate heavy from light jets and one to separate b from c jets. A summary of the obtained performance is shown in Fig. 52, where the efficiency of flavour identification is plotted as a function of the misidentification of light jets.

Production of W and Z with jets. W and Z production have also been studied in association with jets [238], in $W+j$, $Z+j$, $W+b\bar{b}$ and $W+c\bar{c}$. Jets are reconstructed as described above, while Z and W bosons are reconstructed mainly in muonic final states. The production of W boson plus jets is discriminated from misidentified QCD background processes using a muon isolation variable, which is built as the ratio between the p_T of the jet containing the muon and the p_T of the muon alone. Figure 50b shows the distribution of this variable, with genuine muons from the W boson peaking at 1. Figure 53 shows the comparison of the measured cross sections in LHCb with theoretical expectations, showing very good agreement.

LHCb has measured the $W^\pm + b\bar{b}$, $W^\pm + c\bar{c}$, production cross sections using a sample of pp collisions taken at $\sqrt{s} = 8$ TeV with a high-p_{T} isolated lepton from the W decay (electron or muon) and two heavy flavour (b or c) tagged jets in the final state.

The heavy-quark tagging uses the method described above. In this analysis, the $W + c\bar{c}$ channel is studied for the first time.

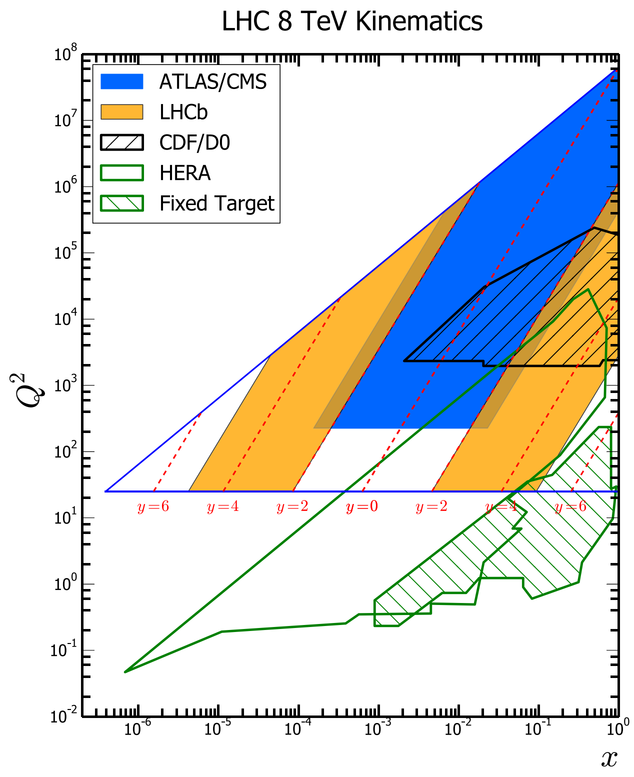

Fig. 51 The region in the $x - Q^2$ plane probed by LHCb, compared to ATLAS, CMS and previous experiments

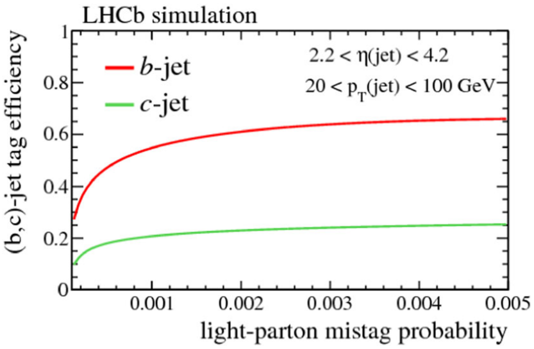

Fig. 52 Simulated efficiencies for SV-tagging a b, c-jet as a function of mistag probability for a light-quark jet

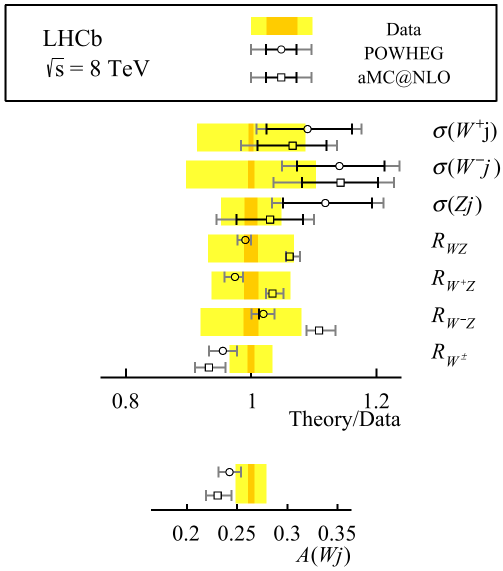

Fig. 53 Comparison with theoretical calculations of measured cross sections for W and Z production accompanied by jets. The orange bands represent the statistical uncertainty only, the yellow bands are the quadratic sum of statistical and systematic uncertainties

In order to extract the different signal components, a simultaneous four-dimensional fit is performed on the μ^+, μ^-, e^+ and e^- samples. Here the electron channels are used to increase statistics. The four variables used in the fit are the dijet mass, a multivariate discriminator to separate $t\bar{t}$ from $W + b\bar{b}$ and $W + c\bar{c}$ events and a multivariate discriminator to separate b- and c-jets, used for both accompanying jets [245]. In this fit, the background from QCD multi-jets is extrapolated from a control sample in data, while other background contributions are fixed to SM theoretical expectations. Only the signal components are then unconstrained. The projections of the resulting fit on four input variables for the μ^+ sample are illustrated in Fig. 54. The statistical significance of the measured $W^+ + b\bar{b}$, $W^+ + c\bar{c}$, $W^- + b\bar{b}$, $W^- + c\bar{c}$ and $t\bar{t}$ production cross sections are 7.1σ, 4.7σ, 5.6σ, 2.5σ and 4.9σ, respectively. The cross sections measured in the LHCb fiducial acceptance agree well with the Next-to-Leading-Order (NLO) theory predictions.

Search for long-lived new particles. The LHCb detector has been designed to measure very rare decays of b quarks, with the aim of detecting the presence of new beyond-the-SM particles through their couplings in loops, which could change the expected SM branching ratios. This implies reaching mass scales higher than those explored in *open* new particle searches, where the particle is produced directly in pp collisions. The traditional way to search for new particles is, as for ATLAS and CMS, reconstructing their decays through exclusive final states in their invariant masses, or with missing energy techniques. Here hermiticity is a mandatory feature of the detector. In all cases, assumptions on their coupling, their production mechanism, and on their decay modes must be made, and the search is therefore guided by theoretical models.

For LHCb, the most promising final states are those decays which form a secondary vertex, for which the LHCb VELO (see Sect. 2.2) is extremely efficient, i.e. the new particles are long lived.

Several negative results have been published which are often less sensitive than the General-Purpose Detector (GPD) results. However in some cases, LHCb can extend the exclusion region. An example is given in Fig. 55 for a Higgs-like particle H^0 decaying into jets

Fig. 54 Projections of the simultaneous four-dimensional fit for the μ^+ sample [245] to: **a** the dijet mass, **b** the discriminator to separate $t\bar{t}$ from $W+b\bar{b}$ and $W+c\bar{c}$ and **c** the discriminator to separate b and c leading jets **d** sub-leading jets. In light blue is $W+b\bar{b}$, in green $t\bar{t}$, in red $W+c\bar{c}$ and in black the background

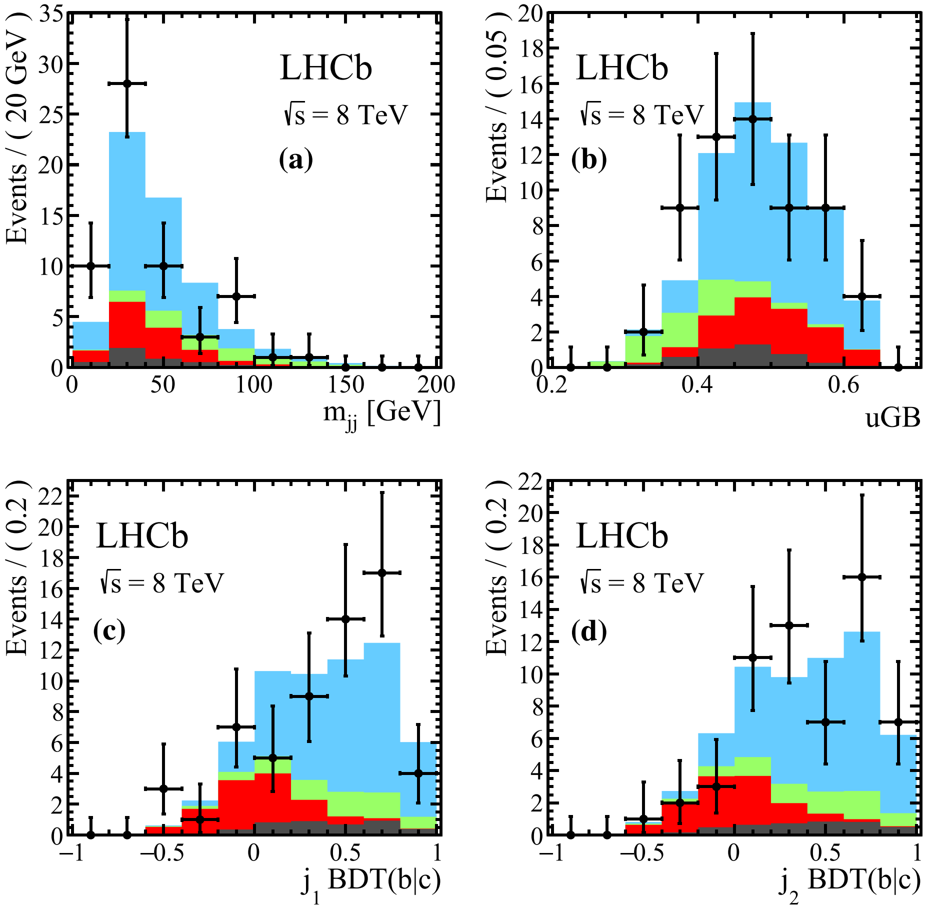

forming a separate secondary vertex. The LHCb exclusion region is compared with that of ATLAS and CMS, which demonstrates the complementarity of the LHC experiments. The limits are, in this specific case, competitive, despite a factor 10 less luminosity.

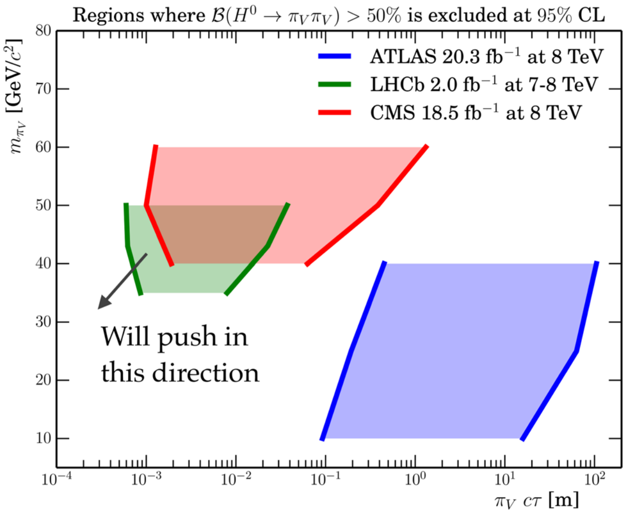

Fig. 55 Comparison of the LHCb exclusion region for the Branching Ratio of H $H^0 \to \pi_V \pi_V$, where π_V is a long-lived particle decaying to jets. Exclusion regions for ATLAS and CMS are also shown

Production of $t\bar{t}$ pairs. Top quark production is an excellent example where the forward acceptance of the LHCb detector has several advantages with respect to the central region instrumented by ATLAS and CMS. The t quark cross section can provide important constraints on the large-x gluon PDF, where the forward kinematic region is particularly sensitive. In addition, the forward region provides a greater fraction of events with quark-initiated production than in the central region and enhances the size of $t\bar{t}$ asymmetries visible at LHCb. The challenge for LHCb to measure $t\bar{t}$ production is the small acceptance and the impossibility of a missing energy measurement. Also the fact that the luminosity is limited by the need to reduce multiple interactions for measurements in the b sector, disfavours $t\bar{t}$ statistics.

Top-quark production is presented here at $\sqrt{s}$=13 TeV, which gives an increase in the production rate of an order of magnitude with respect to 8 TeV, and which brings these new channels into statistical reach. The $t\bar{t}$ analysis is based on an integrated luminosity of 2 fb^{-1}, and with $e\mu b$ measured in the final state. Hence, the final state is the decay chain $t\bar{t} \to bW^+bW^- \to e^+\mu^-bb$, where at least one b-jet is reconstructed. This is a very pure final state, as the second lepton suppresses $W + b\bar{b}$ production and the different flavoured leptons suppress $Z + b\bar{b}$. The signal purity is illustrated in Fig. 56a, and the observable cross section is measured to be $\sigma_{t\bar{t}} = 126 \pm 19(\,(\text{stat})) \pm 16(\,(\text{syst})) \pm 5(\text{lumi})$ fb, which is compatible with SM predictions.

$Z \to b\bar{b}$ decay. This measurement is an important validation of the LHCb jet reconstruction and b-tagging performance. Two b-tagged jets are reconstructed, with a third balancing jet also reconstructed to help control the QCD background and define signal and control regions using a multivariate technique. The background-subtracted signal distribution is shown in Fig. 56b [246]. The signal is observed with a statistical significance of 6σ and the measured cross section is found to be compatible with SM predictions at next-to-leading order.

6.3 Dark photons

The possibility that dark matter particles may interact via unknown forces, almost not felt by SM particles, has motivated substantial effort to search for dark-sector forces (see [247] for a review). A dark-force scenario involves a massive dark photon, A'.

In the minimal model, the dark photon does not couple directly to charged SM particles, but it can gain a weak coupling to the SM electromagnetic current via kinetic mixing. The strength of this coupling is suppressed by a factor ϵ with respect to the SM photon. If the kinetic mixing arises from processes whose amplitudes involve one or two loops containing high-mass particles, perhaps even at the Planck scale, then $10^{-12} \leq \epsilon^2 \leq 10^{-4}$ is expected [247].

Constraints have been placed on visible A' decays by previous beam-dump, fixed-target, collider and rare meson decay experiments; the few-loop region is ruled out for dark photon masses $m(A') \sim 10\ \text{MeV}/c^2$. Additionally, the region $\epsilon^2 < 5 \times 10^{-7}$ is excluded for $m(A') < 10.2\ \text{GeV}/c^2$, along with about half of the remaining few-loop region below the dimuon threshold. Many ideas have been proposed to further explore the $[m(A'), \epsilon^2]$ parameter space, including an inclusive search for $A' \to \mu^-\mu^+$ decays with the LHCb experiment. A dark photon produced in proton–proton collisions via γ^*A' mixing inherits the production mechanisms of an off-shell photon with $m(\gamma^*) = m(A')$; therefore, both the production and decay kinematics of the $A' \to \mu^+\mu^-$ and $\gamma^* \to \mu^+\mu^-$ processes are identical.

LHCb has performed searches for both prompt-like and long-lived dark photons [248] produced in pp collisions at a centre-of-mass energy of 13 TeV, using $A' \to \mu^+\mu^-$ decays and a data sample corresponding to an integrated luminosity of 1.6 fb^{-1} collected during 2016. The prompt-like A' search is performed from near the dimuon threshold up to 70 GeV, above which the $m(\mu^+\mu^-)$ spectrum is dominated by the Z boson. The prompt-like dimuon spectrum is shown in Fig. 57.

Three main types of background contribute to the prompt-like A' search: prompt off-shell $\gamma^* \to \mu^+\mu^-$, which is irreducible; resonant decays to $\mu^+\mu^-$, whose mass peak regions are excluded in the search (see Fig. 57), and various types of misidentification, which are highly suppressed by the stringent muon-identification and prompt-like requirements applied in the trigger.

For the long-lived dark photon search, i.e. with displaced dimuon vertices, the stringent criteria applied in the trigger make contamination from prompt muon candidates negligible. The long-lived A' search is restricted to the mass range $214 \leq m(A') \leq 350\ \text{MeV}/c^2$, where the data sample potentially provides sensitivity. In this case, the background composition is dominated by photon conversions to $\mu^+\mu^-$ in the VELO, b-hadron decays where two muons are produced in the decay chain, and the low-mass tail from $K^0_\text{S} \to \pi^+\pi^-$ decays where both pions are misidentified as muons.

In the dark-photon searches, no evidence for a signal is found, and 90% CL exclusion regions are set on the $\gamma - A'$ kinetic-mixing strength, as shown in Fig. 58. The constraints placed on prompt-like dark photons are the most stringent to date for the mass range $10.6 \leq m(A') \leq 70\ \text{GeV}/c^2$ and are comparable to the best existing limits for $m(A') \leq 0.5\ \text{GeV}/c^2$. The search for long-lived dark photons is the first to achieve sensitivity using a displaced-vertex signature. These results demonstrate the unique sensitivity of the LHCb experiment to dark photons, even using a data sample collected with a trigger that is inefficient for low-mass $A' \to \mu^+\mu^-$ decays. Using knowledge gained from this analysis, the software-trigger efficiency for low-mass dark photons has been significantly improved for 2017 data taking.

In Run 3 to come, the planned increase in luminosity and removal of the hardware- trigger stage should increase the number of expected $A' \to \mu^+\mu^-$ decays in the low-mass region by $\mathcal{O}(100 - 1000)$ compared to the 2016 data sample.

6.4 Nuclear collisions

Ultra-relativistic heavy-ion collisions allow the study of the so-called Quark-Gluon Plasma (QGP) state of matter, a hot and dense medium of deconfined quarks and gluons where heavy quarks are crucial probes.

Produced via hard interactions at the early stage of the nucleus–nucleus collision, before the QGP formation, heavy quarks experience the entire evolution of the QGP. A correct interpretation of these probes requires a full understanding of Cold Nuclear Matter (CNM) effects, which are present regardless of the formation of the deconfined medium. To disentangle the CNM from genuine QGP effects, heavy-flavour production in proton–nucleus collisions is studied.

The LHCb experiment has collected data of proton–lead (pPb) and lead–lead (PbPb) collisions. Since the LHCb detector covers only one direction of the full

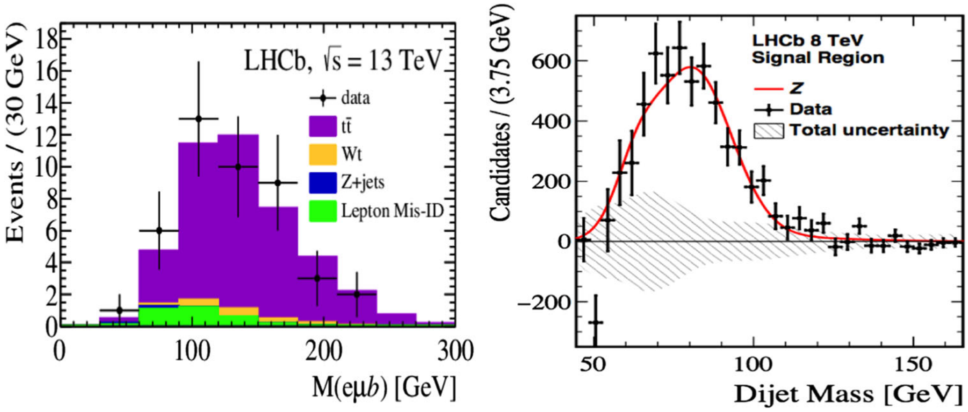

Fig. 56 (Left) The $e\mu b$ invariant mass for all 44 selected $t\bar{t}$ candidates illustrates the excellent signal purity. (Right) The background-subtracted dijet mass spectrum showing the $Z \to b\bar{b}$ signal [246]

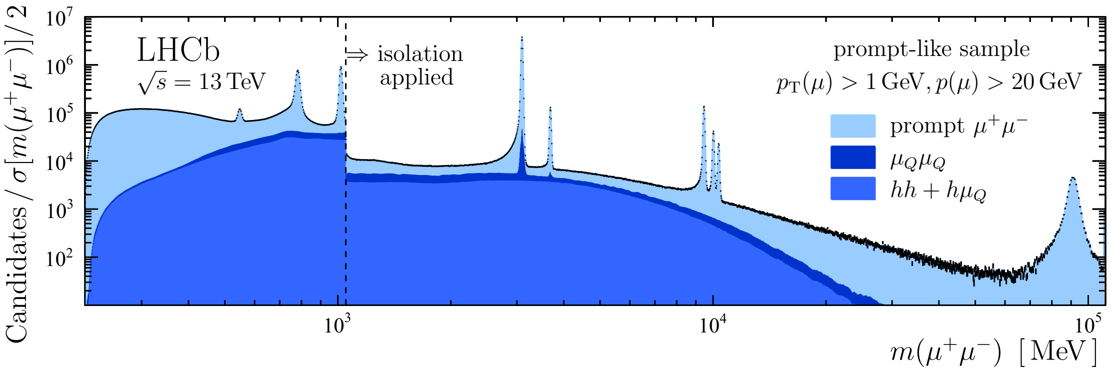

Fig. 57 The prompt-like $\mu^+\mu^-$ mass spectrum

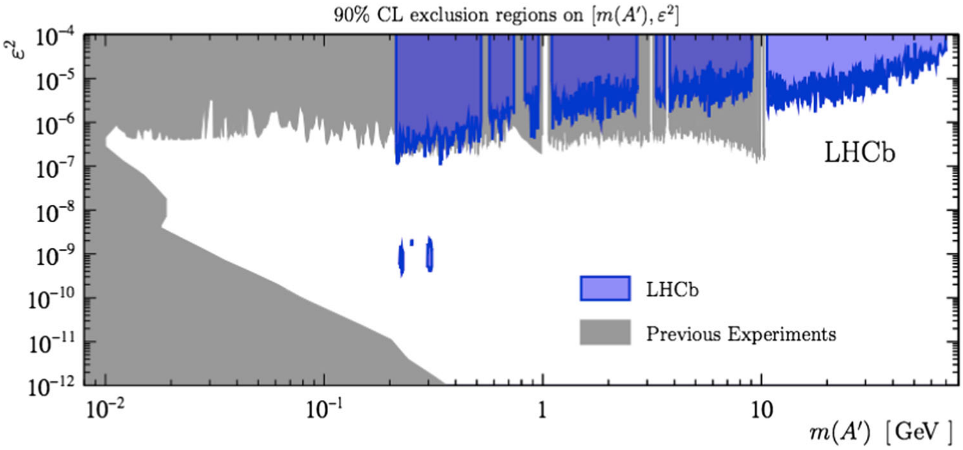

Fig. 58 Results of the dark photon search. Both prompt-like (top) and displaced (centre) exclusions are shown

acceptance, there are two distinctive beam configurations for the pPb collisions. In the forward (backward) configuration, the proton (lead) beam enters the LHCb detector from the interaction point. The proton beam and the lead beam have different energies per nucleon in the laboratory frame; hence, the nucleon–nucleon centre-of-mass frame is boosted in the proton direction with a rapidity, y, shift. This results in the LHCb acceptance for the forward configuration as $1.5 < y < 4$, and for the backward configuration $-5 < y < -2.5$.

In addition, LHCb provides the unique capability at the LHC to collect fixed-target collisions utilising the System for Measuring the Overlap with Gas (SMOG) system [249]. Originally designed for precise luminosity measurements, SMOG provides the injection of a noble gas such as argon or helium inside the primary LHC vacuum around the VELO detector with pressure $\mathcal{O}(10^{-7})$ mbar, allowing measurements of p-gas and ion-gas collisions, and operating LHCb as a fixed target experiment. Since 2015, LHCb has exploited SMOG in physics runs using special fills not devoted to pp physics, with a variety of beam (p or Pb) and target configurations. This allows unique production studies which are relevant to cosmic ray and heavy-ion physics.

The heavy-ion results on heavy-flavour production in pPb, PbPb and fixed-target collisions collected by

LHCb bring yet more diversity and complementarity into the field. Also in this context, the excellent momentum resolution and particle identification provided by LHCb are especially suited for measuring heavy quark production. The LHCb collaboration joined the other participants into the LHC heavy-ion collider programme with a pPb run at 5 TeV in 2013 and with a PbPb run in 2015. Following these pioneering data runs, significantly larger data-sets have been successfully recorded.

Fixed target collisions. LHCb has reported first measurements of heavy-flavour production with the fixed-target mode [250]. J/ψ production cross sections and D^0 yields have been measured in pHe collisions at $\sqrt{s_{NN}} = 86.6$ GeV and pAr collisions at $\sqrt{s_{NN}} = 110.4$ GeV, over the rapidity range $2 < y < 4.6$. The cross-section measurements are made for pHe data only, since the luminosity determination is only available for this sample. After correction for acceptances, efficiencies and branching fractions, the cross sections are extrapolated to the full phase space. The D^0 measurement is used to extract the $c\bar{c}$ cross section. The J/ψ and $c\bar{c}$ measurements are compared in Fig. 59 with other experiments at different centre-of-mass energies and with theoretical predictions.

With pHe data, LHCb also measured the antiproton production cross section [251], a very interesting direct determination, helping the interpretation of the antiproton cosmic-ray flux detected by space experiments [252].

Collider mode. In collider mode, the LHCb experiment has collected proton–lead collision data at $\sqrt{s_{NN}} = 5$ TeV in 2013 and at 8.16 TeV in 2016. The 2013 data sample corresponds to an integrated luminosity of 1.06 ± 0.02 nb^{-1} for the forward and 0.52 ± 0.01 nb^{-1} for the backward regions, while the 2016 data corresponds to 13.6 ± 0.3 nb^{-1} for the forward and 20.8 ± 0.5 nb^{-1} for the backward. These data samples are used to measure quarkonium and open charm or beauty production.

Υ(nS)-meson production is studied in the decay to two opposite-sign muons [253]. The measurements include the differential production cross sections of Υ(1S), Υ(2S) states and nuclear modification factors, performed as a function of transverse momentum and rapidity in the nucleon–nucleon centre-of-mass frame of the Υ(nS) state. Also the production cross sections for the Υ(3S) are measured, integrated over phase space, and the production ratios between all three Υ(nS) states are determined.

The three states are well identified in both pPb and Pbp configurations as shown in Fig. 60. The nuclear modification factors are compared with theoretical predictions, and suppressions for bottomium in pPb collisions are observed. The LHCb measurements improve the understanding of cold nuclear matter effects down to low p_{T}.

7 Future prospects

Over the years 2011–2018, both the LHC machine and the LHCb detector performed extremely well, providing great improvements with respect to the B Factory measurements, in particular the pioneering CP violation measurements (Sect. 3), the observation of the rarest beauty meson decays (Sect. 4) and the discovery of pentaquarks (Sect. 5). LHCb also observed and reported a number of interesting hints of anomalies related to the flavour sector, which has generated much theoretical attention, especially relating to rare decays and lepton flavour universality. The precision achieved by the experiment is in line with prior expectations, as documented in [254], and which demonstrates the remarkable understanding of all aspects of the detector.

To further pursue these exciting results and fully exploit the flavour physics potential of the LHC, the LHCb detector required an upgrade, to increase the rate and efficiency of data taking beyond the Long Shutdown 2 (LS2). Consequently, the LHCb detector is now undergoing a major upgrade that is well underway and will allow the experiment to pursue its superb performance into the future.

At present, the hardware-based trigger limits the amount of data taken each year to a maximum of about 2 fb^{-1}. In addition, most of the detector sub-systems would not cope with higher luminosity due to either their outdated readout electronics or radiation-induced damage sustained during Run 1 and Run 2 data taking. The initial ideas regarding the upgrade were formulated in 2011 [255], and further solidified in 2012 when the Technical Design Report was released [256]. Many of the subdetector components are largely unchanged in the upgrade, with the exception of a new pixel vertex detector replacing the current VELO, the TT stations being replaced by a new silicon micro-strip upstream tracker (UT) and the straw outer chambers replaced by a scintillating fibre detector. Details of each subdetector upgrade can be found in refs. [256–260].

The crucial point of the upgrade project is to build a reliable and robust detector capable of operating at higher luminosity without compromising the excellent physics performance of the current detector. This, in turn, cannot be achieved by redesigning the hardware components alone, but has to be augmented by a new innovative and flexible trigger system. A critical part of the upgrade strategy is the design of a so-called triggerless front-end electronics system capable of reading out the full detector at 40 MHz, i.e. at the LHC clock frequency. Completely new and novel chips have been designed and tested for the pixel sensors [257] the UT [258] and RICH detectors [259].

The upgraded detector will operate at an instantaneous luminosity of $2 \cdot 10^{33}$ cm^{2}s^{-1} which allows collection of around 10 fb^{-1} of data per year as a target, also keeping pace with Belle II [261], the other major flavour-physics experiment. Figure 61 shows the corresponding time-line for LHCb operations over the next decade.

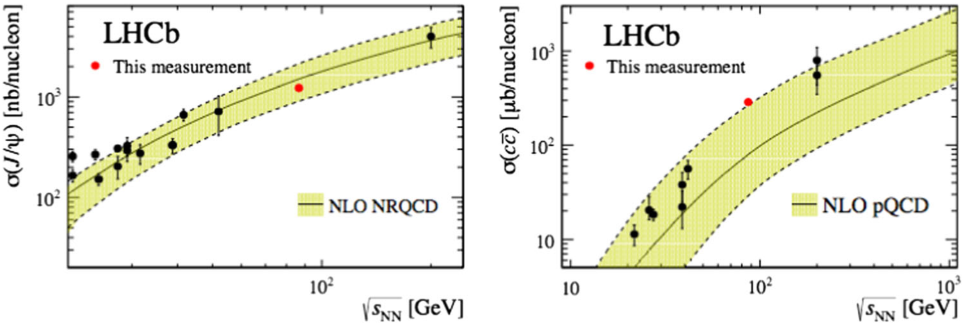

Fig. 59 J/ψ (left) and $c\bar{c}$ (right) cross-section measurements as a function of the centre-of-mass energy, compared with other experimental data (black points). The bands correspond to fits based on NLO NRQCD calculations for J/ψ and NLO pQCD calculations for $c\bar{c}$, respectively. More details are given in [250]

Fig. 60 Invariant-mass distribution of $\mu^+\mu^-$ pairs from the (left) pPb and (right) Pbp samples after trigger and offline selections

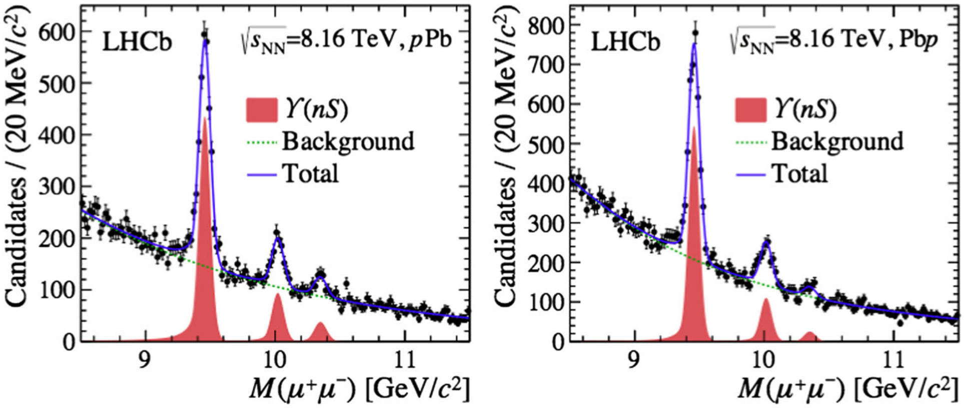

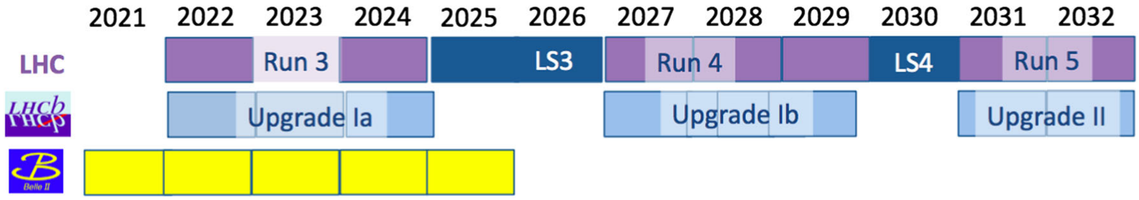

Fig. 61 A time-line showing the operations of the LHC and the HL-LHC over the next decade, including long shutdown (LS) periods, as can be estimated today. The operational periods of LHCb and Belle II are shown in [261]

To efficiently run at increased luminosity, the present hardware-based trigger will be replaced, and events will be selected by the software-based HLT alone. To cope with the much higher event rate (typically five proton–proton interactions per beam crossing), a flexible software trigger will be employed and coupled with a re-optimised network capable of handling a multi-terabyte data stream. The upgraded trigger will process every event (the visible rate at LHCb is estimated to reach 30 MHz) using information from every sub-detector to enhance its decision and maximise signal efficiencies, especially for the hadronic channels. The precision of particle identification and track-quality information will be identical than "offline" and able to reduce the rate down to 20–100 kHz. The new trigger strategy will increase the triggering efficiency for the hadronic channels by a factor 2 to 4 with respect to Run 1 [262], corresponding to an increase in a factor 10 to 20 for the hadronic yields.

Finally, plans for a further future upgrade (called Upgrade II) to use the full potential of flavour physics during the HL-LHC operation have now started [263, 264]. This upgrade would require a complete redesign of the detector able to take data at instantaneous luminosities of $2 \cdot 10^{34}$ cm^{2}s^{-1} and collect ~ 50 fb^{-1} of data per year, guaranteeing LHCb operation beyond 2030.

The LHCb Upgrades I and II will significantly improve the reach of key physics measurements. By way of example, the precision quoted in Sect. 3.3.3 on today's measurement of the CKM angle γ, $\mathcal{O}(5°)$, will be improved to 1° with the new Upgrade I hadronic trigger and luminosity increase. This further improves to 0.35° with the large statistics accumulated with LHCb Upgrade II. As discussed in Sect. 4.1, currently there is not enough sensitivity to measure the rare decay $\mathcal{B}(B^0 \to \mu^+\mu^-)$. With LHCb Upgrade I, a first observation should be possible, but it will require Upgrade II to reach a $\sim 10\%$ precision on its branching ratio. This sensitivity will allow a meaningful measurement of the ratio between B^0 and B_s^0 into the $\mu^+\mu^-$ final state and will constitute a clean and powerful test of extensions beyond the SM.

8 Summary and conclusions

In ten years of operation at the LHC, the LHCb experiment has delivered a remarkably rich programme of physics measurements. In this paper, the 25-year evolution of the experiment since its inception has been described, and its successes and achievements have been summarised. The diversity of the physics output has truly shown LHCb to be a "general-purpose detector in the forward region".

Over the last ten years, LHCb has measured the CKM quark mixing matrix elements and *CP* violation parameters to world-leading precision in the b– and c–quark systems. The experiment has measured very rare decays of b and c mesons and baryons, some with branching ratios down to order 10^{-9}, testing Standard Model predictions to unprecedented levels. Hints of new physics in rare-decay angular distributions and through tests of lepton universality in electron–muon decay modes have generated considerable theoretical interest. The global knowledge of b and c quark states has improved significantly, through discoveries of many new resonances already anticipated in the quark model, and also by the observation of new exotic tetraquark and pentaquark states. In addition, many interesting measurements have been made that were not anticipated in the original LHCb proposal, such as electroweak physics, jet measurements, new long-lived particle searches and heavy-ion physics. An incredibly rich harvest of fundamental results has been produced, many of these will remain in textbooks for years to come.

LHCb has recently been upgraded and will start data-taking early in 2022 at a factor 5 higher luminosity, incorporating new subdetectors and a software-based trigger. Statistics in hadronic modes will be improved by at a factor 10–20, allowing much more precise measurements, especially of very rare b- and c-hadron decays. In addition, the future planned Upgrade II at the (HL)-LHC early in 2030 will ensure that LHCb maintains its lead in flavour physics for at least the next two decades.

Acknowledgements LHCb is at present a collaboration of about 1000 authors. The rich variety of outstanding results has been made possible by the dedicated work of many colleagues: detector builders and operators, data verifiers and analysts. We would like to acknowledge the important roles played by T. Nakada as first spokesman and by the late H.J.Hilke as Technical Coordinator, who successfully managed the realisation of this very complex detector. Finally, we would also like to thank our colleagues P. Koppenburg and G. Passaleva who made helpful and insightful comments to this paper.

References

1. S.L. Glashow, J. Iliopoulos, L. Maiani, Weak interactions with Lepton–Hadron symmetry. Phys. Rev. D **2**, 1285 (1970)
2. SLAC-SP-017, J.E. Augustin, et al., Discovery of a Narrow Resonance in e^+e^- Annihilation. Phys. Rev. Lett. **33**, 1406 (1974)
3. E598, J.J. Aubert, et al., Experimental Observation of a Heavy Particle J, Phys. Rev. Lett. **33**, 1404 (1974)
4. M. Kobayashi, T. Maskawa, CP violation in the renormalizable theory of weak interaction. Prog. Theor. Phys. **49**, 652 (1973)
5. CLEO, S. Behrends, et al., Observation of exclusive decay modes of B flavored mesons. Phys. Rev. Lett. **50**, 881 (1983)
6. ARGUS, H. Schroder, Observation of B0 anti-B0 oscillations, in *International Europhysics Conference on High-energy Physics*, pp. 365–367 (1987)
7. ALEPH, CDF, DELPHI, L3, OPAL, SLD, D. Abbaneo et al., Combined results on B hadron production rates, lifetimes, oscillations and semileptonic decays, arXiv:hep-ex/0009052
8. K. Berkelman, E.H. Thorndike, Physics at the cornell electron storage ring. Ann. Rev. Nucl. Part. Sci. **59**, 297 (2009). https://doi.org/10.1146/annurev-nucl-010609-115108
9. P. Oddone, An asymmetric B factory based on PEP. Annals N. Y. Acad. Sci. **578**, 237 (1989)
10. J.P. Albanese et al., Direct observation of the decay of beauty particles into charm particles. Phys. Lett. B **158**, 186 (1985)
11. G. Fidecaro, Fixed target B physics at the LHC, in *ECFA Large Hadron Collider (LHC) Workshop: Physics and Instrumentation*, pp. 288–294 (1990)
12. K.P. Myznikov, L.D. Solovev, V.A. Yarba, IHEP accelerator and storage complex (UNK). Conf. Proc. C **8405141**, 95 (1984)
13. BEATRICE, M. Adamovich, et al., WA92: A Fixed target experiment to trigger on and identify beauty particle decays, Nucl. Instrum. Meth. A **379**, 252 (1996)
14. C.S. Mishra and P. McBride, (eds.), *B physics at hadron accelerators. Proceedings, Workshop, Snowmass, USA* (1993)
15. A. Brandt et al., Proposal to the SPSC: study of beauty physics at the SPS-collider with real-time use of sili-

con microvertex information. Nucl. Instrum. Methods Phys. Res. A **263**, 188 (1988)
16. J. Ellett, et al., R&D for collider beauty physics at the LHC , CERN-DRDC-91-18. DRDC-P-28, CERN, Geneva (1991)
17. P238, J. Ellett, et al., Development and test of a large silicon strip system for a hadron collider beauty trigger. Nucl. Instrum. Methods A **317**, 28 (1992)
18. HERA-B, P. Krizan, et al., HERA-B, an experiment to study CP violation at the HERA proton ring using an internal target. Nucl. Instrum. Methods A **351** (1994) 111 (1992)
19. E.L. Berger, R. Meng, Bottom quark cross-sections at collider and fixed target energies at the SSC and LHC, in *Summer Workshop on B Physics at Hadron Accelerators*, 0339–342 (1993) arXiv:hep-ph/9308372
20. COBEX, S. Erhan, M. Medinnis, J. Zweizig, COBEX: a Collider beauty experiment for the LHC. Nucl. Instrum. Methods A **351**, 132 (1994)
21. GAJET, P.D. Dauncey, T. Nakada, J.P. Perroud, The GAJET experiment at the LHC. Nucl. Instrum. Methods A **351**, 147 (1994)
22. LHB, R. Waldi, The LHB experiment. Nucl. Instrum. Methods A **351**, 161 (1994)
23. B.N. Jensen, et al., A proposal to test beam extraction by crystal channeling at the SPS: a first step towards a LHC extracted beam. CERN-DRDC-91-25. DRDC-P-29, CERN, Geneva (1991)
24. H. Akbari et al., First results on proton extraction from the CERN SPS with a bent crystal. Phys. Lett. B **313**, 491 (1993)
25. P.E. Schlein (ed), Proceedings, 2nd International Conference on B-Physics at Hadron Machines (Beauty 1994): Le Mont Saint Michel, France, April 24–29, 1994, Nucl. Instrum. Methods A **351**, 1 (1994)
26. H. Dijkstra, et al., LHC-B Letter of Intent, LHC-B Collaboration, LHCB-95-001, CERN-LHCB-95-001 (1995)
27. A. Kulyavtsev, et al., Proposal for an Experiment to Measure Mixing, CP Violation and Rare Decays in Charm and Beauty Particle Decays at the Fermilab Collider—BTeV, Fermilab-Proposal-0918 (2000)
28. LHCb Collaboration, S. Amato, et al., LHCb technical proposal: a Large Hadron Collider Beauty Experiment for Precision Measurements of CP Violation and Rare Decays, CERN-LHCC-98-04, CERN-LHCC-98-4, CERN-LHCC-P-4 (1998)
29. LHCb collaboration, LHCb technical design report: reoptimized detector design and performance, CERN-LHCC-2003-030 (2003)
30. LHCb Collaboration, A.A. Alves Jr., et al., The LHCb detector at the LHC. JINST **3**, S08005 (2008)
31. R. Aaij et al., Performance of the LHCb vertex locator. JINST **9**, P09007 (2014). arXiv:1405.7808
32. R. Arink et al., Performance of the LHCb outer tracker. JINST **9**, P01002 (2014). arXiv:1311.3893
33. P. d'Argent et al., Improved performance of the LHCb Outer Tracker in LHC Run 2. JINST **12**, P11016 (2017). arXiv:1708.00819
34. LHCb collaboration, R. Aaij, et al., LHCb detector performance. Int. J. Mod. Phys. **A30**, 1530022 (2015). arXiv:1412.6352
35. Betata, A., et al., Calibration and performance of the LHCb calorimeters in Run 1 and 2 at the LHC. Rep No. LHCb-DP-2020-001 (2020). arXiv:2008.11556
36. M. Adinolfi et al., Performance of the LHCb RICH detector at the LHC. Eur. Phys. J. C **73**, 2431 (2013). arXiv:1211.6759
37. A.A. Alves Jr. et al., Performance of the LHCb muon system. JINST **8**, P02022 (2013). arXiv:1211.1346
38. LHCb, S. Amato, et al., LHCb technical proposal, CERN-LHCC-98-04
39. LHCb collaboration, LHCb trigger system: Technical Design Report, CERN-LHCC-2003-031 (2003)
40. R. Aaij et al., The LHCb trigger and its performance in 2011. JINST **8**, P04022 (2013). arXiv:1211.3055
41. R. Aaij et al., Performance of the LHCb trigger and full real-time reconstruction in Run 2 of the LHC. JINST **14**, P04013 (2019). arXiv:1812.10790
42. R. Aaij et al., A comprehensive real-time analysis model at the LHCb experiment. JINST **14**, P04006 (2019). arXiv:1903.01360
43. J.H. Christenson, J.W. Cronin, V.L. Fitch, R. Turlay, Evidence for the 2π decay of the K_2^0 Meson. Phys. Rev. Lett. **13**, 138 (1964)
44. BaBar, B. Aubert, et al., Observation of CP violation in the B^0 meson system. Phys. Rev. Lett. **87**, 091801 (2001). arXiv:hep-ex/0107013
45. Belle, K. Abe, et al., Observation of large CP violation in the neutral B meson system, Phys. Rev. Lett. **87**, 091802 (2001). arXiv:hep-ex/0107061
46. CDF, T. Affolder, et al., A measurement of $\sin(2\beta)$ from $B \to J/\psi K_S^0$ with the CDF detector. Phys. Rev. **D61**, 072005 (2000). arXiv:hep-ex/9909003
47. N. Cabibbo, Unitary symmetry and leptonic decays. Phys. Rev. Lett. **10**, 531 (1963)
48. L. Wolfenstein, Parametrization of the Kobayashi–Maskawa Matrix. Phys. Rev. Lett. **51**, 1945 (1983)
49. Particle Data Group, M. Tanabashi, et al., Review of particle physics. Phys. Rev. **D98**, 030001 (2018), and 2019 update
50. C. Jarlskog (ed.), *CP Violation*, vol. 3, WSP (1989)
51. S. Erhan, N. Harnew, U. Uwer, Proceedings, 12th International Conference on B physics at Hadron Machines (Beauty 2009): Heidelberg, Germany, September 7–11, 2009, Proceedings of Science **BEAUTY2009** (2009)
52. CKMfitter Group, J. Charles, et al., CP violation and the CKM matrix: Assessing the impact of the asymmetric B factories. Eur. Phys. J. **C41**, 1 (2005). arXiv:hep-ph/0406184, updated results and plots available at http://ckmfitter.in2p3.fr/
53. CDF, T. Aaltonen, et al., First Flavor-Tagged Determination of Bounds on Mixing-Induced CP Violation in $B_s^0 \to J/\psi\phi$ Decays. Phys. Rev. Lett. 100, 161802 (2008). https://doi.org/10.1103/PhysRevLett.100.161802
54. D0, V.M. Abazov, et al., Measurement of B_s^0 mixing parameters from the flavor-tagged decay $B_s^0 \to J/\psi\phi$. Phys. Rev. Lett. 101, 241801 (2008). https://doi.org/10.1103/PhysRevLett.101.241801
55. LHCb Collaboration, R. Aaij, et al., Opposite-side flavour tagging of B mesons at the LHCb experiment. Eur. Phys. J. **C72**, 2022 (2012). arXiv:1202.4979

56. LHCb collaboration, R. Aaij, et al., New algorithms for identifying the flavour of B^0 mesons using pions and protons. Eur. Phys. J. **C77**, 238 (2017). arXiv:1610.06019
57. LHCb Collaboration, R. Aaij, et al., A precise measurement of the B^0 meson oscillation frequency. Eur. Phys. J. **C76**, 412 (2016). arXiv:1604.03475
58. CDF, A. Abulencia, et al., Measurement of the $B_s^0-\bar{B}_s^0$ Oscillation Frequency. Phys. Rev. Lett. **97**, 062003 (2006). arXiv:hep-ex/0606027
59. LHCb Collaboration, R. Aaij, et al., Precision measurement of the B_s^0–$\bar{\mathrm{B}}_s^0$ oscillation frequency in the decay $B_s^0 \to D_s^- \pi^+$. New J. Phys. **15**, 053021 (2013). arXiv:1304.4741
60. LHCb Collaboration, R. Aaij, et al., Observation of D^0–$\bar{D}^0$ oscillations. Phys. Rev. Lett. **110**, 101802 (2013). arXiv:1211.1230
61. R. Fleischer, Flavor physics and CP violation, in *High-energy physics. Proceedings, European School, Tsakhkadzor, Armenia, August 24–September 6, 2003*, 81–150 (2004). arXiv:hep-ph/0405091
62. LHCb Collaboration, R. Aaij, et al., Measurement of CP violation in $B^0 \to J/\psi K_S^0$ and $B^0 \to \psi(2S)K_S^0$ decays. JHEP **11**, 170 (2017). arXiv:1709.03944
63. Heavy Flavor Averaging Group, Y. Amhis, et al., Averages of b-hadron, c-hadron, and τ-lepton properties as of summer 2016. Eur. Phys. J. **C77**, 895 (2017). arXiv:1612.07233
64. A.E. Snyder, H.R. Quinn, Measuring CP asymmetry in B—rho pi decays without ambiguities. Phys. Rev. D **48**, 2139 (1993)
65. J. Brod, J. Zupan, The ultimate theoretical error on γ from $B \to DK$ decays. JHEP **01**, 051 (2014). arXiv:1308.5663
66. J. Brod, A. Lenz, G. Tetlalmatzi-Xolocotzi, M. Wiebusch, New physics effects in tree-level decays and the precision in the determination of the quark mixing angle γ. Phys. Rev. D **92**, 033002 (2015). arXiv:1412.1446
67. M. Gronau, D. London, How to determine all the angles of the unitarity triangle from B(d)0 – D K(s) and B(s)0–D0. Phys. Lett. B **253**, 483 (1991)
68. M. Gronau, D. Wyler, On determining a weak phase from CP asymmetries in charged B decays. Phys. Lett. B **265**, 172 (1991)
69. D. Atwood, I. Dunietz, A. Soni, Enhanced CP violation with B – K D0 (anti-D0) modes and extraction of the CKM angle gamma. Phys. Rev. Lett. **78**, 3257 (1997). arXiv:hep-ph/9612433
70. A. Giri, Y. Grossman, A. Soffer, J. Zupan, Determining gamma using B+—DK+- with multibody D decays. Phys. Rev. D **68**, 054018 (2003). arXiv:hep-ph/0303187
71. LHCb Collaboration, R. Aaij, et al., Measurement of CP observables in $B^\pm \to DK^\pm$ and $B^\pm \to D\pi^\pm$ with two- and four-body D decays. Phys. Lett. **B760**, 117 (2016). arXiv:1603.08993
72. LHCb Collaboration, R. Aaij, et al., Measurement of the CKM angle γ using $B^\pm \to DK^\pm$ with $DK_S^0\pi^+\pi^-$, $K_S^0K^+K^-$ decays. JHEP **08**, 176 (2018). Erratum ibid. **10** (2018) 107, arXiv:1806.01202
73. R. Aleksan, I. Dunietz, B. Kayser, Determining the CP violating phase gamma. Z. Phys. C **54**, 653 (1992)
74. LHCb Collaboration, R. Aaij, et al., Measurement of CP asymmetry in $B_s^0 \to D^\mp + sK^\pm$ decays. JHEP **11**, 060 (2014). arXiv:1407.6127
75. LHCb Collaboration, Update of the LHCb combination of the CKM angle γ using $B \to DK$ decays, LHCb-CONF-2018-002 (2018)
76. LHCb collaboration, R. Aaij, et al., Determination of the quark coupling strength $|V_{ub}|$ using baryonic decays. Nat. Phys. **11**, 743 (2015). arXiv:1504.01568
77. LHCb collaboration, R. Aaij, et al., Updated measurement of time-dependent CP-violating observables in $B_s^0 \to J/\psi K^+K^-$ decays. Eur. Phys. J. **C79**, 706 (2019). arXiv:1906.08356
78. LHCb Collaboration, R. Aaij, et al., Measurement of the CP-violating phase ϕ_s from $B_s^0 \to J/\psi\pi^+\pi^-$ decays in 13 TeV pp collisions. Phys. Lett. **B797**, 134789 (2019). arXiv:1903.05530
79. LHCb Collaboration, R. Aaij, et al., Observation of CP violation in charm decays. Phys. Rev. Lett. **122**, 211803 (2019). arXiv:1903.08726
80. LHCb Collaboration, R. Aaij, et al., Measurement of matter-antimatter differences in beauty baryon decays. Nat. Phys. **13**, 391 (2017). arXiv:1609.05216
81. LHCb Collaboration, R. Aaij, et al., Search for CP violation in $\Xi_c^+ \to pK^-\pi^+$ decays with model-independent techniques, LHCb-PAPER-2019-026 (in preparation)
82. LHCb Collaboration, R. Aaij, et al., Amplitude analysis of $B^\pm \to \pi^\pm K^+K^-$ decays. Phys. Rev. Lett. **123**, 231802 (2019). arXiv:1905.09244
83. LHCb Collaboration, R. Aaij, et al., Observation of several sources of CP violation in $B^+ \to \pi^+\pi^+\pi^-$ decays. Phys. Rev. Lett. **124**, 031801 (2020). arXiv:1909.05211
84. LHCb Collaboration, R. Aaij, et al., Amplitude analysis of the $B^+ \to \pi^+\pi^+\pi^-$ decay. Phys. Rev. **D101**, 012006 (2020). arXiv:1909.05211
85. M. Beneke, C. Bobeth, R. Szafron, Power-enhanced leading-logarithmic QED corrections to $\mathrm{B}_q \to \mu^+\mu^-$. J. High Energy Phys., **2019** (2019)
86. LHCb, R. Aaij, et al., Measurement of the $B_s^0 \to \mu^+\mu^-$ branching fraction and effective lifetime and search for $B^0 \to \mu^+\mu^-$ decays. Phys. Rev. Lett. **118**, 191801 (2017). arXiv:1703.05747
87. C.M.S. Collaboration, Measurement of properties of $B_\mathrm{s}^0 \to \mu\mu$ decays and search for $B_\mathrm{d}^0 \to \mu\mu$ with the CMS experiment. CMS-PAS-BPH-16-004. Geneva: CERN (2019)
88. M. Aaboud, et al., Study of the rare decays of B_s^0 and B_d^0 mesons into muon pairs using data collected during 2015 and 2016 with the ATLAS detector. J. High Energy Phys. **2019** (2019)
89. LHCb Collaboration, R. Aaij, et al., Angular analysis of the $B^0 \to K^{*0}\mu^+\mu^-$ decay using 3 fb^{-1} of integrated luminosity. JHEP **02**, 104 (2016). arXiv:1512.04442
90. J. Aebischer, et al., *B-decay discrepancies after moriond* (2019)
91. W. Altmannshofer, D.M. Straub,. New physics in $b \to s$ transitions after LHC run 1. Eur. Phys. J. C, **75** (2015)
92. G. Hiller, F. Kruger, More model-independent analysis of $b \to s$ processes. Phys. Rev. D **69**, 074020 (2004). arXiv:hep-ph/0310219

93. C. Bobeth, G. Hiller, G. Piranishvili, Angular distributions of $\bar{B} \to \bar{K}\ell^+\ell^-$ decays. JHEP **12**, 040 (2007). arXiv:0709.4174
94. HPQCD collaboration, C. Bouchard, Standard Model predictions for $B \to K\ell^+\ell^-$ with form factors from lattice QCD, Phys. Rev. Lett. 111, et al. (2013). 162002. *Erratum ibid.*, *112*(2014), 149902. arXiv:1306.0434
95. M. Bordone, G. Isidori, A. Pattori, On the standard Model predictions for R_K and R_{K^*}. Eur. Phys. J. C **76**, 440 (2016). arXiv:1605.07633
96. LHCb Collaboration, R. Aaij, et al., Search for lepton-universality violation in $B^+ \to K^+\ell^+ell^-$ decays. Phys. Rev. Lett. **122**, 191801 (2019). arXiv:1903.09252
97. LHCb Collaboration, R. Aaij, et al., Test of lepton universality with $B^0 \to K^{\star 0}\ell^+\ell^-$ decays. JHEP **08**, 055 (2017). arXiv:1705.05802
98. LHCb Collaboration, R. Aaij, et al., Measurement of $\sigma(pp \to b\bar{b}X$ at $\sqrt{s}$ =7 TeV in the forward region. Phys. Lett. **B694**, 209 (2010). arXiv:1009.2731
99. LHCb Collaboration, R. Aaij, et al., Measurement of J/ψ production in pp collisions at $\sqrt{s}$ =7 TeV. Eur. Phys. J. **C71**, 1645 (2011). arXiv:1103.0423
100. LHCb Collaboration, R. Aaij, et al., Measurement of Υ production in pp collisions at $\sqrt{s}$ =7 TeV. Eur. Phys. J. **C72**, 2025 (2012). arXiv:1202.6579
101. LHCb Collaboration, R. Aaij, et al., Measurement of the $B^\pm$ production cross-section in pp collisions at $\sqrt{s}$ =7 TeV, JHEP **04**, 093 (2012). arXiv:1202.4812
102. LHCb Collaboration, R. Aaij, et al., Measurement of B meson production cross-sections in proton-proton collisions at $\sqrt{s}$ =7 TeV. JHEP **08**, 117 (2013). arXiv:1306.3663
103. LHCb Collaboration, R. Aaij, et al., Production of J/ψ and Υ mesons in pp collisions at $\sqrt{s}$ =8 TeV. JHEP **06**, 064 (2013). arXiv:1304.6977
104. LHCb Collaboration, R. Aaij, et al., Measurement of Υ production in pp collisions at $\sqrt{s}$ = 2.76 TeV. Eur. Phys. J. **C74**, 2835 (2014). arXiv:1402.2539
105. LHCb collaboration, R. Aaij *et al.*, Measurement of the $\eta_c(1S)$ production cross-section in proton-proton collisions via the decay $\eta_c(1S) \to p\bar{p}$, Eur. Phys. J. **C75** (2015) 311, arXiv:1409.3612
106. LHCb Collaboration, R. Aaij, et al., Measurement of forward J/ψ production cross-sections in pp collisions at $\sqrt{s}$ =13 TeV. JHEP **10**, 172 (2015). Erratum ibid. **05** (2017) 063, arXiv:1509.00771
107. LHCb Collaboration, R. Aaij, et al., Measurements of prompt charm production cross-sections in pp collisions at $\sqrt{s}$ =13 TeV. JHEP **03**, 159 (2016). Erratum ibid. **09** (2016) 013, Erratum ibid. **05** (2017) 074, arXiv:1510.01707
108. LHCb Collaboration, R. Aaij, et al., Forward production of Υ mesons in pp collisions at $\sqrt{s}$ =7 and 8 TeV. JHEP **11**, 103 (2015). arXiv:1509.02372
109. LHCb Collaboration, R. Aaij, et al., Measurement of the b-quark production cross-section in 7 and 13 TeV pp collisions. Phys. Rev. Lett. **118**, 052002 (2017). Erratum ibid. **119** (2017) 169901, arXiv:1612.05140
110. LHCb Collaboration, R. Aaij, et al., Measurements of prompt charm production cross-sections in pp collisions at $\sqrt{s}$ =5 TeV. JHEP **06**, 147 (2017). arXiv:1610.02230
111. LHCb Collaboration, R. Aaij, et al., Measurement of the $B^\pm$ production cross-section in pp collisions at $\sqrt{s}$ =7 and 13 TeV. JHEP **12**, 026 (2017). arXiv:1710.04921
112. LHCb Collaboration, R. Aaij, et al., Measurement of Υ production cross-section in pp collisions at $\sqrt{s}$ =13 TeV. JHEP **07**, 134 (2018). arXiv:1804.09214
113. LHCb collaboration, R. Aaij, et al., Measurement of $\psi(2S)$ production cross-sections in proton-proton collisions at $\sqrt{s}$ =7 and 13 TeV. Eur. Phys. J. **C80**, 185 (2020). arXiv:1908.03099
114. LHCb Collaboration, R. Aaij, et al., Measurement of the $\eta_c(1S)$ production cross-section in pp collisions at $\sqrt{s}$ = 13 TeV. Eur. Phys. J. **C80**, 191 (2020). arXiv:1911.03326
115. A. Powell, et al., Particle identification at LHCb, PoS **ICHEP2010** 020, LHCb-PROC-2011-008 (2010)
116. Particle Data Group, M. Tanabashi, et al., Review of particle physics. Phys. Rev. **D98**, 030001 (2018)
117. LHCb Collaboration, R. Aaij, et al., Measurements of the Λ_b^0, Ξ_b^-, and Ω_b^- baryon masses. Phys. Rev. Lett. **110**, 182001 (2013). arXiv:1302.1072
118. LHCb Collaboration, R. Aaij, et al., Precision measurement of D meson mass differences. JHEP **06**, 065 (2013). arXiv:1304.6865
119. LHCb Collaboration, R. Aaij, et al., Observation of excited Λ_b^0 baryons. Phys. Rev. Lett. **109**, 172003 (2012). arXiv:1205.3452
120. LHCb Collaboration, R. Aaij, et al., Observation of two new Ξ_b^- baryon resonances. Phys. Rev. Lett. **114**, 062004 (2015). arXiv:1411.4849
121. LHCb Collaboration, R. Aaij, et al., Measurement of the properties of the Ξ_b^{*0} baryon. JHEP **05**, 161 (2016). arXiv:1604.03896
122. LHCb Collaboration, R. Aaij, et al., χ_{c1} and χ_{c2} resonance parameters with the decays $\chi_{c1,c2} \to J/\psi\mu^+\mu^-$. Phys. Rev. Lett. **119**, 221801 (2017). arXiv:1709.04247
123. LHCb Collaboration, R. Aaij, et al., Observation of a new baryon state in the $\Lambda_b^0\pi^+\pi^-$ mass spectrum. arXiv:2002.05112, submitted to JHEP
124. LHCb Collaboration, R. Aaij, et al., Study of the line shape of the $\chi_{c1}(3872)$ meson. arXiv:2005.13419, Submitted to Phys. Rev. D
125. LHCb Collaboration, R. Aaij, et al., Study of the $\psi_2(3823)$ and $\chi_{c1}(3872)$ states in $B^+ \to (J/\psi\pi^+\pi^-)K^+$ decays. arXiv:2005.13422, submitted to JHEP
126. P. Koppenburg, Beauty 2019—Conference summary, in *18th International Conference on B-Physics at Frontier Machines (Beauty 2019) Ljubljana, Slovenija, September 30–October 4, 2019* (2020). arXiv:2001.11796
127. LHCb Collaboration, R. Aaij, et al., First observation of $B_s^0 \to J/\psi f_0(980)$ decays. Phys. Lett. **B698**, 115 (2011). arXiv:1102.0206
128. LHCb Collaboration, R. Aaij, et al., Observation of $\bar{\mathrm{B}}_s^0 \to J/\psi f_2'(1525)$ in $J/\psi K^+K^-$ final states. Phys. Rev. Lett. **108**, 151801 (2012). arXiv:1112.4695
129. LHCb Collaboration, R. Aaij, et al., Evidence for the decay $B^0 \to J/\psi\omega$ and measurement of the relative branching fractions of B_s^0 meson decays to $J/\psi\eta$ and $J/\psi\eta'$. Nucl. Phys. **B867**, 547 (2013). arXiv:1210.2631
130. LHCb Collaboration, R. Aaij, et al., Amplitude analysis and branching fraction measurement of

$\bar{\mathrm{B}}^0_s \to J/\psi K^+K^-$. Phys. Rev. **D87**, 072004 (2013). arXiv:1302.1213

131. LHCb Collaboration, R. Aaij, et al., Analysis of the resonant components in $\bar{\mathrm{B}}^0 \to J/\psi\pi^+\pi^-$. Phys. Rev. **D87**, 052001 (2013). arXiv:1301.5347
132. LHCb Collaboration, R. Aaij, et al., Observations of $B^0_s \to \psi(2S)\eta$ and $B^0_{(s)} \to \psi(2S)\pi^+\pi^-$ decays. Nucl. Phys. **B871**, 403 (2013). arXiv:1302.6354
133. LHCb Collaboration, R. Aaij, et al., Measurement of the polarization amplitudes in $B^0 \to J/\psi K^\star(892)^0$ decays. Phys. Rev. **D88**, 052002 (2013). arXiv:1307.2782
134. LHCb Collaboration, R. Aaij, et al., Observation of the decay $B^+_c \to J/\psi K^+K^-\pi^+$. JHEP **11**, 094 (2013). arXiv:1309.0587
135. LHCb Collaboration, R. Aaij, et al., Observation of $\bar{\mathrm{B}}^0_s \to J/\psi f_1(1285)$ decays and measurement of the $f_1(1285)$ mixing angle. Phys. Rev. Lett. **112**, 091802 (2014). arXiv:1310.2145
136. LHCb Collaboration, R. Aaij, et al., Measurement of resonant and CP components in $\bar{\mathrm{B}}^0_s \to J/\psi\pi^+\pi^-$ decays. Phys. Rev. **D89**, 092006 (2014). arXiv:1402.6248
137. LHCb Collaboration, R. Aaij, et al., Evidence for the decay $B^+_c \to J/\psi 3\pi^+ 2\pi^-$. JHEP **05**, 148 (2014). arXiv:1404.0287
138. LHCb Collaboration, R. Aaij, et al., Measurement of the resonant and CP components in $\bar{\mathrm{B}}^0 \to J/\psi\pi^+\pi^-$ decays. Phys. Rev. **D90**, 012003 (2014). arXiv:1404.5673
139. LHCb Collaboration, R. Aaij, et al., Observation of the resonant character of the $Z(4430)^-$ state. Phys. Rev. Lett. **112**, 222002 (2014). arXiv:1404.1903
140. LHCb Collaboration, R. Aaij, et al., Observation of the $B^0_s \to J/\psi K^0_S K^\pm\pi^\mp$ decay. JHEP **07**, 140 (2014). arXiv:1405.3219
141. LHCb Collaboration, R. Aaij, et al., A new algorithm for identifying the flavour of B^0_s mesons at LHCb. JINST **11**, P05010 (2016). arXiv:1602.07252
142. LHCb Collaboration, R. Aaij, et al., Model-independent confirmation of the $Z(4430)^-$ state. Phys. Rev. **D92**, 112009 (2015). arXiv:1510.01951
143. LHCb Collaboration, R. Aaij, et al., Model-independent evidence for $J/\psi p$ contributions to $\Lambda^0_b \to J/\psi pK^-$ decays. Phys. Rev. Lett. **117**, 082002 (2016). arXiv:1604.05708
144. LHCb Collaboration, R. Aaij, et al., Observation of exotic $J/\psi\phi$ structures from amplitude analysis of $B^+ \to J/\psi\phi K^+$ decays. Phys. Rev. Lett. **118**, 022003 (2017). arXiv:1606.07895
145. LHCb Collaboration, R. Aaij, et al., Amplitude analysis of $B^+ \to J/\psi\phi K^+$ decays. Phys. Rev. **D95**, 012002 (2017). arXiv:1606.07898
146. LHCb Collaboration, R. Aaij, et al., Observation of $B^+ \to J/\psi 3\pi^+ 2\pi^-$ and $B^+ \to \psi(2S)\pi^+\pi^+\pi^-$ decays. Eur. Phys. J. **C77**, 72 (2017). arXiv:1610.01383
147. LHCb Collaboration, R. Aaij, et al., Study of D_J meson decays to $D^+\pi^-$, $D^0\pi^+$ and $D^{\star+}\pi^-$ final states in pp collisions. JHEP **09**, 145 (2013). arXiv:1307.4556
148. LHCb Collaboration, R. Aaij, et al., Dalitz plot analysis of $B^0 \to \bar{D}^0\pi^+\pi^-$ decays. Phys. Rev. **D92**, 032002 (2015). arXiv:1505.01710
149. LHCb Collaboration, R. Aaij, et al., Amplitude analysis of $B^- \to D^+\pi^-\pi^-$ decays. Phys. Rev. **D94**, 072001 (2016). arXiv:1608.01289
150. LHCb Collaboration, R. Aaij, et al., Determination of quantum numbers for several excited charmed mesons observed in $B^- \to D^{*+}\pi^-\pi^-$ decays. Phys. Rev. **D101**, 032005 (2020). arXiv:1911.03326
151. LHCb Collaboration, R. Aaij, et al., Study of D_{sJ} decays to $D^+K^0_S$ and D^0K^+ final states in pp collisions. JHEP **10**, 151 (2012). arXiv:1207.6016
152. LHCb Collaboration, R. Aaij, et al., Observation of overlapping spin-1 and spin-3 $\bar{D}^0K^-$ resonances at mass 2.86 GeV/c^2. Phys. Rev. Lett. **113**, 162001 (2014). arXiv:1407.7574
153. BaBar Collaboration, B. Aubert, et al., Observation of a new D_{squark} meson decaying to DK at a mass of 2.86 GeV/c^2. Phys. Rev. Lett. **97**, 222001 (2006). arXiv:hep-ex/0607082
154. BaBar Collaboration, B. Aubert, et al., Study of D_{sJ} decays to D^*K in inclusive e^+e^- interactions. Phys. Rev. **D80**, 092003 (2009). arXiv:0908.0806
155. LHCb Collaboration, R. Aaij, et al., Study of the D^0p amplitude in $\Lambda^0_b \to D^0p\pi^-$ decays, JHEP **05**, 030 (2017). arXiv:1701.07873
156. LHCb Collaboration, R. Aaij, et al., Observation of new Ξ^0_c baryons decaying to $\Lambda^+_c K^-$. Phys. Rev. Lett. **124**, 222001 (2020). arXiv:2003.13649
157. LHCb Collaboration, R. Aaij, et al., Observation of five new narrow Ω^0_c states decaying to $\Xi^+_c K^-$. Phys. Rev. Lett. **118**, 182001 (2017). arXiv:1703.04639
158. V.R. Debastiani, J.M. Dias, W.H. Liang, E. Oset, Molecular Ω^0_c states generated from coupled meson-baryon channels. Phys. Rev. D **97**, 094035 (2018). arXiv:1710.04231
159. S.S. Gershtein, V.V. Kiselev, A.K. Likhoded, A.I. Onishchenko, Spectroscopy of doubly heavy baryons. Phys. Atom. Nucl. **63**, 274 (2000). arXiv:hep-ph/9811212, [Yad. Fiz. 63, 334 (2000)]
160. SELEX Collaboration, M. Mattson, et al., First observation of the doubly charmed baryon $\Xi_c c^+$. Phys. Rev. Lett. **89**, 112001 (2002). arXiv:hep-ex/0208014
161. SELEX Collaboration, A. Ocherashvili, et al., Confirmation of the double charm baryon $\Xi_c c^+(3520)$ via its decay to pD^+K^-. Phys. Lett. **B628**, 18 (2005). arXiv:hep-ex/0406033
162. S.P. Ratti, New results on c-baryons and a search for cc-baryons in FOCUS. Nucl. Phys. (Proc. Suppl.) **115**, 33 (2003)
163. BaBar Collaboration, B. Aubert, et al., Search for doubly charmed baryons $\Xi_c c^+$ and $\Xi_c c^+ +$ in BABAR. Phys. Rev. **D74**, 011103 (2006). arXiv:hep-ex/0605075
164. Belle Collaboration, R. Chistov, et al., Observation of new states decaying into $\Lambda^+_c K^-\pi^+$ and $\Lambda^+_c K^0_S\pi^-$. Phys. Rev. Lett. **97**, 162001 (2006). arXiv:hep-ex/0606051
165. LHCb Collaboration, R. Aaij, et al., Search for the doubly charmed baryon Ξ^+_{cc}. JHEP **12**, 090 (2013). arXiv:1310.2538
166. LHCb Collaboration, R. Aaij, et al., First observation of the doubly charmed baryon decay $\Xi^{++}_{cc} \to \Xi^+_c\pi^+$. Phys. Rev. Lett. **121**, 162002 (2018). arXiv:1807.01919

167. LHCb Collaboration, R. Aaij, et al., Measurement of the lifetime of the doubly charmed baryon $\Xi_c c^+ +$. Phys. Rev. Lett. **121**, 052002 (2018). arXiv:1806.02744
168. LHCb Collaboration, R. Aaij, et al., Precision measurement of the $\Xi_c c^+ +$ mass. JHEP **02**, 049 (2020). arXiv:1911.08594
169. LHCb Collaboration, R. Aaij, et al., Observation of the doubly charmed baryon $\Xi_c c^+ +$. Phys. Rev. Lett. **119**, 112001 (2017). arXiv:1707.01621
170. CDF Collaboration, T. Aaltonen, et al., Measurement of resonance parameters of orbitally excited narrow B^0 mesons. Phys. Rev. Lett. **102**, 102003 (2009). arXiv:0809.5007
171. D0 Collaboration, V.M. Abazov, et al., Observation and properties of $L = 1B_1$ and B_2^* mesons. Phys. Rev. Lett. **99**, 172001 (2007). arXiv:0705.3229
172. CDF Collaboration, T.A. Aaltonen, et al., Study of orbitally excited B mesons and evidence for a new $B\pi$ resonance. Phys. Rev. **D90**, 012013 (2014). arXiv:1309.5961
173. LHCb Collaboration, R. Aaij, et al., Precise measurements of the properties of the $B_1(5721)^{0,+}$ and $B_2^*(5747)^{0,+}$ states and observation of structure at higher invariant mass in the $B^+\pi^-$ and $B^0\pi^+$ spectra. JHEP **04**, 024 (2015). arXiv:1502.02638
174. CDF Collaboration, T. Aaltonen, *et al.*, Observation of orbitally excited B_s mesons, Phys. Rev. Lett. **100**, 082001 (2008). arXiv:0710.4199
175. D0 Collaboration, V.M. Abazov, et al., Observation and properties of the orbitally excited B*(s2) meson, Phys. Rev. Lett. **100**, 082002 (2008). arXiv:0711.0319
176. M. Di Pierro, E. Eichten, Excited heavy–light systems and hadronic transitions. Phys. Rev. D **64**, 114004 (2001). arXiv:hep-ph/0104208
177. ATLAS, G. Aad, et al., Observation of an Excited $B_c^\pm$ Meson State with the ATLAS detector. Phys. Rev. Lett. **113**, 212004 (2014). arXiv:1407.1032
178. LHCb Collaboration, R. Aaij, et al., Search for excited B_c^+ states. JHEP **01**, 138 (2018). arXiv:1712.04094
179. CMS, A.M. Sirunyan, et al., Observation of Two Excited B_c^+ states and measurement of the $\mathrm{B}_c^+(2S)$ mass in pp collisions at $\sqrt{s} = 13$ TeV. Phys. Rev. Lett. **122**, 132001 (2019). arXiv:1902.00571
180. LHCb Collaboration, R. Aaij, et al., Observation of an excited B_c^+ state. Phys. Rev. Lett. **122**, 232001 (2019). arXiv:1904.00081
181. LHCb Collaboration, R. Aaij, et al., Observation of new resonances in the $\Lambda_b^0\pi^+\pi^-$ system. Phys. Rev. Lett. **123**, 152001 (2019). arXiv:1907.13598
182. S. Capstick, N. Isgur, Baryons in a relativized quark model with chromodynamics. Phys. Rev. D **34**, 2809 (1986)
183. CMS, A.M. Sirunyan, et al., Study of excited Λ_b^0 states decaying to $\Lambda_\mathrm{b}^0\pi^+\pi^-$ in proton-proton collisions at $\sqrt{s} = 13$ TeV. arXiv:2001.06533
184. LHCb Collaboration, R. Aaij, et al., Observation of two resonances in the $\Lambda_b^0\pi^\pm$ systems and precise measurement of $\Sigma_b^\pm$ and $\Sigma_b^{*\pm}$ properties. Phys. Rev. Lett. **122**, 012001 (2019). arXiv:1809.07752
185. C.D.F. Collaboration, T. Aaltonen et al., Observation of the heavy baryons Σ_b and Σ_b^*. Phys. Rev. Lett. **99**, 202001 (2007)
186. CDF, T. Aaltonen, et al., Measurement of the masses and widths of the bottom baryons Σ_b^{+-} and Σ_b^{*+-}. Phys. Rev. **D85**, 092011 (2012). arXiv:1112.2808
187. CMS Collaboration, S. Chatrchyan, et al., Observation of a new Ξ_b baryon. Phys. Rev. Lett. **108**, 252002 (2012). arXiv:1204.5955
188. W. Detmold, C.J.D. Lin, S. Meinel, Calculation of the heavy-hadron axial couplings g_1, g_2 and g_3 using lattice QCD. Phys. Rev. D **85**, 114508 (2012). arXiv:1203.3378
189. C. Chen et al., Strong decays of charmed baryons. Phys. Rev. D **75**, 094017 (2007). arXiv:0704.0075
190. LHCb Collaboration, R. Aaij, et al., Observation of a new Ξ_b^- resonance. Phys. Rev. Lett. **121**, 072002 (2018). arXiv:1805.09418
191. LHCb Collaboration, R. Aaij, et al., First observation of excited Ω_b^- states. Phys. Rev. Lett. **124**, 082002 (2020). arXiv:2001.00851
192. K.-L. Wang, Y.-X. Yao, X.-H. Zhong, Q. Zhao, Strong and radiative decays of the low-lying S- and P-wave singly heavy baryons. Phys. Rev. D **96**, 116016 (2017). arXiv:1709.04268
193. LHCb Collaboration, R. Aaij, et al., Near-threshold $D\bar{D}$ spectroscopy and observation of a new charmonium state. JHEP **07**, 035 (2019). arXiv:1903.12240
194. T. Barnes, S. Godfrey, E.S. Swanson, Higher charmonia. Phys. Rev. D **72**, 054026 (2005)
195. LHCb Collaboration, R. Aaij, et al., Observation of $J/\psi p$ resonances consistent with pentaquark states in $\Lambda_b^0 \to J/\psi p K^-$ decays. Phys. Rev. Lett. **115**, 072001 (2015). arXiv:1507.03414
196. LHCb Collaboration, R. Aaij, et al., Evidence for exotic hadron contributions to $\Lambda_b^0 \to J/\psi p\pi^-$ decays. Phys. Rev. Lett. **117**, 082003 (2016). arXiv:1606.06999
197. LHCb Collaboration, R. Aaij, et al., Observation of a narrow $P_c(4312)^+$ state, and of two-peak structure of the $P_c(4450)^+$. Phys. Rev. Lett. **122**, 222001 (2019). arXiv:1904.03947
198. Belle Collaboration, S.-K. Choi, et al., Observation of a narrow charmonium-like state in exclusive $B^\pm \to K^\pm\pi^+\pi^- J/\psi$ decays. Phys. Rev. Lett. **91**, 262001 (2003). arXiv:hep-ex/0309032
199. CDF Collaboration, D. Acosta, et al., Observation of the narrow state $X(3872) \to J/\psi\pi^+\pi^-$ in $p\bar{p}$ collisions at $\sqrt{s} = 1.96$ TeV. Phys. Rev. Lett. **93**, 072001 (2004). arXiv:hep-ex/0312021
200. D0 Collaboration, V.M. Abazov, et al., Observation and properties of the X(3872) decaying to $J/\psi\pi^+\pi^-$ in $p\bar{p}$ collisions at $\sqrt{s} = 1.96$ TeV. Phys. Rev. Lett. **93**, 162002 (2004). arXiv:hep-ex/0405004
201. BaBar Collaboration, B. Aubert, et al., Study of the $B^- \to J/\psi K^-\pi^+\pi^-$ decay and measurement of the $B^- \to X(3872)K^-$ branching fraction. Phys. Rev. **D71**, 071103 (2005). arXiv:hep-ex/0406022
202. N.A. Tornqvist, Isospin breaking of the narrow charmonium state of Belle at 3872-MeV as a deuson. Phys. Lett. B **590**, 209 (2004). arXiv:hep-ph/0402237
203. L. Maiani, F. Piccinini, A.D. Polosa, V. Riquer, Diquark-antidiquarks with hidden or open charm and the nature of $X(3872)$. Phys. Rev. D **71**, 014028 (2005). arXiv:hep-ph/0412098
204. C. Hanhart, Y.S. Kalashnikova, A.V. Nefediev, Interplay of quark and meson degrees of freedom in a near-

threshold resonance: multi-channel case. Eur. Phys. J. A **47**, 101 (2011). arXiv:1106.1185

205. BaBar Collaboration, B. Aubert, et al., Search for $B^+ \to X(3872)K^+$, $X(3872) \to J/\psi\gamma$. Phys. Rev. **D74**, 071101 (2006). arXiv:hep-ex/0607050
206. Belle Collaboration, V. Bhardwaj, et al., Observation of $X(3872) \to J/\psi\gamma$ and search for $X(3872) \to \psi'\gamma$ in B decays. Phys. Rev. Lett. **107**, 091803 (2011). arXiv:1105.0177
207. CDF Collaboration, A. Abulencia, et al., Analysis of the quantum numbers J^{PC} of the $X(3872)$. Phys. Rev. Lett. **98**, 132002 (2007). arXiv:hep-ex/0612053
208. M. Jacob, G.C. Wick, On the general theory of collisions for particles with spin. Ann. Phys. **7**, 404 (1959)
209. J.D. Richman, An experimenter's guide to the helicity formalism, CALT-68-1148 (1984)
210. S.U. Chung, General formulation of covariant helicity-coupling amplitudes. Phys. Rev. D **57**, 431 (1998)
211. LHCb Collaboration, R. Aaij, et al., Determination of the $X(3872)$ meson quantum numbers. Phys. Rev. Lett. **110**, 222001 (2013). arXiv:1302.6269
212. LHCb Collaboration, R. Aaij, et al., Quantum numbers of the $X(3872)$ state and orbital angular momentum in its $\rho^0 J/\psi$ decays. Phys. Rev. **D92**, 011102(R) (2015). arXiv:1504.06339
213. BaBar Collaboration, B. Aubert, et al., A Study of $B \to X(3872)K$, with $X_{3872} \to J/\Psi\pi^+\pi^-$. Phys. Rev. **D77**, 111101 (2008). arXiv:0803.2838
214. CDF Collaboration, T. Aaltonen, et al., Precision measurement of the $X(3872)$ Mass in $J/\psi\pi^+\pi^-$ decays. Phys. Rev. Lett. **103**, 152001 (2009). arXiv:0906.5218
215. LHCb Collaboration, R. Aaij, et al., Observation of $X(3872)$ production in pp collisions at $\sqrt{s}$ =7 TeV. Eur. Phys. J. **C72**, 1972 (2012). arXiv:1112.5310
216. Belle Collaboration, S.-K. Choi, et al., Bounds on the width, mass difference and other properties of $X(3872) \to \pi^+\pi^- J/\psi$ decays. Phys. Rev. **D84**, 052004 (2011). arXiv:1107.0163
217. BESIII Collaboration, M. Ablikim, et al., Observation of $epem \to X(3872)\gamma$ at BESIII. Phys. Rev. Lett. **112**, 092001 (2014). arXiv:1310.4101
218. ATLAS Collaboration, M. Aaboud, et al., Measurements of $\psi(2S)$ and $X(3872) \to J/\psi\pi^+\pi^-$ production in pp collisions at $\sqrt{s} = 8$ TeV with the ATLAS detector. JHEP **01**, 117 (2017). arXiv:1610.09303
219. CMS Collaboration, S. Chatrchyan, et al., Measurement of the $X(3872)$ production cross section via decays to $J/\psi\pi^+\pi^-$ in pp collisions at $\sqrt{s} = 7$ TeV. JHEP **04**, 154 (2013). arXiv:1302.3968
220. BaBar Collaboration, B. Aubert, et al., Evidence for $X(3872) \to \psi_{2S}\gamma$ in $B^\pm \to X_{3872}K^\pm$ decays, and a study of $B \to c\bar{c}\gamma K$. Phys. Rev. Lett. **102**, 132001 (2009). arXiv:0809.0042
221. CDF Collaboration, T. Aaltonen, et al., Evidence for a narrow near-threshold structure in the $J/\psi\phi$ mass spectrum in $B^+ \to J/\psi\phi K^+$ decays. Phys. Rev. Lett. **102**, 242002 (2009). arXiv:0903.2229
222. CMS, S. Chatrchyan, et al., Observation of a peaking structure in the $J/\psi\phi$ mass spectrum from $B^\pm \to J/\psi\phi K^\pm$ decays. Phys. Lett. **B734**, 261 (2014). arXiv:1309.6920
223. D0, V.M. Abazov, et al., Search for the $X(4140)$ state in $B^+ \to J_{\psi,\phi}K^+$ decays with the D0 Detector. Phys. Rev. **D89**, 012004 (2014). arXiv:1309.6580
224. D0, V.M. Abazov, et al., Inclusive Production of the X(4140) State in $p\bar{p}$ Collisions at D0. Phys. Rev. Lett. **115**, 232001 (2015). arXiv:1508.07846
225. J. Brodzicka, Heavy flavour spectroscopy. Conf. Proc. **C0908171**, 299 (2009)
226. S. Belle, Cheng-Ping, XYZ particles at Belle. Chin. Phys. C **34**, 615 (2010). arXiv:0912.2386
227. BaBar, J.P. Lees, et al., Study of $B^{\pm,0} \to J/\psi K^+K^-K^{\pm,0}$ and search for $B^0 \to J/\psi\phi$ at BABAR. Phys. Rev. **D91**, 012003 (2015). arXiv:1407.7244
228. LHCb Collaboration, R. Aaij, et al., Search for the $X(4140)$ state in $B^+ \to J/\psi\phi K^+$ decays. Phys. Rev. **D85**, 091103(R) (2012). arXiv:1202.5087
229. Belle, S.K. Choi, et al., Observation of a resonance-like structure in the $pi^\pm\psi'$ mass distribution in exclusive $B \to K\pi^\pm\psi'$ decays. Phys. Rev. Lett. **100**, 142001 (2008). arXiv:0708.1790
230. Belle, K. Chilikin, et al., Experimental constraints on the spin and parity of the $Z(4430)^+$. Phys. Rev. **D88**, 074026 (2013). arXiv:1306.4894
231. M.B. Voloshin, $Z_c(3900)$ - what is inside? Phys. Rev. D **87**, 091501 (2013). arXiv:1304.0380
232. LHCb Collaboration, R. Aaij, et al., Evidence for a $\eta_c(1S)\pi^-$ resonance in $B^0 \to \eta_c(1S)K^+\pi^-$ decays. Eur. Phys. J. **C78**, 1019 (2018). arXiv:1809.07416
233. LHCb Collaboration, R. Aaij, et al., Observation of J/ψ-pair production in pp collisions at $\sqrt{s}$ =7 TeV. Phys. Lett. **B707**, 52 (2012). arXiv:1109.0963
234. LHCb Collaboration, R. Aaij, et al., Measurement of the J/ψ pair production cross-section in pp collisions at $\sqrt{s}$ =13 TeV. JHEP **06**, 047 (2017). Erratum ibid. **10** (2017) 068, arXiv:1612.07451
235. LHCb Collaboration, R. Aaij, et al., Observation of structure in the J/ψ pair mass spectrum. LHCb-PAPER-2020-011 (in preparation)
236. LHCb Collaboration, R. Aaij, et al., Study of η–η' mixing from measurement of $B^0_(s)J/\psi\eta^{(\prime)}$ decay rates. JHEP **01**, 024 (2015). arXiv:1411.0943
237. LHCb Collaboration, R. Aaij, et al., Measurement of the forward W and Z boson production in pp collisions at $\sqrt(s)$=8 TeV . JHEP **01**, 155 (2016). arXiv:1511.08039
238. LHCb Collaboration, R. Aaij, et al., Measurement of forward W and Z boson production in association with jets in p-p collisions at $\sqrt(s)$=8 TeV. JHEP **05**, 131 (2016). arXiv:1605.0095
239. LHCb Collaboration, R. Aaij, et al., Measurement of forward $Z \to e^+e^-$ production at $\sqrt{s} = 8$ TeV. JHEP **05**, 109 (2015). arXiv:1503.00963
240. LHCb Collaboration, R. Aaij, et al., A study of the Z production cross-section in pp collisions at $\sqrt{s} =$ 7 TeV using tau final states. JHEP **01**, 111 (2013). arXiv:1210.6289
241. LHCb Collaboration, R. Aaij, et al., Measurement of forward $W \to e\nu$ production in pp collisions at $\sqrt{s} = 8$ TeV. JHEP **10**, 030 (2016). arXiv:1608.01484
242. LHCb Collaboration, R. Aaij, et al., Measurement of the forward Z boson production cross-section in pp

collisions at $\sqrt(s)$ = 13 TeV. JHEP **09**, 136 (2016). arXiv:1607.06495

243. LHCb Collaboration, R. Aaij, et al., Identification of beauty and charm quark jets at LHCb. JINST **10**, P06013 (2015). arXiv:1505.04051
244. M. Cacciari et al., The anti-kT jet clustering algorithm. JHEP **0804**, 063 (2008). arXiv:0802.1189
245. LHCb Collaboration, R. Aaij, et al., Measurement of forward $t\bar{t}$, $W+b\bar{b}$ and $W+c\bar{c}$ production in pp collisions at $sqrt(s) = 8$ TeV. Phys. Lett. **B767**, 110 (2017). arXiv:1610.08142
246. LHCb Collaboration, R. Aaij, et al., First observation of forward $Z \rightarrow b\bar{b}$ production in pp collisions at $\sqrt{s}$ =8 TeV. Phys. Lett. **B776**, 430 (2018). arXiv:1709.03458
247. R. Alexander, et al., Dark Sectors 2016 Workshop , Community Report (2016). arXiv:1608.08632
248. LHCb Collaboration, R. Aaij, et al., Search for dark photons produced in 13 TeV pp collisions. Phys. Rev. Lett. **120**, 061801 (2018). arXiv:1710.02867
249. LHCb Collaboration, R. Aaij, et al., Precision Luminosity measurement at LHCb. JINST **9**, P12005 (2014). arXiv:1410.0149
250. LHCb Collaboration, R. Aaij, et al., First measurements of charm production in fixed-target configuration at the LHC. Phys. Rev. Lett. **122**, 132002 (2019). arXiv:1810.07907
251. LHCb Collaboration, R. Aaij, et al., Measurement of antiproton production in p He collisions at $\sqrt{s_{nn}}$ = 110 GeV. Phys. Rev. Lett. **121**, 222001 (2018). arXiv:1808.06127
252. AMS Collaboration, M. Aguilar, et al., Antiproton flux, antiproton-to-proton flux ratio,and properties of elementary particle fluxes in primary cosmic rays measured with the Alpha Magnetic Spectrometer on the International Space Station. Phys. Rev. Lett. **117**, 091103 (2016)
253. LHCb Collaboration, R. Aaij, et al., Study of Υ production in pPb collisions at $\sqrt{s_{NN}}$ = 8.16 TeV. arXiv:1810.07655 arXiv:1810.07655
254. R. Fleischer, T. Hurth, M.L. Mangano (eds.), *Flavor in the era of the LHC: reports of the CERN working groups*, vol. 29 of *Advances in the Physics of Particles and Nuiclei*, Springer-Verlag Berlin Heidelberg, 2009. Reprinted from Eur. Phys. J. C57 (2008) 1
255. LHCb Collaboration, CERN-LHCC-2011-001 (2011) Letter of Intent (LoI) for the LHCb upgrade
256. LHCb Collaboration, Framework TDR for the LHCb Upgrade: Technical Design Report, CERN-LHCC-2012-007 (2012)
257. LHCb Collaboration, LHCb Tracker Upgrade Technical Design Report, CERN-LHCC-2014-001 (2014)
258. LHCb Collaboration, LHCb VELO Upgrade Technical Design Report, CERN-LHCC-2013-021 (2013)
259. LHCb Collaboration, LHCb PID Upgrade Technical Design Report, CERN-LHCC-2013-022 (2013)
260. LHCb Collaboration, Computing Model of the Upgrade LHCb experiment, CERN-LHCC-2018-014 (2018)
261. BELLE II Collaboration, T. Abe, et al., Belle II Technical Design Report, Rep. No. KEK-REPORT-2010-1 (2010). arXiv:1011.0352
262. LHCb Collaboration, LHCb Trigger and Online Technical Design Report, CERN-LHCC-2014-016 (2014)
263. LHCb Collaboration, Expression of Interest for a Phase-II LHCb Upgrade: Opportunities in flavour physics, and beyond, in the HL-LHC era, CERN-LHCC-2017-003 (2017)
264. LHCb Collaboration, Physics case for an LHCb Upgrade II—Opportunities in flavour physics, and beyond, in the HL-LHC era. arXiv:1808.08865